Direct Measurement of Magnetic Monopole Charge and Transport Dynamics

Chun-Chih Hsu

Jesus College

University of Oxford

A thesis submitted to for the degree of

Doctor of Philosophy

Trinity 2024

ABSTRACT

Magnetic monopoles are magnetic excitations with quantized magnetic charge whose existence in pyrochlore spin ice materials has been studied widely. As a platform to study the hypothetical magnetic monopoles, classical spin ices have aroused fundamental interest. Despite the extensive studies, the transport theory of the magnetic monopole fluid remains elusive, especially indicated by the recent investigation with noise spectroscopy. This thesis endeavors to elucidate the dynamics of the monopole fluid by developing advanced SQUID-based spectrometer and provides several unique pieces of evidence towards the dynamical mechanism.

In Chapter 1 of the thesis. I first briefly introduce spin ice materials and the emergence of the magnetic monopoles from a historical basis. Chapter 2 points out recent puzzles in magnetic monopole dynamics uncovered by the noise spectroscopy. Both the free monopole fluid theory and the advanced dynamical fractal theory on monopole motion are described in detail. In Chapter 3, I present a thorough description of the home-built SQUID-based monopole current/noise spectrometer that I have been working on throughout my DPhil. The high precision spectrometer compatible with external magnetic field is designed to perform experiments mentioned in Chapter 2. In addition, the calibration process and introduction on types of measurement of SQUID spectroscopy are included. Starting from Chapter 4, I present the work using this newly-developed technique. In Chapter 4, I discuss the exploration of dichotomous monopole dynamics originated from another slower spin flipping rate in $Dy_2Ti_2O_7$. By combining Monte Carlo simulation and monopole current measurements, signatures from dynamical fractal motion are identified. Chapter 5 further investigates the monopole noise towards lower temperatures, leading to the discovery of dynamical heterogeneity of the magnetic monopole fluid in its supercooled state. Monopole noise characterizes the gradual transition from the free monopole fluid to the supercooled fluid, and eventually towards the glass-forming state. In Chapter 6, I provide a direct measurement on the magnetic charge, which is the core of the monopole dynamics. The excellent agreement of the charge between theory and experiments marks the importance of entropic force in the monopole transport. Finally, the overall work and the potential future exploration is summarized in Chapter 7.

To my dearest father and mother, and those who have supported me on this challenging but memorable journey.

ACKNOWLEDGEMENTS

First and foremost, I would like to express my gratitude to my DPhil supervisor, Prof. J.C. Séamus Davis, for the unwavering guidance and encouragement throughout this journey. It is my honor to work with such great physicists. His expertise, insightful feedback, and the enthusiasm towards exploring unknown nature have always been stimulating and supportive. I am truly grateful for the opportunities and the inspiration he provided me to grow as a better researcher.

I am fortunate that I have such wonderful labmates in the Davis group, making my time in the group joyful and unforgettable. Among these colleagues, I especially thank Hiroto Takahashi. As a research partner, he is always very helpful on all kinds of work and countless discussion. Without him, building the cryostat and completing the research projects would not be possible. As a part of the spin noise team, I would like to extend to my thanks to Fabian Jerzembeck, Jahn Dasini, Chaia Carroll, Jack Murphy, Jonathan Ward, and Catherine Dawson. Despite being physically far away from Oxford, they are always kind to support me on technical issues and most importantly, to make our lab a cheerful place. I would also like to thank Ritika Dusad, who really is the pioneer of the work of this thesis, for frequently traveling to Oxford just to provide experimental assistance. I was constantly amazed by her tricks on instrumentation and her quick thoughts on alternative solutions to my blindspot. In Oxford, I am grateful to have colleagues with brilliant minds. Being the closest neighbor to my experimental room, Prof. Shuqiu Wang and Wangping Ren often assisted my daily lab work. I appreciate the time we spent together, including those memorable formal dinners, and the joy they have shared with me. I thank Yutong Dai in particular for being one of my closest friends in Oxford and helping me on various lab tasks. Harris Pirie, Niall Kennedy, Jan Knapp, and Jack Enright are all among the smartest people I have met. Not only did they provide great sources of help, I also enjoyed the time when they shared creative ideas. Weijiong Chen taught me numerous experimental skills, broadening my view as an experimentalist. Many thanks also to my colleagues in Cork and Cornell, including Jiahao Yan, Ge He, Huiyu Zhao, Siyuan Wan, Vincent Oliviero, Joe Carroll, Qiangqiang Gu, and Kuanysh Zhussupbekov. Although we don’t have many opportunities to meet, their friendliness

and generosity are very heartfelt when we met in conferences or in my visits to UCC. It was truly my pleasure to work with these amazing colleagues in the group.

Within a highly collaborative project, I would like to express my appreciation towards Jonathan Hallén, Prof. Claudio Castelnovo, and Prof. Roderich Moessner, for significant contribution that enriched the research in this thesis. The intense discussion and their insightful perspectives were really crucial in this work. I thank Prof. Steve Blundell and Prof. Graeme Luke for various exciting collaborations. To construct a home-made cryostat from the scratch, I have received lots of assistance from staff of the department. I would like to express my sincere gratitude to building service, stores, and mechanical workshop staff members, especially to Pierre Van Zijl, David Sharp, Robert Storey, Bradley Harsant, Philip Prior, Johan Pretorius, Jonathan Denton, and Alan Francis, for the effort on making the ANDROMEDA into reality.

At last, I thank my dearest parents for supporting me on the journey of exploring the beauty of physics. It is the encouragement from them that gives me strength and perseverance to overcome the obstacles in pursuit of the DPhil degree. I also thank all the friends, in and out of Oxford, who have brought me cheer and delight. Po-Yuan Huang, Han Lee, Allen Lee, and Ming Liu are all friendly people and I will not forget those fun moments we shared. I would also like to thank Neng-Chun Chiu, Shu-Fan Chen, Joy Hsu, Chia-Kai Guo and Yen Yun. Although these old friends may not work on the same physics area or time zone, I enjoy every moment we chat about the exploration of physics and the experience of pursuing a physics PhD degree. All in all, I am truly lucky to meet these friends and cannot express my appreciation enough to all these wonderful people.

TABLE OF CONTENTS

LIST OF FIGURES

The major works presented in this thesis (Chapter 4 to Chapter 6) are collaborative works, and here I would like to acknowledge the contribution. At the moment when this thesis is written, part of the Chapter 4 has been published in *Proc. Natl. Acad. Sci. U.S.A.* **121**, e2320384121 (2024). I have built the monopole current/noise spectrometer with the assistance from Hiroto Takahashi and Ritika Dusad. I performed all the experiments with the assistance from Hiroto Takahashi, Jahn Dasini, and Chaia Carroll. I also performed the data analysis for the work. Sudarshan Sharma and Graeme Luke provided the sample. Jonathan Hallén performed the Monte-Carlo simulations. Part of the Chapter 5 appears in arXiv:2408.00460 (2024). In the work of Chapter 5, I developed the technique and the programming protocol for the susceptibility measurements. I assisted Jahn Dasini and Chaia Carroll with performing the magnetic susceptibility and noise experiments. Jahn Dasini and Chaia Carroll performed the data analysis. For the work of the Chapter 6, I have constructed a modified spectrometer with the assistance from Hiroto Takahashi. I performed all the experiments and data analysis.

Chapter 1 Introduction

Learn from yesterday, live for today, hope for tomorrow. The important thing is not to stop questioning.

--Albert Einstein

Spin ice materials are remarkably simple systems, yet they show unexpectedly complex collective magnetic behavior at low temperature (*1-4*). In the first approximation, spin ice is merely a classical Ising antiferromagnet. However, with the combination of the highly frustrated geometry, the ground state becomes highly degenerate, and its spin configuration is analogous to the bonding configuration of water ice. One major consequence is the residual entropy at low temperature due to the spin degeneracy. It was later realized by the community that the dominating interaction in the classical spin ice is, in fact, the dipolar interaction of spins. To explain the mystery of the screened dipolar interaction, the beautiful idea of the magnetic monopole as the excitation is born. One spin flip against the ice rule can be seen as the creation of a pair of magnetic monopoles, thus opening the door to the physics of spin fractionalization. Rewriting the dipolar spin ice model in terms of the magnetic monopole Coulomb interaction harmonizes the complex description and explains various experimental discoveries. In this chapter, I will introduce the background for the primary work of this thesis, starting from the pyrochlore material and the classical spin ice.

1.1 Rare Earth Oxide Pyrochlore and Spin Ice

Spin ice physics arises from rare-earth oxides with the pyrochlore lattice. The pyrochlore lattice is characterized by a three-dimensional network of corner sharing tetrahedra, which forms a face centered cubic (FCC) Bravais lattice (Figure 1.1). The

canonical spin ice compounds belong to a broader family of $A_2B_2O_7$ materials, such as $Dy_2Ti_2O_7$ (DTO) and $Ho_2Ti_2O_7$ (HTO). In $A_2B_2O_7$ materials, both A and B sit on interpenetrating pyrochlore sublattices. In DTO, Ti and O ions are non-magnetic, while Dy^{3+} is the magnetic ion with large spin J_s = 15/2, which leads to the huge magnetic moment of $\mu \approx 10\mu_B$.

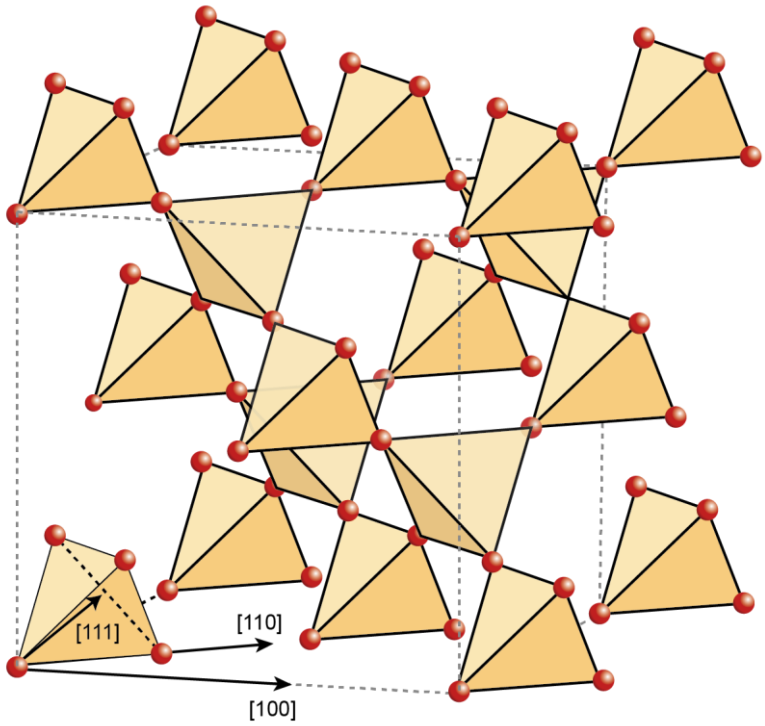

Figure 1.1 The representation of the pyrochlore lattice. For the canonical spin ice material DTO. Dy^{3+} ions sit at the position corresponding to the red spheres, forming the corner-sharing tetrahedron. The [111] direction points in the center of the tetrahedron.

As the first approximation, the spin ice can be understood as the ferromagnetic Ising model. With the J_{ex} denoted as the exchange coupling, the Hamiltonian is

$$\mathcal{H} = -J_{\text{ex}} \sum_{\langle i,j \rangle} \vec{\mu}_i \cdot \vec{\mu}_j \tag{1.1}$$

The angular moment $\vec{\mu}_i$ can be written as $\vec{\mu}_i = \mu S_i \hat{z}_i$, where $S_i = 1$ or -1 for the spins

that are parallel or antiparallel to the <111> direction (pointing in or out of the center of the tetrahedron). Due to the strong spin anisotropy along the <111> direction the in pyrochlore lattice, we have $\hat{z}_i \cdot \hat{z}_j = -\frac{1}{3}$ for the nearest neighbors. Thus, the Hamiltonian becomes

$$\mathcal{H} = \frac{\mu^2 J_{\text{ex}}}{3} \sum_{\langle i,j \rangle} S_i S_j \tag{1.2}$$

Clearly, the ground state has the maximum number of antiparallel spin pairs for each tetrahedron. That is, two of the spins point in to the center, while the other two spins point out of the center (2-in-2-out), as shown in Figure 1.2. This constraint is the so-called ‘‘ice rule’’ and this is how the material gets its name of spin ice. For a pure cubic lattice, such a constraint will only lead to two types of antiferromagnetic spin configuration with antiparallel spins. However, for the corner sharing pyrochlore lattice, the ice rule constraint results in a highly degenerate ground state (*5*). Thus, long-range magnetic order fails to form in spin ice materials. For example, neutron scattering measurements of HTO observed the absence of any magnetic Bragg peak even below the Curie-Weiss temperature T_{CW} at ~ 2 K (*6*). Likewise, DC susceptibility measurement has determined the T_{CW} for DTO at approximately 1.2 K (*7*). However, neutron scattering spectra show diffusive scattering down to 0.05 K, indicating non-magnetic ordering well below T_{CW} (*8*).

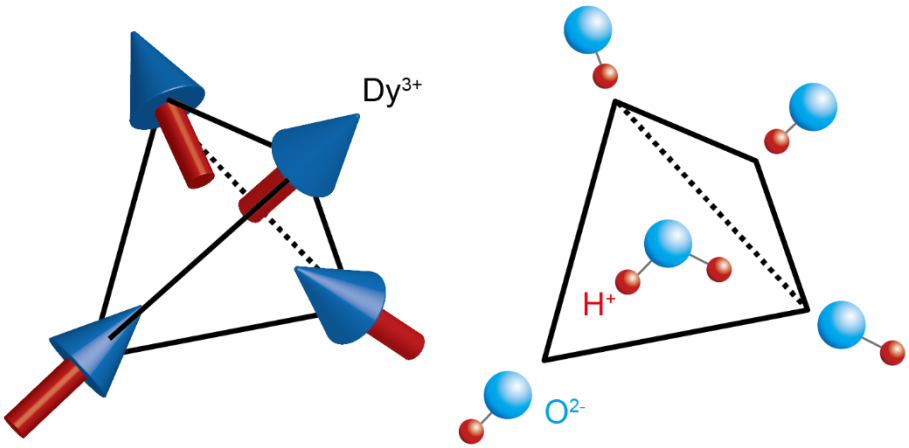

Figure 1.2 Schematic illustration of spin configuration of spin ice (left) and O-H bond configuration of the water ice.

One of the most astonishing consequences of the highly degenerate ground state of spin ice is the residual entropy when approaching absolute zero. Predicted by Pauling, water ice has a finite entropy of approximately $(Nk_B/2)\ln(3/2)$ due to the inequivalent O-H bond when forming a tetrahedron. Spin ice is the spin configuration analogue and, in this case, N is the number of spins of a system. Experimentally, the residual entropy has been successfully identified by specific heat measurements, as shown in the left panel of Figure 1.3. Indeed, by integrating $\int C/T \ dT$, spin ice yields a result of saturated entropy at $(0.67R)\ln2$ (R: ideal gas constant), implying a residual entropy at zero temperature close to the predicted $(R/2)\ln(3/2)$. This finding indicates that the ground state of DTO can be mapped onto water ice and is therefore considered to be the smoking gun for the existence of spin ice.

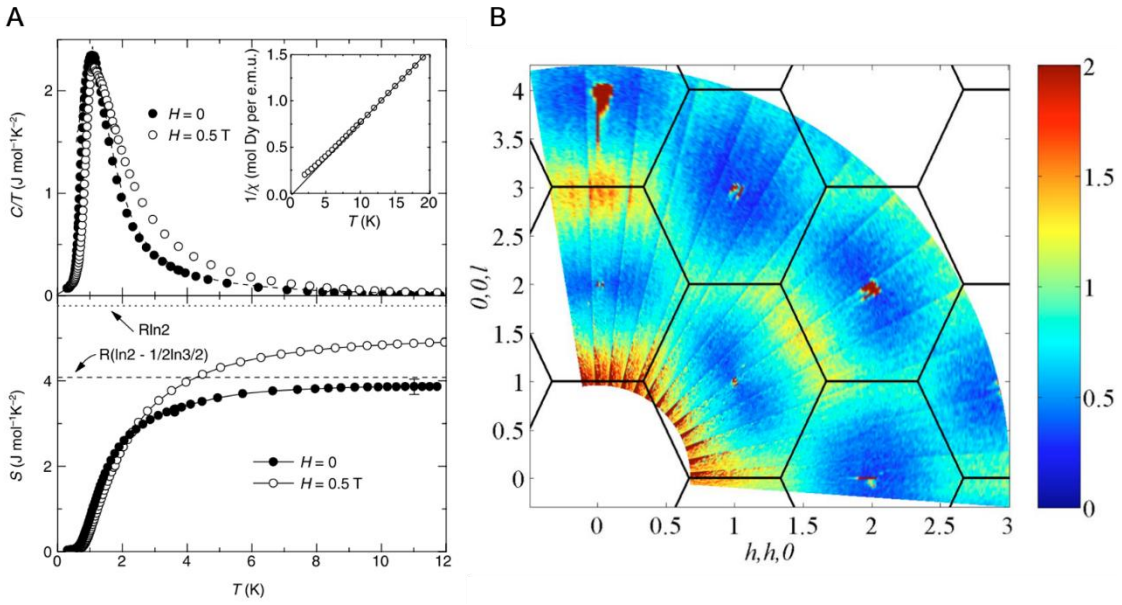

Figure 1.3 (A) Specific heat measurements of DTO (top left). The calculated entropy from integrating the specific heat over temperature $S = \int C/T \; dT$ (bottom left). The entropy shows a suppression about $(R/2)\ln(3/2)$ below the conventional molar entropy $R\ln 2$. Figure reproduced from ref. (*9*). (B) Neutron scattering spectra for DTO measured at $T = 0.3$ K, showing diffusive scattering and no indication of magnetic order. Figure reproduced from ref. (*8*).

1.2 Dipolar Interaction

Despite the success of the nearest neighbor spin ice model in describing the collective magnetic behavior in rare earth pyrochlores, it has been pointed out (*10*) that the dipolar interactions are non-negligible as they are stronger than the superexchange interaction in spin ice materials. This finding arouses another mystery how a complex magnet with strong long-range dipolar interaction can be well-described by the near neighbor spin ice model.

By including the long range dipole-dipole interaction term, we have dipolar spin

ice (DSI) Hamiltonian (*3*) as

$$\mathcal{H}_{\mathrm{DSI}} = J_{\mathrm{nn}} \sum_{\langle i,j \rangle} S_i S_j + D a^3 \sum_{i<j} \left[\frac{\vec{S}_i \cdot \vec{S}_j}{r_{ij}^3} - \frac{3(\vec{S}_i \cdot \vec{r}_{ij})(\vec{S}_j \cdot \vec{r}_{ij})}{r_{ij}^5} \right] \tag{1.3}$$

where r_{ij} is the distance between spins and $a \sim 3.57$ Å is the nearest neighbor distance in the tetrahedron of the pyrochlore lattice. *D* is the dipolar coupling constant with

$$D = \frac{\mu_0 \mu^2}{4\pi a^3} \sim 1.41 \text{ K} \tag{1.4}$$

The nearest-neighbor coupling constant J_{nn} is determined by comparing the simulation with experiments with $J_{\mathrm{nn}} \sim -1.2$ K for DTO (*11*). Evidently, the Hamiltonian is much more complicated than the simple near neighbor spin ice model. Despite the complexity, experiments (*9, 12*) have indicated that the dipolar interaction must somehow be self-screened since including the dipolar term does not seem to hinder the description of the spin ice state. The combination of the observations and the dipolar puzzle eventually led to the dumbbell model, marking the introduction of the elegant concept of the magnetic monopole excitation.

1.3 Magnetic Monopoles in Spin Ice

It is now clear the spin ice model has a ground state that fulfills the 2-in-2-out ice rule for each tetrahedron. Even more interesting physics lies in the excitation from this ground state. Due to its Ising nature, for the 4 spins in each tetrahedron, there are 16 states which correspond to the 2-in-2-out, 3-in-1-out/1-in-3-out, and all-in/all-out spin configurations. These yield energies of 0, +2*J*, and +8*J*, respectively. Therefore, the first elementary excitation that breaks the ice rule is by flipping a single spin and becomes the 3-in-1-out or 1-in-3-out state. Such an excitation can be generated by thermal fluctuation or by applying a magnetic field of a fraction of a Telsa along the [111] direction (*12, 13*).

At high temperature, these configurations (2-in-2-out, 3-in-1-out/1-in-3-out, and all-in/all-out) distribute thermodynamically and thereby forming a paramagnetic state.

It turns out that if we consider the magnetic moment with the underlying dipolar spin ice Hamiltonian as Eqn. 1.3, we can derive the existence of the fractionalized excitation (*1, 14*). This picture, which is the so-called dumbbell model, replaces one dipole moment along the local [111] direction by two opposite magnetic charges $\pm q_{\mathrm{m}} = 2\mu/a_{\mathrm{d}}$ (*14, 15*) at the center of a tetrahedron, where a_{d} is the diamond lattice bond length with $a_{\mathrm{d}} = \sqrt{3/2}a \approx 4.37$ Å for DTO. Mathematically, this rewrites the original dipolar term $\mathcal{H}_{\mathrm{dip}}$ in the Hamiltonian

$$\mathcal{H}_{\mathrm{dip}} = Da^3 \sum_{i<j} \left[\frac{\vec{S}_i \cdot \vec{S}_j}{r_{ij}^3} - \frac{3(\vec{S}_i \cdot \vec{r}_{ij})(\vec{S}_j \cdot \vec{r}_{ij})}{r_{ij}^5} \right] \tag{1.5}$$

into

$$\mathcal{H} = \sum_{i<j} \frac{\mu_0}{4\pi} \frac{q_{\mathrm{i}} q_{\mathrm{j}}}{r_{\mathrm{ij}}} \tag{1.6}$$

in the approximation to the order of $O(1/r^3)$, where the charge q_{i} has a value of $\pm q_{\mathrm{m}}$. Apparently, the converted Hamiltonian resembles the Coulomb interaction but in the magnetic version. Similarly, the Ising term yields the potential energy $v_0 q_{\mathrm{i}} q_{\mathrm{j}}$. v_0 is chosen to match the effective exchange interaction ($J_{\mathrm{eff}} = J_{\mathrm{nn}} + 5D/3$) of neighboring dipoles with

$$v_0 \left(\frac{\mu}{a_d}\right)^2 = J_{\mathrm{eff}} + \frac{4}{3}\left[1 + \sqrt{\frac{2}{3}}\right] D \tag{1.7}$$

The replacement of the Ising term and the dipolar term leads to an expression in terms of the magnetic charge. That is,

$$\mathcal{H} = \frac{\mu_0}{4\pi} \sum_{i<j} \frac{q_{\mathrm{i}} q_{\mathrm{j}}}{r_{\mathrm{ij}}} + \frac{v_0}{2} \sum_i q_i^2 \tag{1.8}$$

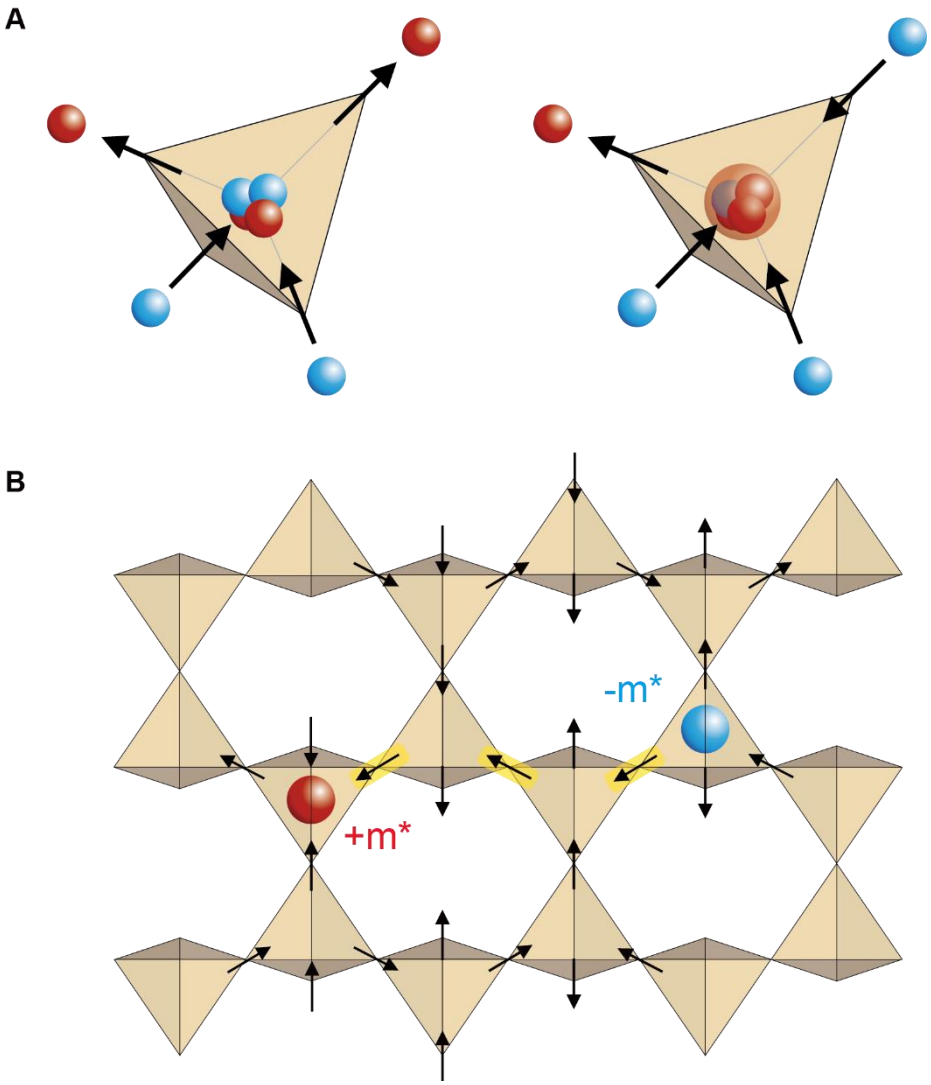

Figure 1.4 (A) Illustration of the dumbbell model. The magnetic dipole moments are mapped to positive and negative magnetic charges. Left: charge neutral scenario with 2-in-2-out spin configuration. Right: 3-in-1-out excited state with one positive charge at the center of tetrahedron. (B) Representation of an excited state with the generation of a pair of magnetic charges. Two magnetic monopoles with opposite charge are interconnected through the Dirac string.

The transformed Hamiltonian can be seen as a combination of magnetic Coulomb interaction and the on-site repulsive energy of magnetic charge. Clearly, the ground state will rule out the existence of the magnetic charge as $q_i = 0$ is favored energetically. The

simplest excitation, however, occurs when a single spin flips and breaks the ice rule for the two neighboring tetrahedra, leaving one tetrahedron with a 1-in-3-out configuration and another with a 3-in-1-out configuration. Based on the picture, such an excitation always generates a pair of magnetic monopoles with the opposite charge and thus the number of the positive charge is symmetric to that of the negative charge. Following a sequence of spin flips, the monopole pair can travel along the tetrahedra network or generate a new pair of magnetic charges throughout the crystal.

According to the magnetic monopole picture, the monopole interactions originate from the dipolar spin interactions, which is the key of the theory. Therefore, it is natural that the dipolar interaction does not alter the ground state as there is no magnetic charge residing at the lattice site. Therefore, the long-range interaction is screened, leaving the ground state with the same as the one described from the near neighbor spin ice model (*16*). Other interesting physics that is embedded in the magnetic monopole picture is the Dirac string. When the dipolar dumbbell is fractionalized into deconfined magnetic charges, the charges are actually attached to each other through a Dirac string (yellow in Figure 1.4 marks one possible choice of the Dirac string). Notably, the magnetic charge m of these topological defects is proposed to be $m = 2\mu/a_{\mathrm{d}}$, and thus is at least 3 orders of magnitude smaller than the Dirac monopole (*17*). Therefore, unlike the Dirac string from the fundamental magnetic monopole in vacuum being undetectable as postulated by Paul Dirac, the Dirac strings in spin ices are experimentally detectable. This main difference has led to the experimental search for magnetic monopoles through the signature of the Dirac string (*18, 19*).

1.4 The Search for Magnetic Monopoles

The idea of magnetic monopoles as the excitations in spin ice has aroused broader interest in the field of condensed matter physics as it offers a brand-new platform to study a unique type of excitation.

1.4.1 Magnetic Susceptibility, Neutron Scattering and μSR Study

In searches for the signature of the magnetic monopole excitation in spin ice, the community started from searching the signature of Dirac strings. For example, various magnetic susceptibility measurements were used to study the magnetic monopole flow in DTO (*20-26*). Especially for the AC field measurements, by locating the maximum in the frequency dependence of the out-of-phase magnetic response, this allowed the determination of the temperature dependent relaxation times for DTO. A typical measured relaxation rate for DTO is shown in Figure 1.5. Above 12 K, DTO is in the paramagnetic regime and the monopole description fails. Below 12 K, the measured relaxation rate follows the Arrhenius law with

$$\tau = \tau_0 \exp\left(\frac{2J_{eff}}{k_B T}\right) \tag{1.9}$$

where in the monopole picture $2J_{eff}$ is the energy cost for creating a pair of free monopoles (*18*). In Figure 1.5, the bulk susceptibility data were taken from ref. (*20*), while the red fitted line was plotted with the parameters obtained from ref. (*11*). Theoretically, the relaxation process can be explained by the generation-recombination process of the monopole with the diffusive motion constrained by the Dirac string (*18, 19*). The good agreement between the measured relaxation rate and the fitted line marks the validity of

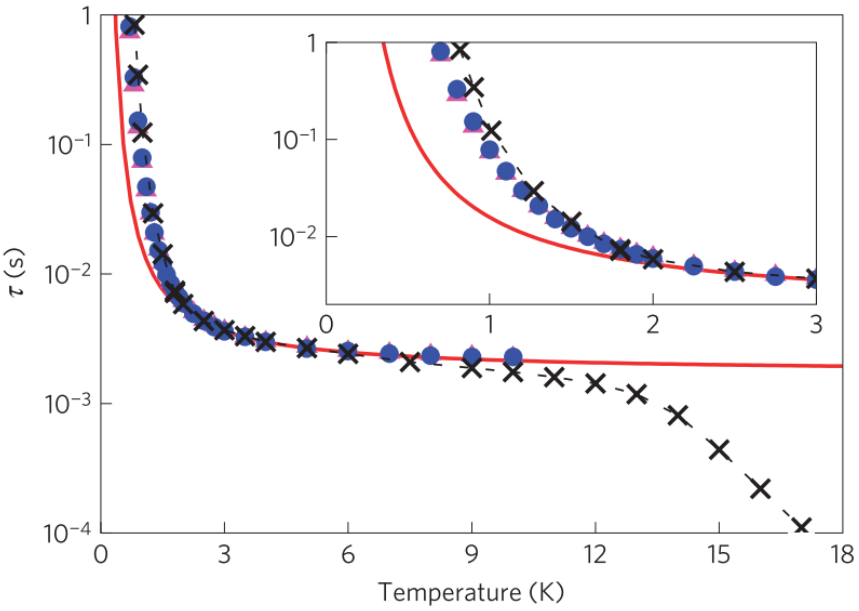

Figure 1.5 Experimentally measured relaxation time obtained from bulk AC susceptibility measurement for DTO (crosses). The red fitted line is the theoretical result from non-interacting diffusive motion of the free magnetic monopole excitations. Blue dots represent Monte Carlo simulation for the monopole model. Figure reproduced from ref. (*18*).

the monopole picture. Also, it can be deduced that monopoles enter the quantum tunneling regime from 4 K to 12 K when the relaxation rate shows a plateau region. That is, the relaxation time in this region is close to the monopole hopping rate, or the quantum mechanical spin flipping rate, which is about 85 μs. Noticeably, in Figure 1.5, some deviation between the experimental and theoretical results can be clearly observed below 1 K where the relaxation rate exhibits a super-Arrhenius law. The explanation of this leads to the discovery of the dynamical fractal transport of magnetic monopole (*27*) and the work of this thesis. In this thesis, I also examined the complex magnetic response with the AC field, and more details will be discussed in later chapters.

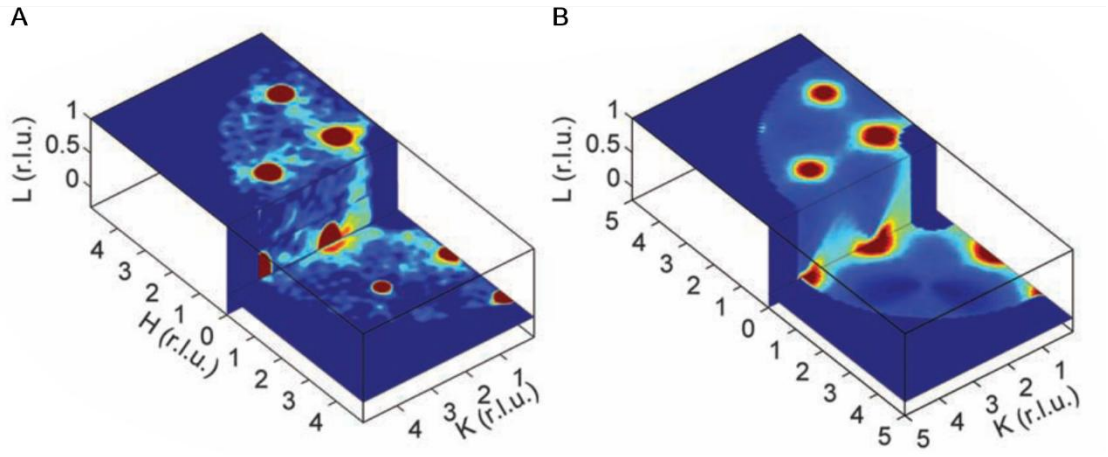

Figure 1.6 (A) 3D correlation data from neutron scattering at applied field around 0.5 T and 0.7 K, showing the predicted cone-shaped scattering pattern at (020). (B) The simulated result for scattering characteristic from random walk of dilute Dirac string with pyrochlore lattice. Figure reproduced from [D. J. P. Morris *et al.*, Dirac Strings and Magnetic Monopoles in the Spin Ice $Dy_2Ti_2O_7$. *Science* **326**, 411-414 (2009)] /Reprinted with permission from AAAS.

Another landmark confirming the diffusive nature of Dirac strings is the neutron scattering measurement under an external field along the [001] direction (*28*). Previously, many diffusive neutron scattering experiments had been performed (*8, 29*) and had confirmed the spin ice state with the absence of long-range magnetic order in zero field. Morris *et al.* (*28*) took a step further by applying an external magnetic field which almost completely magnetized the crystal. The magnetic field was chosen close to the 3D Kasteleyn transition (*30, 31*), with the experiment carried out slightly above 0.6 K, which is lower than the monopole pair energy. Indeed, at zero field, DTO is in a state with fluctuating monopole pair formation and Dirac strings. When the DTO crystal is magnetized, the ground state shifts to a unique 2-in-2-out state where the collective spin points along the [001] direction. This state is unfavorable by entropy but still satisfies the

ice rule. Since the DTO is almost but not completely magnetized, a small fraction of spins is able to flip with the help of thermal energy. In experiment, the sparse Dirac string executing a random walk monotonically in the [001] direction generates a unique scattering pattern. As shown in Figure 1.6, the 3D correlation measured by neutron scattering and the simulated result both show cone-like intensity patterns. Furthermore, as the field is reduced, the scattering pattern at (020) deforms back to the original pinch point observed in the zero field limit, indicating the Coulomb phase nature (*32*). Finally, by tilting the external field away from [001], the random walk of the Dirac string becomes biased and is observed experimentally. Based on all these results, the theoretical models based on the monopole picture agree with various experimental studies with external field excitation.

The magnetic susceptibility and neutron scattering studies were followed by pioneering muon spin rotation (μSR) research on DTO to investigate the quantity of magnetic charge (*33*). By drawing an analogy between the electrolyte in water ice and the magnetolyte in spin ice, it was hypothesized that the Wien effect could occur. In this scenario, the relaxation rate $\lambda(B)$ of the muon precession signal would follow the relation:

$$\frac{1}{\lambda(0)}\frac{d\lambda(B)}{dB} = \frac{\mu_0 m^3}{16\pi k_B^2 T^2} \tag{1.10}$$

where λ represents the decay rate of the μSR measurement. Through this equation, the magnetic charge m can be extracted using field-dependent μSR measurements. It was demonstrated that the Wien effect was observed in DTO, and the magnetic charge was measured in good agreement with theoretical predictions, within a narrow temperature range (<150 mK). However, subsequent controversy arose when another μSR

measurement (*34*) observed no transverse field precession, which aligns with both theoretical (*35, 36*) and experimental studies (*37*). It has been suggested that the μSR measurement that detected the Wein effect may have been influenced by stray fields from weakly magnetized DTO with the muon stopping in the silver sample holder. Ultimately, due to these controversies, the direct detection of magnetic monopole charge remains elusive and inconclusive.

1.4.2 SQUID Detection of Magnetic Monopoles

In 2018, a new proposal was introduced to detect the excitation of magnetic monopoles in spin ice without an external field (*38*). More specifically, it was proposed that by detecting the magnetic field fluctuation of monopoles with superconducting quantum interference device (SQUID) magnetometry, the power noise spectrum would exhibit characteristic frequency and temperature dependencies. This outstanding proposal sparked a series of studies on the magnetic monopole noise and eventually led to the primary works of this thesis.

In the following year after the proposal, it was demonstrated that the spin ice material DTO indeed exhibits the characteristic noise spectrum (*39*). The core idea of the experiment is to detect the flux of a magnetic monopole traveling through a pickup coil linking to a SQUID (Figure 1.7A). For instance, for a magnetic monopole with a charge of *m,* the flux $\Phi = \mu_0 m$ will be generated when the charge passes through. The SQUID converts a flux signal threading the superconducting coil into the measurable voltage signal. Ideally, the superconducting coil picks up one magnetic charge at a time and hence the recorded flux shows a constitution of step fluxes. However, in the spin ice material,

due to the combination of the random walk nature of monopoles and the rapid thermal activated generation-recombination process of monopole pairs, an excess of flux noise is expected (Figure 1.7C and D). By recording the time series of fluctuating voltage *V*(t) from a SQUID, the fluctuation in the flux and its power noise spectrum can be reconstructed.

In fact, the noise source of the magnetic monopoles in spin ice resembles that of the generation-recombination noise from the electron-hole pair of an intrinsic semiconductor (*40-42*) with a shift in the noise power. Accordingly, at the thermal equilibrium, the generation of monopole pairs reaches a dynamic equilibrium with the recombination rate. That is,

$$g(N,T)|_{N_0} = r(N,T)|_{N_0} \tag{1.11}$$

where N_0 is the average number of monopoles, and $g(N,T)$ and $r(N,T)$ represents the generation and recombination rates, respectively. The number fluctuation of the monopole pairs $\delta N = N - N_0$ owing to the generation-recombination process is governed by the Langevin equation (*43*) that

$$\frac{d(\delta N)}{dt} = -\frac{\delta N}{\tau_{GR}(T)} + \sqrt{P(T)}\varsigma(t) \tag{1.12}$$

$\sqrt{P(T)}\varsigma(t)$ is the unit white noise with the noise power $P(T)$ as it has been widely believed that this random process has Gaussian distribution (*43*). The relaxation rate of the generation-recombination process is denoted as τ_{GR} with

$$\tau_{GR}(T) = 1/(\frac{\mathrm{d}r}{\mathrm{d}N} - \frac{\mathrm{d}g}{\mathrm{d}N})|_{N_0} \tag{1.13}$$

The Langevin equation yields a power spectrum of

$$S_N = \frac{4\sigma_N^2 \tau_{GR}(T)}{1+\omega^2\tau_{GR}^2(T)} \tag{1.14}$$

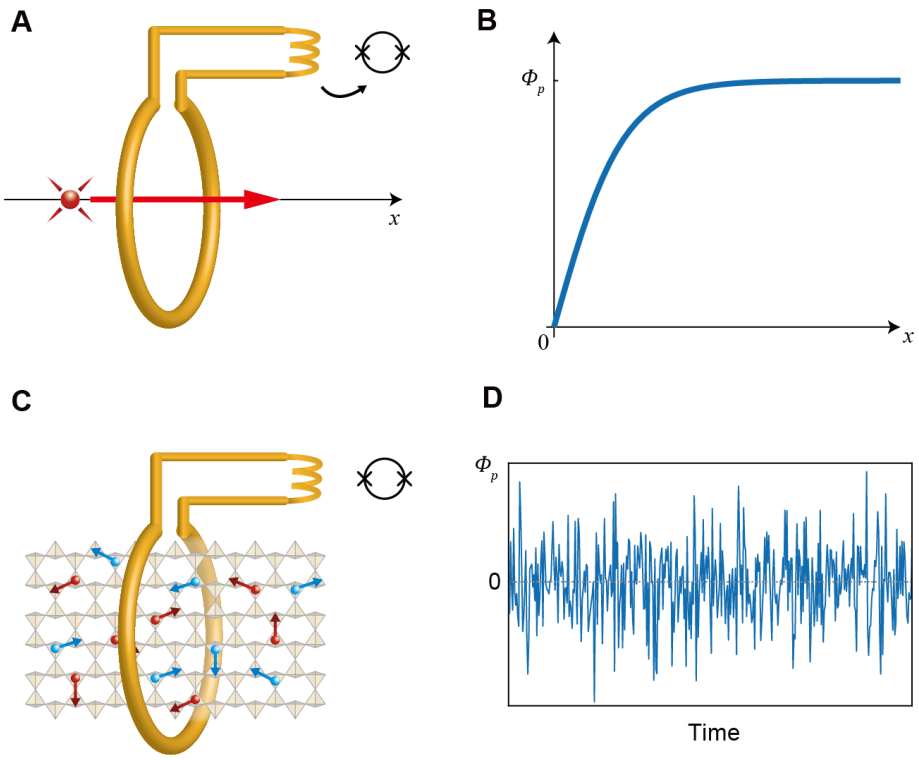

Figure 1.7 (A) Schematic illustration of a magnetic charge traveling through the superconducting pickup coil. The flux threading the coil is transferred to the input coil and is then sensed by SQUID. (B) The flux picked up by the coil when a magnetic charge passing through as a function of x. (C) Schematic illustration of the random walk of monopole fluids in spin ice. (D) The illustration of the expected flux noise from the generation-recombination process of magnetic monopoles in spin ice.

where σ_N^2 is the variance (*43*). Since the magnetic monopole pairs are connected through the flux $\Phi = \mu_0 m$, it is argued (*39*) that the flux noise threading the superconducting coil is proportional to the number fluctuation $S_\Phi \propto S_N$. Indeed, the Monte Carlo simulation yields a flux noise spectrum which generally follows formula form (eqn. 1.14) and the characteristic frequency dependence (Figure 1.8A).

Experimentally, the magnetization noise measured by the SQUID corroborates the

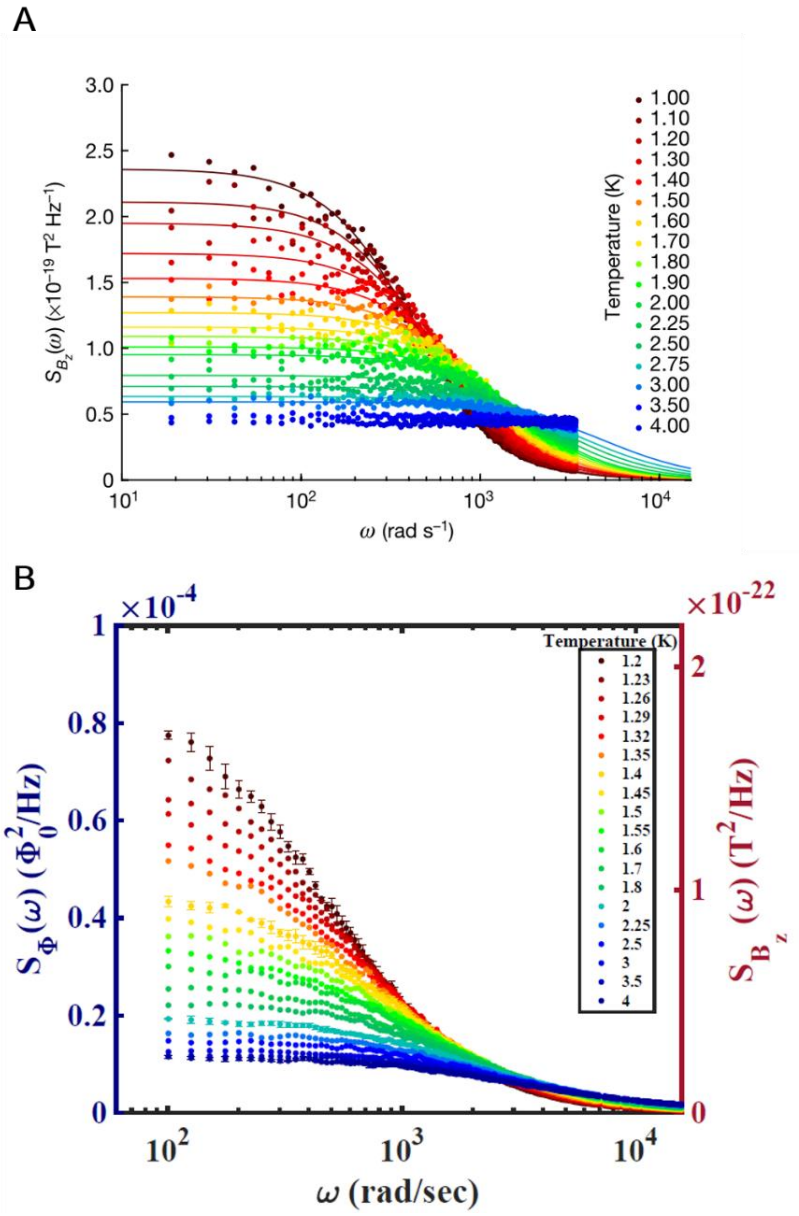

Figure 1.8 (A) The predicted spectral density of magnetic field fluctuation of DTO from Monte Carlo simulation. (B) Measured spectral density of magnetic flux fluctuation from a superconducting coil winding around the DTO. Figure reproduced from ref. (*39*).

theoretical expectations of the overall power noise spectral shape (Figure 1.8B). Interestingly, the power spectral density (PSD) is best fitted with a spectral form of

$$S_\Phi(\omega, T) = \frac{4\sigma^2 \tau_{PSD}(T)}{1+\omega^b \tau_{PSD}^b(T)} \tag{1.15}$$

where b is the additional exponent that is closely related to the color of the noise spectrum. Note that eqn. 1.15 differs from eqn. 1.14 with a change to the exponent. From eqn. 1.14, the exponent predicted by the random walk is 2. Theoretical models based on the nearest neighbor spin ice or dipolar spin ice model also predicts an exponent at 2 or slightly smaller than 2. However, the measured exponent $b(T)$ shows a significant deviation ranging from 1.1 to 1.5 between 1.2 K$<T<$4 K. This deviation implies that the fundamental magnetic monopole dynamics is more complex than the existing theory. Nevertheless, the general agreement between the theoretical and measured spectral density strongly supports the picture of a magnetic monopole fluid in spin ice. Furthermore, the flux noise spectroscopic technique demonstrated by Dusad *et al.* opens a series of research on magnetic noise, including the works of this thesis.

Over the past two decades, physicists have solved numerous conundrums in the spin ice materials, including the screening of dipolar interaction and the brilliant idea of magnetic monopole excitations. Various experiments mentioned above also corroborate the magnetic monopole fluid in the spin ice materials. Despite this huge success, several mysteries remain open. For example, AC susceptibility experiments on $Dy_2Ti_2O_7$ torus sample contradicted the expectation from the predictions of the Debye picture (*21, 44*). Additionally, experiments scrutinizing the muon relaxation rate (*34*) and low temperature specific heat (*45*) reveal controversies regarding the true ground state of spin ice. Thus, an experimental technique to explore how the monopole fluid transitions from a supercooled state to glassy dynamics, potentially identifying hidden phases of matter, is strongly needed. Lastly, the mysterious exponent b ~1.5 in the noise spectrum (*39, 46*), which is surprising and unexpected from the paramagnetic random walk, sheds light on a

more precise microscopic picture of the monopole dynamic. This thesis aims to provide experimental evidence for a new regime towards the ground state of the monopole fluid and to explore the new paradigm of monopole transport.

Chapter 2 Magnetic Monopole Transport Theory

The transport properties of the magnetic monopole fluid in spin ice are the central focus of this thesis. In this chapter, I first provide a comprehensive description of the classical dynamic theory for the free magnetic monopole plasma. This non-interacting theory forms a crucial foundation for later developments, including Debye-Hückel theory (*47*) and Onsager's equation (*48*), which are adapted to the spin ice magnetolyte from the dynamic theory of electrolytes in water solutions. In the second half of the chapter, I introduce a new microscopic transport theory, inspired by the recent discovery of the anomalous exponent from magnetic noise measurements. The modified theory incorporates interactions with additional neighboring lattice sites and integrates a second spin-flipping rate (*49*). Remarkably, this approach reveals a dynamical fractal pattern emerging from the hopping of magnetic monopoles, which accounts for the observed diverging relaxation time (*27*).

2.1 Dynamics of Free Magnetic Monopole Fluid

Perhaps the simplest formulation for magnetic monopole dynamics in spin ice is derived from the near neighbor spin ice model. The fundamental assumption is that monopole diffusion, via site-to-site hopping, originates from the spin flipping process between 2-in-2-out states and 1-in-3-out/3-in-1-out states. Furthermore, the spin ice is treated as weak magnetolyte, meaning the monopole density is dilute and monopoles are non-interacting over long distances throughout the crystal. Ryzhkin (*15, 50, 51*) developed a monopole transport theory based on Jaccard theory, mapping the ice

configuration to pyrochlore lattice. Accordingly, the governing equation of the monopole motion is expressed as

$$j_m = \frac{dM}{dt} \tag{2.1}$$

where j_m is the monopole current density driven by the field $H - M/\chi$ with the existence of an external field H and magnetic suceptibility χ. That is, the monopole current in the diffusive regime can be deduced from the magnetization. Moving forward, one can define a local spin configuration vector field Ω of spin ice in a microscopic volume ν as

$$\Omega \equiv \frac{\mu}{2}\sum_{i\eta}\frac{\sigma_{i\eta}\boldsymbol{e}_{i\eta}}{\nu} \tag{2.2}$$

where i and η label each tetrahedron and each of its vertices. $\sigma_{i\eta} \equiv \pm 1$ represent the Ising spins with moment μ pointing towards/away from each tetrahedron center along the relevant unit vectors $\boldsymbol{e}_{i\eta}$. It is clear that the passage of a monopole changes Ω and thus the configuration vector is directly related to monopole current density as $\Omega(\mathrm{t}) = \int_0^t j_m(t')dt'$. Also, the configurational entropy per volume (*52*) can be derived from Ω as

$$S_c(\Omega) - S_c(0) = -\frac{8}{\sqrt{3}}a_d k_B \frac{|\Omega|^2}{m^2} \tag{2.3}$$

Therefore, if an external force field $f_H \equiv \mu_o H$ is imposed on a magnetic charge, thermodynamically, the power flow should combine the work done by the magnetic force and the change of configuration entropy from. More explicitly,

$$T\dot{S}_c(H) = \mu_o j_m \cdot H + T\dot{S}_c(0) \tag{2.4}$$

By using Eqn, 2.3, the expression can be further reduced to

$$T\dot{S}_c(H) = \mu_o j_m \cdot H - \frac{16akT}{\sqrt{3}m^2}\Omega \cdot \dot{\Omega} = \mu_o j_m \cdot H - \frac{16akT}{\sqrt{3}m^2} j_m \cdot \Omega \tag{2.5}$$

For simplicity, we define Σ as

$$\Sigma \equiv \frac{16a_d k_B T}{\sqrt{3}}. \tag{2.6}$$

and consider Σ a parameter set by the mapping to the ice configuration. Thus, the generalized force fields can be represented as

$$T\dot{S} = j_m(\mu_o H - \frac{\Sigma\Omega}{m^2}) \tag{2.7}$$

where $\mu_0 H - \Sigma\Omega/\mathrm{m}^2$ can be regarded as the effective force field. A master equation set for the monopole dynamics can be derived based on the Jaccard theory and Maxwell equations (*51*).

$$j_m + D\nabla\rho = \sigma_m(\mu_o H - \frac{\Sigma\Omega}{m^2}) \tag{2.8}$$

$$\partial\rho/\partial \mathrm{t} = -\nabla \cdot j_m \tag{2.9}$$

Here, D is the diffusion coefficient. ρ is the charge density of monopoles, and σ_m is the monopole conductivity. Eqn. 2.8 is the general transport equation for the magnetic monopoles with the consideration of the opposing entropic force, while Eqn. 2.9 is the continuity equation for the monopole fluid. On the left hand side of Eqn. 2.8, the monopole current consists of the drift current j_m and the diffusion current $D\nabla\rho$, assuming the spin ice is in a non-equilibrium state with an inhomogeneous monopole distribution. On the right-hand side, the first term is analogous to Ohm's law of electric current, $j_e = \sigma_e E$, indicating a linear response to the external field. From Eqn. 2.7, the entropy causes the force field $\mu_0 H - \Sigma\Omega/\mathrm{m}^2$ to reduce from $\mu_0 H$. Thus, the entropic force, comprising Σ and the configuration vector Ω, is proportional to the temperature. Note that Eqn. 2.8 is approximate in the sense that the chemical kinetic (i.e. generation-recombination process) is excluded and the bound pair formation are not considered.

Interestingly, the conduction of magnetic monopole in spin is inevitably accompanied by the self-magnetization, or the self-screening. Based on Eqn. 2.8, the

monopole current ceases, and equilibrium is achieved when the average force field on the magnetic monopole is zero. That is,

$$\mu_o H - \Sigma\Omega/m^2 = 0 \tag{2.10}$$

Solving the equation leaves an expression of the magnetic charge proportional to the magnetization for a given external drive field.

$$m^2 = \frac{16 a_d kTM}{\sqrt{3}\mu_0 H} \tag{2.11}$$

Therefore, the equilibrium state can be used to measure the magnetic charge directly. The explicit derivation with experiment-related parameters (apparatus-related parameters) is further discussed in Chapter 6.

2.2 The Puzzles of Magnetic Monopole Dynamics

The classic theory of the magnetic monopole dynamics in spin ice posits that the topological defects, which can be described as magnetic monopoles, behave as an idealized monopole fluid. Before 2018, it was often assumed that the diffusion of magnetic monopoles follows Brownian motion (*43*), without considering monopole interactions. In this framework, magnetic monopole diffusion is expected to be non-interacting and to follow a simple random walk. However, recent experimental studies have raised two major puzzles that challenge this classical theory, including adiabatic susceptibility measurements (*23*) and magnetic monopole noise measurements (*39*). First, measurements on relaxation time (*20-22, 24, 45*) reveal a diverging super-Arrhenius trend at low temperature especially when the monopoles enter a supercooled state. How monopole dynamics evolve from a fluidic state to supercooled and eventually showing glassiness is inexplicable by conventional monopole transport theory. The second puzzle

is that the direct magnetization noise experiments (*39, 46*) unravel the anomalous exponent b of power noise spectrum $S(\omega) \sim \omega^{-b}$, indicating that the magnetic monopole motion deviates from the Brownian motion. More explicitly, the monopole dynamics based on a Brownian random walk inevitably leads to an exponent $b = 2$. Even for the Hamiltonian that accounts for the thermodynamic properties of the canonical spin ice (*53*), the simulation with single rate spin flip leads to an exponent of 1.8-1.9 (*46*). Thus, the observed exponent $b \sim 1.2$-1.5 implies the motion to be in the sub-diffusive regime and hence a different microscopic monopole dynamic. To explain the 'color' of the magnetic monopole noise (b is called the color of noise here since $b = 2$ is conventionally called the red noise, while $b = 0$ is called the white noise), various theoretical approaches considering multiple relaxation timescales have been proposed, despite the lack of a microscopic picture (*54, 55*).

2.3 Dynamical Fractal Transport Theory

A critical clue appears from the theoretical simulations, which discovered the emergence of a bimodal transverse field distribution when considering more neighbor sites and different spin configuration subsets (*49*). Combining this observation and the concept of multiple relaxation times, a new microscopic theory of magnetic monopole transport has been proposed. Instead of the standard model (SM) which assumes a single spin flip rate, the new theory called beyond the standard model (bSM) considers two distinct spin configurations involving two tetrahedra. As shown in Figure 2.1, the center spin experiences different transverse field strengths (0 T and 0.45 T calculated from the nearest 6 spins) due to the parallel or anti-parallel alignment of the magnetic field from the upper and lower tetrahedron. For example, on the left panel, the upper tetrahedron

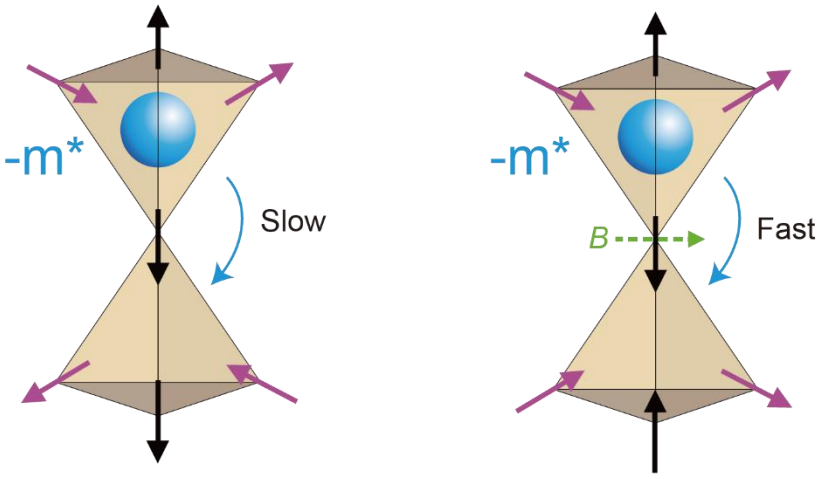

Figure 2.1 Spin configuration of two tetrahedra in spin ice with a single monopole. The left scenario represents the spin configuration where the transverse field vanishes. In the right panel, a finite transverse field from 6 neighboring sites enable the spin flip and thereby causing a fast spin flip rate.

with a transverse field points to the right, while the lower tetrahedron's transverse field points to the left, resulting in no effective transverse field on the center spin. On the other hand, in another configuration of the right panel, a net transverse field is imposed on the center spin, which can be expressed from the superposition of 6 spins as

$$B_{dip}(0) = \frac{\mu_0 |m^*|}{4\pi r_{nn}^3} \sum_{j=1,2,3} (\hat{z}_j + \sqrt{6}\hat{r}_j)\,(S_j + S_{j+3}) \tag{2.12}$$

where the spin pairs $(S_j,\ S_{j+3})$ from the upper and lower tetrahedron have the same anisotropies $\hat{z}_j = \hat{z}_{j+3}$ and $r_j = r_{nn}\hat{r}_j$. For randomly distributed spins, 2/3 of cases result in a finite transverse field acting on the centre spin. The presence of the transverse field assists the spin flip between the 3-out-1-in state and the 2-in-2-out state with a spin relaxation rate τ_{fast}. Otherwise, the spin experiences an energy penalty without the transverse field and thereby leading to a slower spin flipping rate τ_{slow}. Consequently,

when a magnetic monopole diffuses throughout the spin ice material, it continuously passes between the τ_{slow} and τ_{fast} configurations as if navigating through a maze. It was realized that with the existence of the extra τ_{slow} spin flipping rate, the trajectory of monopole becomes a dynamical fractal, and thus the monopole hopping dynamic becomes sub-Brownian (*27*).

2.3.1 Monte Carlo Simulation

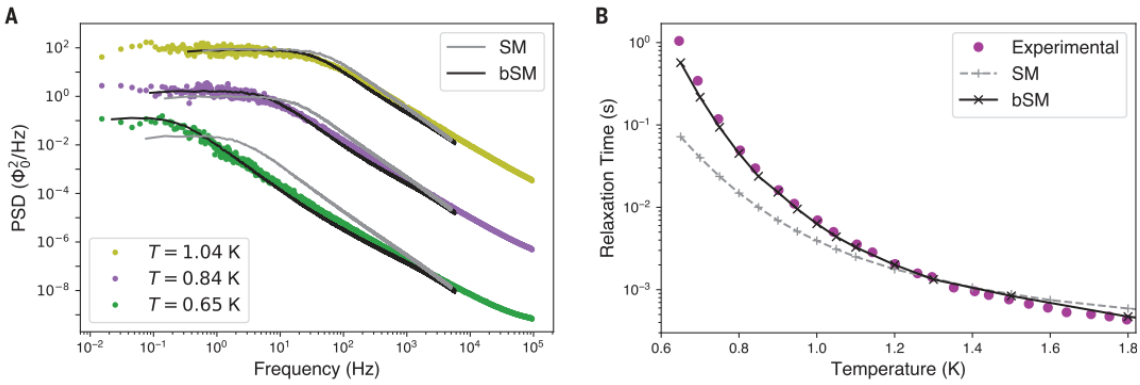

Figure 2.2 The simulated magnetic noise and relaxation time from Ref. (*27*). (A) Comparison between SQUID-measured PSD (filled circle) and simulated results based on SM and bSM (grey). (B) Relaxation rate extracted from the fit to the experiments and the simulated results. Figure from [*Science* **378**, 1218-1221 (2022)] / Reprinted with permission from AAAS.

A Monte Carlo (MC) simulation study has been performed in Ref. (*27*) on monopole dynamics and its magnetic noise, incorporating the two different timescales. More specifically, the simulation is based on the Hamiltonian consisting of short-range exchange and long-range dipolar interaction between the first, second, and third-neighbor spins

$$\mathcal{H}_{\mathrm{OP}} = Da^3 \sum_{i<j} \left[\frac{\vec{S}_i \cdot \vec{S}_j}{r_{ij}^3} - \frac{3(\vec{S}_i \cdot \vec{r}_{ij})(\vec{S}_j \cdot \vec{r}_{ij})}{r_{ij}^5} \right]$$

$$+ J_1 \sum_{\langle i,j \rangle} \vec{S}_i \cdot \vec{S}_j + J_2 \sum_{\langle i,j \rangle_2} \vec{S}_i \cdot \vec{S}_j$$

$$+ J_3 \sum_{\langle i,j \rangle_3} \vec{S}_i \cdot \vec{S}_j + J_{3'} \sum_{\langle i,j \rangle_{3'}} \vec{S}_i \cdot \vec{S}_j \qquad (2.13)$$

where the exchange strengths are J_1 = 3.41 K, J_2 = 0.0 K, J_3 = −0.00466 K, and J_3' = 0.0439 K and the dipolar interaction strength is D = 1.3224 K/a^3. These parameters were obtained by fitting to the neutron scattering, specific heat measurements and magnetic susceptibility data (*53*). The monopole dynamics were simulated with a reference of time τ_{fast} as one MC step.

Figure 2.2A shows the simulated magnetic noise from the bSM Hamiltonian adapted from Ref. (*27*). It was discovered that by choosing τ_{fast} to be 85 μs and $\tau_{slow}/\tau_{fast} \rightarrow \infty$, the simulated magnetic noise reaches outstanding agreement with the experimentally measured power noise spectrum $S(\omega) \sim 1/(1 + (\omega\tau)^b)$. It is remarkable that such a simple inclusion of a longer timescale can account for the anomalous exponent *b*~1.2-1.5 so accurately. Furthermore, at the temperature below 1 K, the contribution of τ_{slow} significantly affects the macroscopic experimental relaxation time. Despite 1/3 of spin configurations having enough thermal energy for spin flipping, the absence of transverse field slows down the process, leading to the super-Arrhenius law at lower temperatures. The mechanism successfully explains how the relaxation rate tends to become slower than expected, which is a long-standing puzzle in the spin ice community (*20, 21, 24, 25, 39, 46*).

What is even more intriguing is that linking the sites reachable by successive hopping of an isolated magnetic monopole in spin ice yields a fractal cluster. As shown

in Figure 2-3, the number of sites that an isolated magnetic monopole can visit is significantly sparser in the bSM model compared to the SM model. It was also found that the number of reachable sites defines a percolation problem that grows with $n^{1.85}$ (n: number of Monte Carlo steps), which is very close to the critical percolation. This fractal dimension is the key to cause the exponent of magnetic noise to b = 1.5. Notably, up to the critical step $n_{cr} = 14$, the system crosses over to the conventional 3D behavior n^3 at larger scales. This suggests that under a sudden field excitation, the motion of the magnetic monopole fluid starting from the equilibrium will show a cross-over in magnetization response.

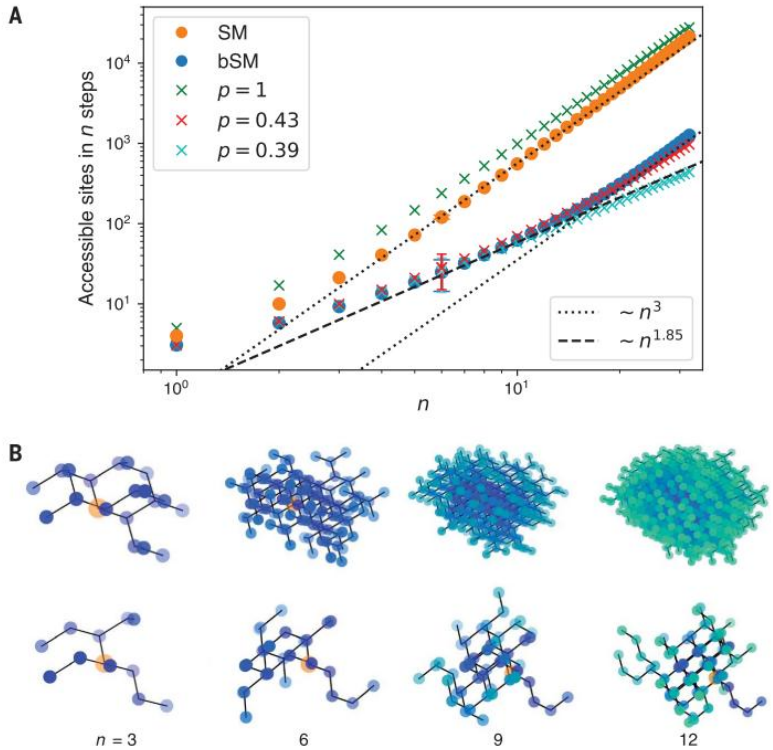

Figure 2.3 The dynamical fractal cluster formed by isolated monopole. (A) Number of sites reachable by a given steps with SM (orange) and bSM model (blue). (B) Visualization of fractal cluster of SM (upper) and bSM model (lower). The starting point is marked by the orange. Figure from [*Science* **378**, 1218-1221 (2022)] / Reprinted with permission from AAAS.

2.3.2 Theoretical Prediction

The dynamical fractal has become extremely successful to explain two mysteries from the magnetic noise measurements – the anomalous exponent and the diverging relaxation rate. However, no other positive definite evidence supports this advanced theory. Jonathan. N. Hallén later simulated the magnetic response under various magnetic field conditions. Confirming or falsifying the theory by comparing the theoretical predictions with experimental results has become one of the major motivations behind the work of this thesis.

Monte Carlo simulations have been performed to study monopole current dynamics of the bSM model in two essential cases: (1) monopole current driven from the *instantaneous change* in the applied field from the equilibrium state, and (2) monopole currents driven by a *sinusoidal* oscillating field. Notably, the parameters of the Hamiltonian are set the same as in Ref. (*27*). On the other hand, the simulated external field is on the order of ~10 mT for better signal-to-noise ratio. Overall, the Monte Carlo simulation predicts striking dichotomous signatures of monopole current dynamics that in both scenarios a clear transition is observed in real-time magnetization and the frequency dependence of complex conductivity.

Instantaneous applied field

The pivotal microscopic difference between SM and bSM for the monopole current dynamics under an applied field is the presence of the so-called termini (*56*). Monopole termini happen when magnetic monopoles are trapped in a spin configuration where the nearest 2-3 neighboring tetrahedra have vanishing transverse field. The

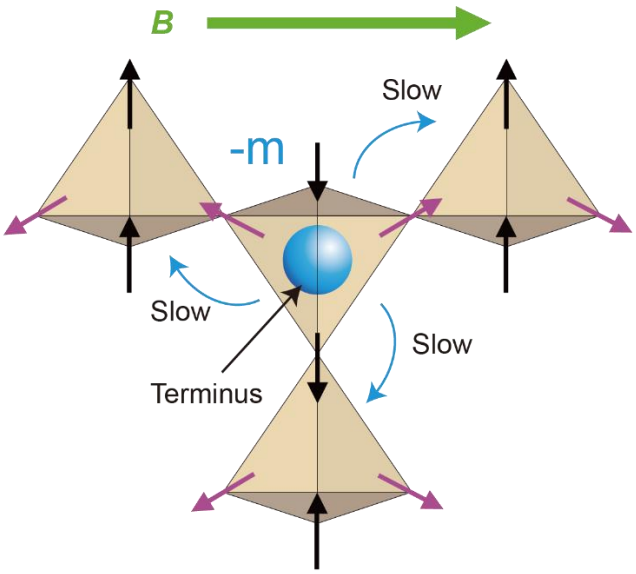

Figure 2.4 Schematic illustration of a magnetic monopole terminus.

monopoles are thereby forced to move along the direction which is energetically unfavorable by the external field. Figure 2-4 shows the schematic illustration of a monopole terminus where an isolated monopole is trapped by the slow spin flipping configuration. Under the sudden change of field, the monopole motion is predicted to be bifurcated into two distinct channels, as *reconfiguration* and *polarization* current. The reconfiguration current involves rapid short-range reconfigurations of monopoles (rapid change of 2-in 2-out configuration) and the burst of creation of extra monopole pairs. The monopole motion follows the constraint from the local termini, and the reconfiguration current amplitude decays with the intrinsic spin flipping rate $\tau_R \sim \tau_{fast}$ (see Figure 2.6, reconfiguration current happens mostly before t = τ_R). The polarization current, on the other hand, changes the polarization of the macroscopic system as the monopoles transport over larger distances. Such diffusive motion decays on another characteristic timescale τ_P. In combination, the simulated result of the monopole current dichotomy is

shown in Figure 2.5.

In Figure 2.5, $t = 0$ marks the time when the magnetic field is suddenly turned on. The magnetic response is subtracted by the equilibrium value of magnetization M_{sat} in the long time limit in order to compare with the trivial exponential decay. At all the temperatures where the monopole model is valid, a vivid transition can be seen at the beginning, indicating the fast-decaying reconfiguration dominated by τ_{fast}. Notably, the inset demonstrates the sharp contrast of the simulated results from bSM (blue) and SM model (orange). In the SM simulation where there is only single timescale, reconfiguration does not exist. Thus, with the absence of the reconfiguration current, the conventional SM model shows merely the exponential decay of the polarization process. In his simulation, Jonathan Hallén also calculated the time-dependent proportion of monopoles in termini, with respect to a given driving field. For simplicity, a monopole terminus is defined to be positive if it is trapped along the preferred direction, while it is negative if it cannot move in the opposite direction to the applied field. The proportion of positive and negative termini are denoted as γ_+ and γ_-, respectively. In Figure 2.6, a magnetic field is applied at $t = 0$. Initially, $\gamma_+(\gamma_-)$ rapidly increases/decreases. This originates from the immediate movement of the monopole reconfiguration and reaches its maximum (minimum) after a time $\tau_{\mathrm{R}} \sim \tau_{\mathrm{fast}}$. The secondary effect becomes obvious when γ_+ and γ_- start to decay with a longer timescale τ_{P}, which contributes to the overall polarization. The monopole termini reach the final state with $\gamma_- > \gamma_+$ due to the energetic preference to magnetic field.

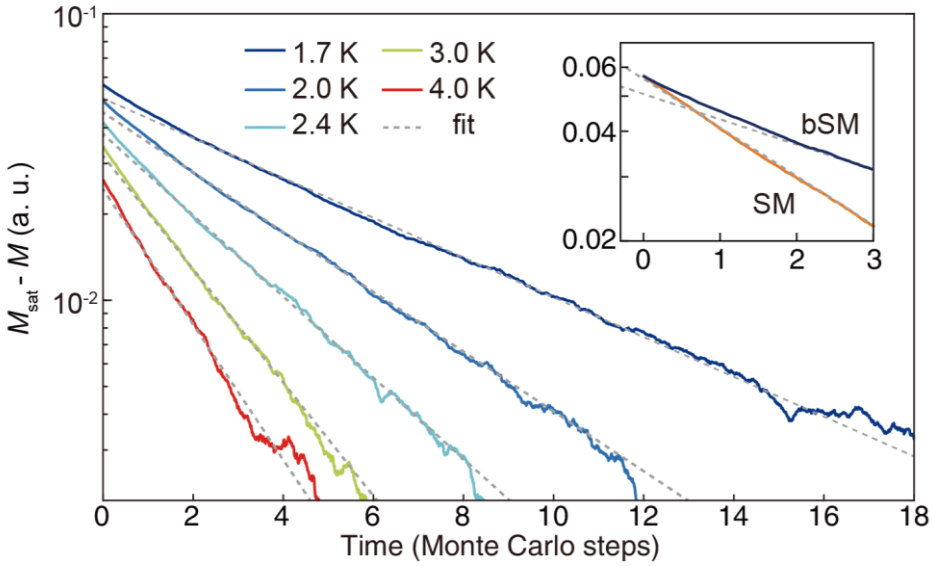

Figure 2.5 Monte Carlo simulation of magnetization response in time domain with an external field of 30 mT applied at $t = 0$. The main panel shows the simulated bSM results at 1.7 K, 2.0 K, 2.4 K, 3.0 K, and 4.0 K with the long-time fit (dashed grey) guided to eye. The inset contrasts the magnetic response of SM (orange) and bSM (blue) at 1.7 K (*56*).

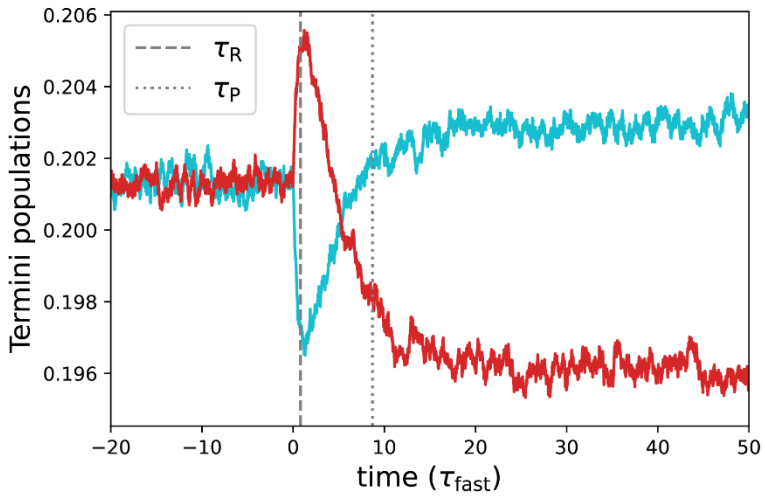

Figure 2.6 The simulated populations of monopole terminus for positive charge (γ_+, red) and negative charge (γ_-, cyan) at 2.2 K. The 15 mT magnetic field is applied at $t = 0$, causing the reconfiguration to occur with the timescale τ_R, followed by the gradual decay of population with another longer timescale of τ_P (*56*).

Oscillating field

Similar to the step-wise application of magnetic field, the magnetic response from the oscillating field also reflects the dichotomy of reconfiguration and polarization current. For an AC monopole current $J(f) = \mathrm{Re}J_f + i\mathrm{Im}J_f$, the loss angle is defined as $\theta(f) = \arctan(\mathrm{Im}J_f/\mathrm{Re}J_f)$. The predicted loss angle is shown in Figure 2-7, where the loss angle $\theta(f)$ is extracted from the magnetization $m(t) = m_0\, sin[2\pi ft + \theta(f)]$ under oscillating field $B(t) = B_0\, cos(2\pi ft)$ with $B_0 = 30$ mT. Intuitively, for the frequency dependence, the magnetization response is dominated by the reconfiguration current/polarization current for the low frequency ($f < 1/\tau_{\mathrm{P}}$) and high-frequency ($f > 1/\tau_{\mathrm{fast}}$) limit. In the intermediate frequency range $\tau_{\mathrm{P}}^{-1} < f < \tau_{\mathrm{R}}^{-1}$ where the interplay of two current dichotomy becomes crucial, a significant bump-like feature can be seen centered at $f \sim \tau_{\mathrm{fast}}$. At the intermediate frequency, magnetic response is interesting in that a proportion of monopoles is driven into and out of the termini continuously, while at the high frequency limit, the direction of field alters too fast for most of monopoles to reach termini. Thereby, the loss angle saturates similarly for all temperatures. Conversely, at the low frequency limit, the monopoles trapped in termini remain in equilibrium and the monopole current oscillates out-of-phase ($\pi/2$) with the external field. The inset of Figure 2.7 highlights the difference of SM (square) and bSM (circle). Without the monopole termini, the significant feature disappears at intermediate frequency. Furthermore, this characteristic frequency is more apparent at lower temperature where τ_{fast} & τ_{slow} are further from each other.

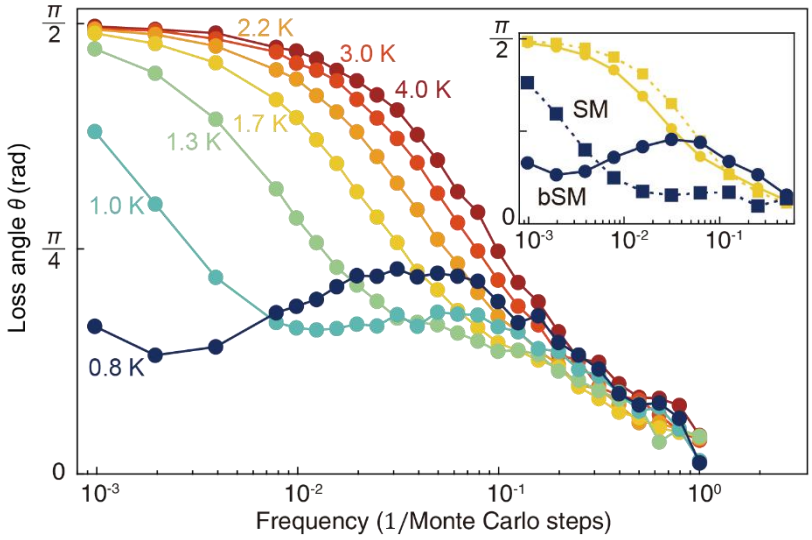

Figure 2.7 The simulated loss angle extracted from the magnetization $m(t) = m_0\, sin[2\pi ft + \theta(f)]$ under oscillating field $B(t) = B_0\, cos(2\pi ft)$. The temperature varies from 0.8 K (dark blue) to 4.0 K (dark red). The inset shows the comparison of the loss angle in SM (square) and bSM (circle) model at 0.8 K and 1.7 K, highlighting the presence of the stark bump-like feature corresponding to $1/\tau_{\text{fast}}$.

2.4 Fluctuation-Dissipation Theorem

So far, we have discussed the monopole transport theory that is based on the microscopic picture. Now I would like to turn our attention to the monopole transport properties in the view of statistical physics. In particular, the fluctuation-dissipation theorem (FDT) links the fluctuations at equilibrium of physical quantities to the linear response of the system to a weak applied force. Namely, for a system with a physical observable $\mathbb{C}$ and its linear response to a finite field ξ conjugate to $\mathbb{C}$, the Hamiltonian can be written as

$$\mathcal{H}(\xi) = \mathcal{H}(0) - \xi\mathbb{C} \tag{2.14}$$

In equilibrium, FDT provides a relation between fluctuation and the linear response when the linear response meets

$$\chi_{\mathbb{C}} = \mathbb{C}/\xi \tag{2.15}$$

where $\chi_{\mathbb{C}}$ is not a function of applied field ξ. In the frequency domain, the classical FDT states that

$$S_{\mathbb{C}} = \frac{2k_BT}{\pi\omega}\mathrm{Im}\chi_{\mathbb{C}}(\omega) \tag{2.16}$$

where $S_{\mathbb{C}}$ is the two-sided power spectrum (frequency ranges from negative to positive) for the observable $\mathbb{C}$. It has been proven that the FDT can be extended to explain Johnson noise (*57, 58*), which links the electrical thermal noise to the electrical conductivity (*59*). Congruently, in the magnetic system, the Hamiltonian can be written as

$$\mathcal{H}(B) = \mathcal{H}(0) - \int \vec{M}\cdot\vec{B}\,dV = \mathcal{H}(0) - \int \mu_0\vec{M}\cdot\vec{H}\,dV \tag{2.17}$$

For a macroscopic magnetization $\vec{M}$ with the sample volume V, we have the FDT for the magnetic system as

$$S_M(\omega,T) = \frac{2k_BT}{\mu_0\pi\omega V}\mathrm{Im}\chi_M(\omega) \tag{2.18}$$

where χ_M is the conventional magnetic susceptibility defined as

$$\chi_M = M/H \tag{2.19}$$

It has been reported in many spin systems that FDT holds in thermal equilibrium (*60, 61*). However, for the canonical spin ice materials, such a relation has never been examined and whether FDT holds or not is crucial to understand the underlying origin of thermal noise. For example, the consistency between magnetic Johnson noise and the monopole generation-recombination noise can indicate that the major thermodynamic process for magnetic monopole is indeed the GR process. Otherwise, magnetic Johnson noise can be distinct from the GR noise and thus each is dominant in a different frequency regime. It has been demonstrated that spin ice materials will fall out of equilibrium under experimental timescales upon lowering the temperature (*3, 20*). On one hand, some spin

glasses have been reported to obey FDT even in the glassy state (*60*). On the other hand, one theory has predicted that spin ice materials will violate the FDT relation (*62*). Therefore, the detection of such a violation is extremely important for understanding the monopole dynamics in the out-of-equilibrium state.

Chapter 3 Spin Current/Noise Spectroscopy

Magnetometry, which measures the magnetization as a function of applied field and temperature, has been one of the most important techniques for characterizing magnetic materials for decades. In this thesis, we have developed spin current spectroscopy (SCS), which is an extension of conventional magnetometry with high-speed data acquisition for measuring magnetic field with micro-second precision. Hence, SCS is designed to detect the monopole current in spin ice, corresponding to the rate of change of the magnetization. On the other hand, spin noise spectroscopy (SNS) is a new type of magnetic spectroscopy that focuses on detecting the magnetization fluctuation noise. Traditionally, noise has been considered an obstacle in experimental results. However, in 1928, it was demonstrated brilliantly that the resistance of a circuit could be measured directly through Johnson noise, which represents the voltage fluctuation across a resistor at thermal equilibrium (*57*). Thus, by statistically analyzing fluctuations, valuable information could be obtained without applying any external perturbation. This makes SNS a unique tool to characterize magnetic materials, garnering huge interests in fingerprinting magnetic materials, monopole fluids (*39, 46*), and spin liquids (*63, 64*).

Typically, magnetic fluctuations are detected by means of Faraday-rotation (*65, 66*) or by directly measuring the flux threading a coil connected to a superconducting quantum interference device (SQUID) (*39*). In Oxford, I built the SCS/SNS apparatus based on the latter method. To date, SQUIDs are the most sensitive detectors of magnetic flux at the level of micro flux quantum per root Hertz ($\mu\varphi_0/\sqrt{\text{Hz}}$). In this chapter, I first

introduce the basics of the SQUID-based spectrometer. Then, I provide a comprehensive description of ANDROMEDA, the home-built low-temperature spin current/noise spectroscope in Oxford. In describing the construction of ANDROMEDA, I would like to acknowledge the assistance of Hiroto Takahashi. The full description of apparatus is followed by a description of different experimental functionality, including the time/frequency domain measurements, as well as noise spectroscopy.

3.1 SQUID-based Spectroscopy

The history of SQUID magnetometry dates back to the 1960s when it was first invented (*67*). It remains the most sensitive magnetic field sensor available, with fT magnetic field precision and a noise level of $\mathrm{fT}/\sqrt{\mathrm{Hz}}$. Depending on the number of Josephson junctions, SQUIDs are classified as DC SQUIDs (2 junctions) or rf SQUIDs (1 junction). In general, DC SQUIDs offer better noise performance, which is why the home-built SQUID spectrometer is based on a DC SQUID. The basic working principles discussed here are specific to DC SQUIDs.

In principle, a SQUID operates optimally at a working point where the flux Φ_{SQ} sensed by the SQUID is linear to the voltage V_{SQ} across it. In practice, a flux-locked loop is normally implemented to lock the flux in a SQUID to be constant by using an additional feedback coil (see Figure 3.1). A current bias is maintained in the SQUID circuit, and the voltage readout is achieved through a flux modulation scheme. In this scheme, a modulated flux Φ_{FLL} is applied to the SQUID such that the working point changes periodically, resulting in an alternating voltage. The voltage modulation is then captured by the lock-in detection and processed through an integrator for the final readout (*68*).

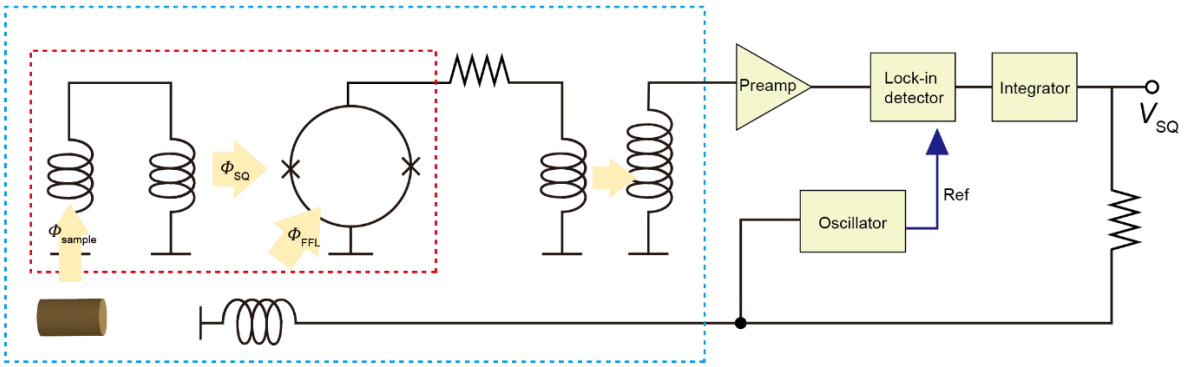

Figure 3.1 Schematic illustration of the circuit diagram of a SQUID magnetometry. The red dashed box marks the measurement circuit, which composes of an input coil and SQUID. The blue dashed box marks the region where the circuit is at cryogenic temperature.

A SQUID magnetometer is realized with another input coil to the SQUID. As shown in the red dashed box in Figure 3.1, the input coil transfers the flux Φ_{sample} generated by the target sample to the flux Φ_{SQ} detected by the SQUID. The calibration of the transfer function from Φ_{sample} to Φ_{SQ}, and eventually to V_{SQ}, is critical for the accuracy of all SQUID-based techniques. The detailed discussion of our SQUID spectrometer's calibration is provided in Appendix A.

SQUID-based spin noise spectroscopy had been employed to study the tiny magnetic field fluctuations from various materials (*60, 69-71*). One of the key advantages of SQUID spectroscopy is its frequency response and bandwidth, as its magnetic field sensitivity persists in low frequency down to DC (*66*). One remarkable success for SQUID-based flux noise spectroscopy was its contribution to the identification of the frequency characteristics of the magnetic noise in spin glass materials. The detection of 1/f noise in spin glass has provided critical insights into the development of spin glass

theory (*72*). Furthermore, SQUID-based noise spectroscopy has been used to unveil the microscopic dynamics of magnetic monopoles, marking a breakthrough in the study of spin ice. Based on these developments, ANDROMEDA is further designed to detect the magnetic noise while the magnetic field is driven externally.

3.2 ANDROMEDA: Monopole Current/Noise Spectrometer

The main experiments reported in this thesis were carried out in ANDROMEDA, which is a SQUID-based spectrometer housed in a custom-built 1 Kelvin (1K) cryostat or the cryo-free 3He refrigerator. Figure 3.2 shows a photograph of the ANDROMEDA spin current/noise spectroscopy on board a 1K cryostat.

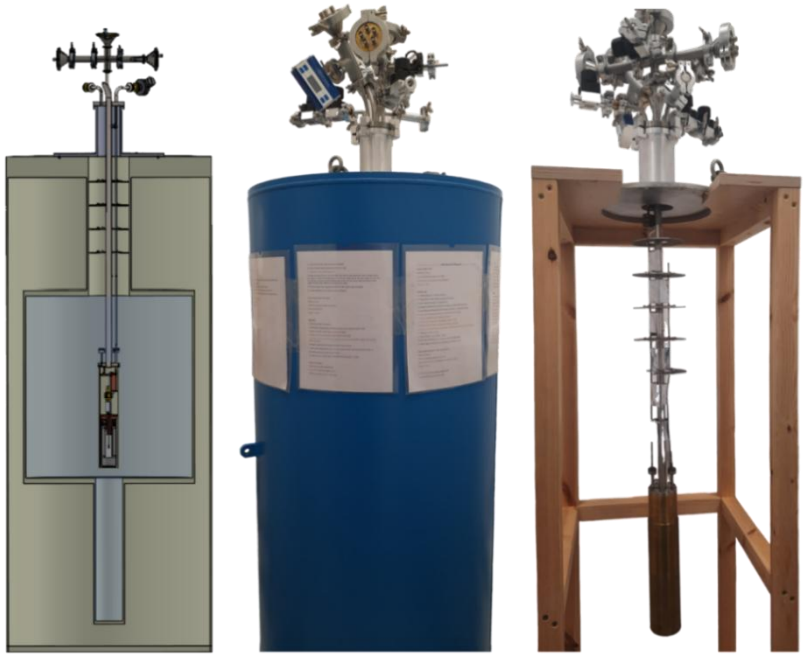

Figure 3.2 Photograph of ANDROMEDA. The left panel shows the cross-section of experimental apparatus in the dewar. The middle is the photograph of the insert during the ongoing experiment. The right panel shows the overall insert on the wooden support.

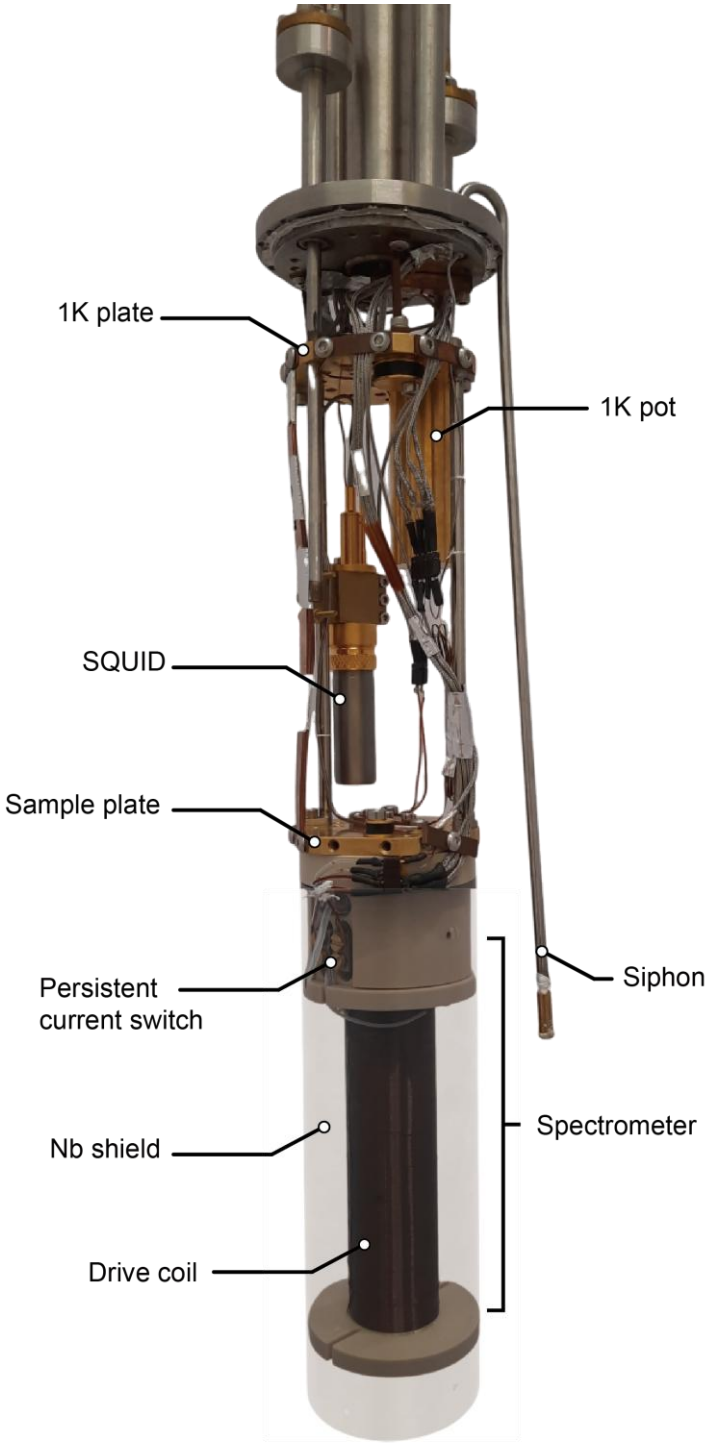

Figure 3.3 Photograph of the cryogenic insert from the vacuum can top (4K) to the bottom spectrometer. The components are labeled accordingly.

3.2.1 Cryostat

The cryostat serves as the structural framework of the SCS/SNS apparatus, which contains the exterior dewar and the interior cryogenic insert.

Dewar

During the experiment, the dewar provides the liquid helium (LHe) bath necessary for the cryogenic insert. It is a double-wall container with the first stage thermal isolation between the exterior and the interior of the dewar. Between the walls is a vacuum jacket that separates the inner container, which reduces the boiling rate of the liquid helium and thereby extends the duration of experiments. In practice, the vacuum jacket is evacuated to ~ 10^{-3} mbar at room temperature and further pumped to lower vacuum via activated charcoal at cryogenic temperatures. To minimize the thermal load from the 300K environment, the dewar neck is made of G-10 fiberglass, known for its low thermal conductivity. Moreover, 4 radiation shields are installed on the cryogenic insert to block the hollow neck and prevent direct heating from radiation. With this optimized heat load, the dewar and the insert achieve a boiling rate of 8 liters per day, allowing the experiment to run continuously for weeks without needing LHe refills (total volume of the dewar is about 120 L).

4He Refrigerator

The cryogenic insert is soaked directly in the LHe bath, ensuring a stable thermal link to the 4K plate. All coaxial cryogenic cables and the SQUID cable are thermally anchored to the 4K plate before reaching the 1K plate and the sample. Through evaporative cooling of the 4He, ANDROMEDA can further reach lower temperature at

1.7 K, which is monitored by the Rox thermometer on the 1K plate. The cooling power of evaporating liquid helium is determined by $\dot{Q} = \dot{n}\dot{L}$, where $\dot{n}$ is the evaporation rate, controlled by the pumping speed, and L is the latent heat of liquid helium-4. The evaporating rate is proportional to the vapor pressure, and hence $\dot{Q} \propto P_{vap} \propto e^{-\frac{1}{T}}$. In ANDROMEDA, a 4He pot with a volume of 15.5 cm^3 is used, with a fraction of liquid helium flowing through the siphon to the pot during experiments. To increase the impedance for the liquid helium flow and thereby decrease the heat load from the continuous liquid helium compensation, the 0.25mm ID CuNi siphon is filled with 0.23mm OD stainless steel wire. The thermal link between the 1K pot and the sample is first provided by 10 layers of copper sheets to the sample plate, followed by a sapphire wire linking to the sample at the PEEK holder. The Cernox thermometer and the metal-film resistive heater are placed firmly onto the thermal link to the sample to have sufficient accuracy in temperature reading. The overall relative position and the wiring diagram of heaters and thermometers are shown in Figure 3.4.

Vibration Isolation

The whole 1K refrigerator is mounted on the isolated ultra-low vibration keel-slab in an acoustically isolated laboratory. The keel-slab is a 30-ton concrete slab that floats the entire apparatus, including the dewar and the cryostat. To avoid the mechanical noise produced from the 1K pot pump, all the pumps are located in the control room which is separated from the experimental room.

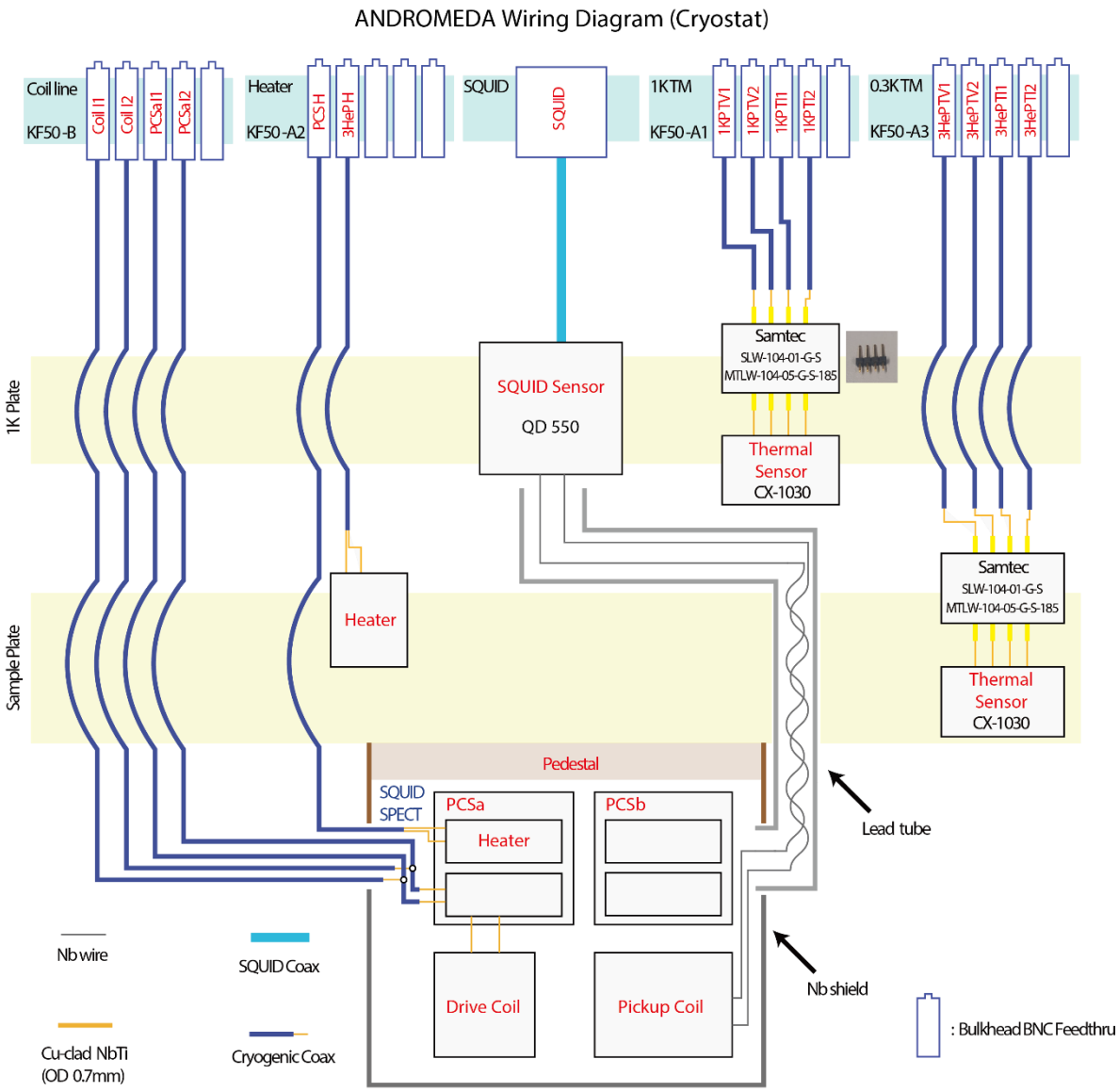

Figure 3.4 The practical wiring diagram of ANDROMEDA. All the coaxial wires are shielded with the stainless-steel braiding until entering the Nb shield of the spectrometer. The pickup coil is made as a twisted pair inside the lead tube to the SQUID connection.

3.2.2 Spectrometer

The spectrometer is the most unique part of the apparatus. Figure 3.5, Figure 3.6 and Figure 3.7 shows the photo of the spectrometer, schematic illustration and its dimension.

The spectrometer assembly consists of a superconductive pickup coil wound directly on the sample holder and an enclosing superconducting excitation coil. The cylindrical sample holder is designed with a concentric hole of 1.6 mm diameter and length 5 mm, in order to encapsulate the rod-shaped sample. During the experiment, the rod-shaped sample is held in the hole covered by the GE varnish. The pickup coil which is made from a single wire consists of two in-series counter-wound NbTi coils with 10 turns each and is fixed onto the PEEK holder with Stycast 1266. The excitation coil is wound with NbTi for 537 turns and 90 mm in length. The mid-point of pickup coil is at the center of the excitation coil. The overall spectrometer assembly is mounted below the refrigerator and is shielded by a Nb shield which has an inner diameter of 47.9 mm and 2 mm in thickness. The pickup coil, excitation coil, and Nb shield are concentrically aligned. The SQUID is mounted next to 1K pot to maintain the low SQUID temperature while varying the sample temperature during the experiments. The SQUID is shielded separately with another Nb shield provided by the manufacturer (Quantum Design) and the input inductance L_i is reported to be 1.82 μH. To deliver the detected flux signal, the pickup coil enters the SQUID externally and is shielded inside the superconducting Pb alloy tube with the twisted pair to reduce the overall inductance.

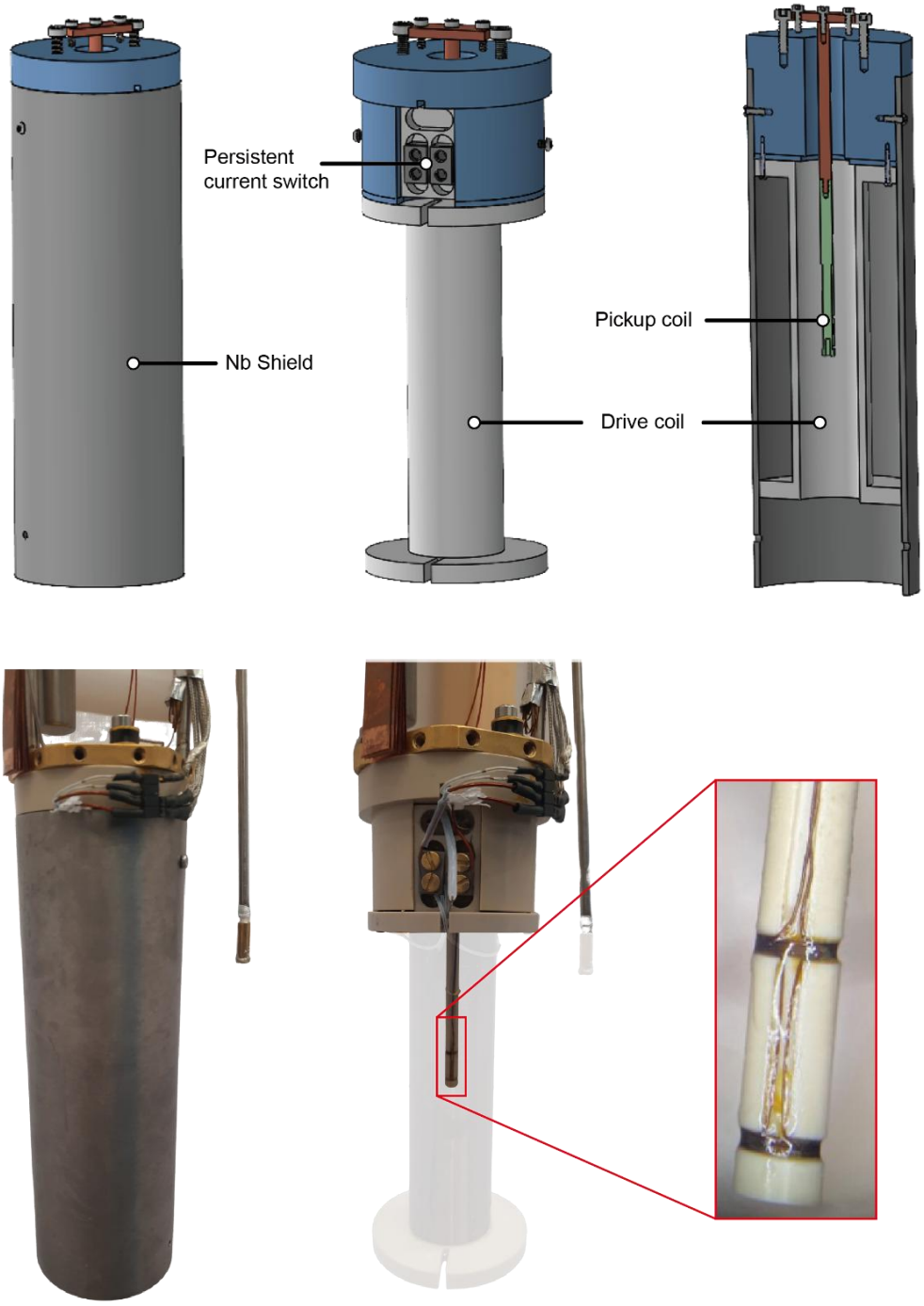

Figure 3.5 The design of the SQUID spectrometer. The components are labeled accordingly (upper panel). The photograph of the SQUID spectrometer (bottom panel). The right panel shows the zoom-in image of the counter-wound pickup coil (for the work of Chapter 4).

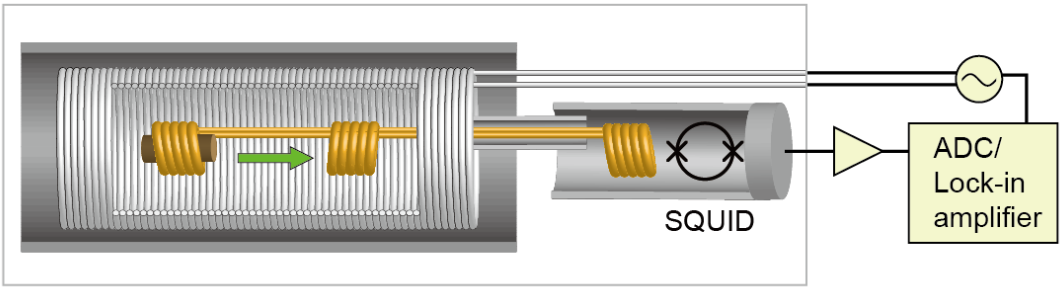

Figure 3.6 Schematic illustration of the SQUID spectrometer and the simplified circuit diagram. The voltage output from SQUID is fed into a preamp, which is followed by the ADC/lock-in amplifier.

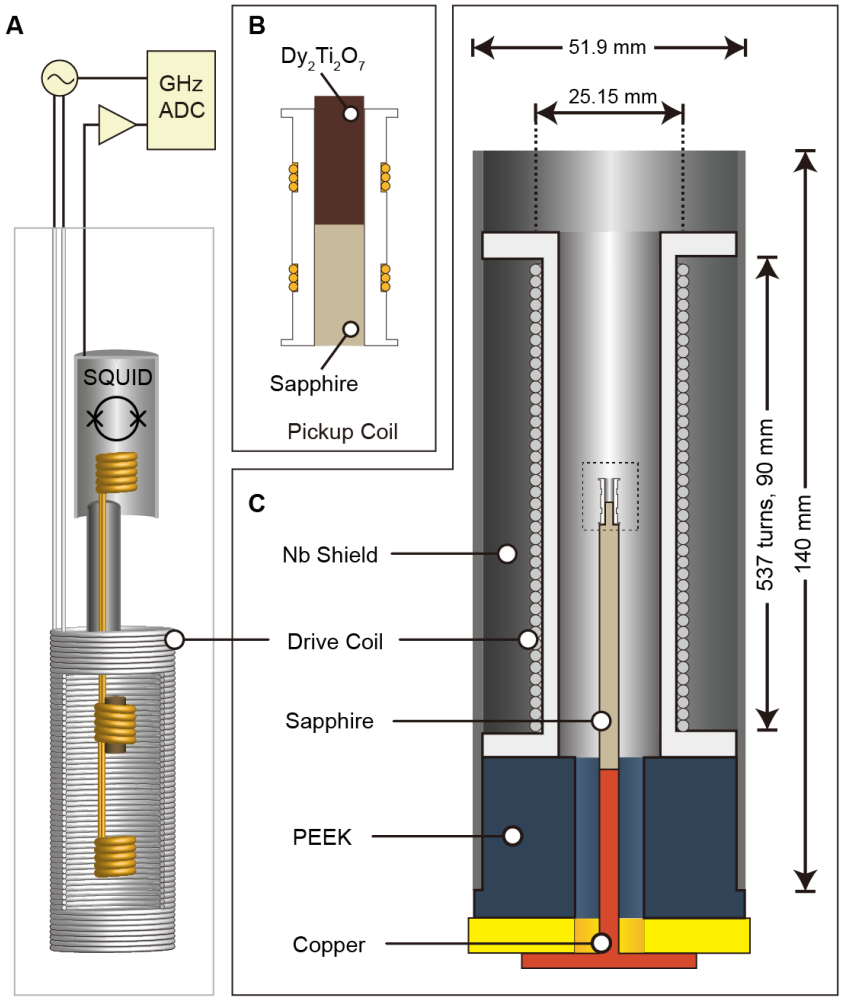

Figure 3.7 (A) Schematic illustration of the modified SQUID spectrometer (for the work if Chapter 6). (B) Zoom-in illustration of pickup coil. (C) The dimension of the spectrometer.

The design idea of the spectrometer is to maximize the signal-to-noise ratio when the external magnetic field is applied to drive the monopole current. The whole spectrometer assembly including the superconductive solenoid generating magnetic field $B(t)$ achieves an overall noise floor $\delta\Phi \lesssim 10^{-5}\ \phi_0/\sqrt{\text{Hz}}$ (see Appendix A.2). The design of superconductive and opposite chirality pickup coil pairs at the center of the drive solenoid achieves almost no net flux to the SQUID when the magnetic field $B(t)$ is applied (see Appendix A.3). Thus, when a sample is introduced to one of the pickup coils, the flux produced from the sample dominates over the flux from the external field.

3.2.3 SQUID & Electronics

SQUID (QD 550)

QD Model 550 manufactured by Quantum Design is the SQUID we adapted to the SCS/SNS. The overall circuitry of the SQUID can be simplified as Figure 3.1 where the input inductance is 1.82 μH and the mutual coupling between Φ_{SQ} and SQUID is 0.21 $\mu A/\phi_0$. QD 550 is a 1-stage SQUID which has a bandwidth of 5 kHz. The flux noise floor of the SQUID is about $5 \times 10^{-5}\ \phi_0/\sqrt{\text{Hz}}$. The sensitivity range has 4 ranges, yielding a full scale from $5\ \phi_0$ to $500\ \phi_0$.

GHz ADC Datalogger (Moku Pro)

A datalogger equipped with GHz analog-to-digital converter (ADC) is used for the time-domain measurements. The internal sampling rate of Moku runs at 5 GSa/s for single channel acquisition and 1.25 GSa/s for four channels. Moku uses a 10-bit ADC as the analog input. By using a combination of limited data acquisition sampling rate (10 MHz for single channel) and oversampling, the effective bit range can be up to 8 bits to

18-bit range with the input voltage range from 400 mV to 40V. Furthermore, with the FPGA-based technique and the blended ADC, Moku can achieve a noise floor below 100 nV/$\sqrt{\text{Hz}}$ for the frequencies in our interest.

Lock-in amplifier (Stanford Research 830)

The frequency domain measurements are performed with Stanford Research 830 (SR830). SR830 is a digital signal processing lock-in amplifier where the voltage signal is first amplified by the internal gain (set by sensitivity) then fed into the digital processor. The digital processor serves as the phase sensitive detector by mixing the input signal with the reference signal. The real component and the imaginary component at the reference frequency are then filtered out by the low pass filter. During the experiments, the sensitivity, dynamic range, input coupling, time constant, and the type of reference (Sine/TTL) are chosen for specific needs.

Arbitrary waveform generator (Keysight 33500)

To generate the magnetic field in the drive coil, an arbitrary waveform generator (Keysight 33500B) is used as a voltage source. The 33500B can output arbitrary waveform designed by the user with low jitter as 100 ps (the square wave edge distortion) and a sampling rate of 1 GSa/s. The waveform generator has a second channel which outputs the TTL waveform with synchronous frequency as the main output channel. In practice, this channel is used as a system clock to detect any phase difference between signals, especially for the lock-in amplifier.

Differentiator amplifier

Since the monopole current $J \propto \mathrm{d}M/\mathrm{d}t$, it is crucial to detect the time derivative of a signal directly instead of doing numerical derivatives in post data analysis, which

potentially induces artificial errors. A typical differentiator circuit is shown in Figure 3.8, which comprises a capacitor followed by a resistor to ground. The bandwidth of a differentiator circuit is $BW = 1/2\pi RC$, and the effective gain is $g = RC$. A typical choice of resistor R is 50 kΩ and capacitor C is 1 nF. This combination yields a bandwidth of 3 kHz and $g = 5 \times 10^{-5}$. The effective gain suppresses the signal-to-noise and therefore a differentiator circuit is normally followed by an additional voltage amplifier. In my experiment, the voltage output differentiator circuit is typically fed into SR560 voltage amplifier with a gain of over 1000.

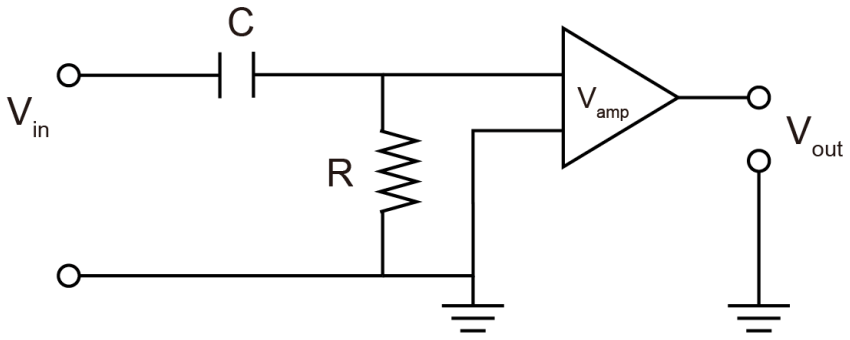

Figure 3.8 Circuit diagram of a differentiator circuit. The relaxation between V_{in} and V_{out} is $V_{out} = RC(\frac{dV_{in}}{dt})$.

3.3 Types of Measurements

With the powerful functionality of measuring the flux response and the flux noise simultaneously, the parameter space for the SCS/SNS expands significantly in terms of magnetic field strength, types of applied field, and the frequency of the alternating field. In general, the types of measurements can be classified into three categories for the SCS/SNS technique, which are the time-domain, frequency domain measurements and

noise spectroscopy. I will introduce the general data acquisition process and analysis method for these measurements, which have been performed to explore different scientific projects in the later chapter of this thesis.

3.3.1 Time domain measurement

To measure the magnetization response (monopole current) under the magnetic field excitation of a certain waveform, the SQUID voltage output is recorded by the 16 bit-ADC (Moku) at the sample rate of 1MSa/s and for typically over 1000 transients of excitation at each measured temperature. Simultaneously, the ADC is set to record the voltage across the resistor in series of the input coil to measure the input magnetic field in the time domain (see Figure 3.8). Experimentally, SQUID is normally set at the highest sensitivity (range 5). Notably, the SQUID provided by the manufacturer has a linear frequency response of 5 kHz, which causes an adjusting time of roughly 200 μs. Therefore, all the time series analysis will exclude the first 200 μs to avoid the influence from the SQUID electronics. Based on different needs for the experiments, the custom designed excitation magnetic field is applied. For example, to study the transient of monopole current, the excitation field is designed to be a sequence of square waves in the two directions. On the other hand, a triangular excitation field is beneficial for the constant monopole current study while the sinusoidal field provides essential information for complex conductivity.

In general, to increase the signal-to-noise ratio (SNR), the flux response in the time-domain $\Phi(t)$ is averaged for all the transients or sections. For example, for the flux response under a sinusoidal magnetic field excitation $B_0\sin(10\pi t)$, we can define 2

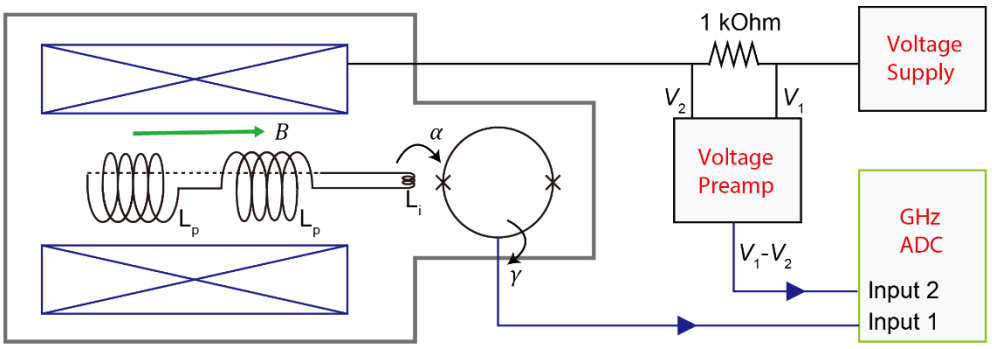

Figure 3.9 Circuit diagram of the time-domain flux transient measurement. Channel 1 of the ADC records the SQUID output while channel 2 records the voltage difference of the resistor in series of the drive coil.

periods as one section. In a time domain flux $\Phi(t)$ with a total length of 1 minute, $\Phi(t)$ can be divided into 150 sections. Mathematically, the corresponding flux $\Phi(t)$ is cut into k sections, and t = 0 is defined as the time when B field is turned on (B=0) at each section.

$$\Phi(t_j) = \begin{Bmatrix} \Phi_1(t_j) \\ \Phi_2(t_j) \\ \cdots \\ \Phi_k(t_j) \end{Bmatrix} \tag{3.1}$$

Therefore, the flux response $\Phi(t)$ is later averaged by k sections as

$$\langle \Phi(t) \rangle = \frac{1}{k} \sum_{i=1}^{k} \Phi_i(t_j) \tag{3.2}$$

Experimentally, it is essential to synchronize all the sections so that the phase maintains the same value for each section, which is achieved by the choice of the frequency of the magnetic field and the sampling rate of the ADC. The frequency of the magnetic field must be a factor of the sampling frequency. Notably, other unwanted noise such as 50 Hz electronic noise is not coherent throughout the whole recorded time-domain. Therefore, average flux response is robust against electronic noise with this technique. The residual

phase noise is from the internal clock of the ADC and the phase noise from the waveform generator, which in combination leaves an overall phase shift 0.0021 rad after 1800 periods of a 10 Hz sinusoidal wave (see Figure 3.10). In practice, it is also important to compensate any low frequency flux/voltage drift in the experiment. To eliminate any flux drift, each section can first subtract the section average before doing the overall averaging process.

$$\langle \Phi(t) \rangle = \frac{1}{k}\sum_{i=1}^{k}\left(\Phi_i(t_j) - \frac{1}{T}\sum_{j=1}^{T}\Phi_i(t_j)\right) \tag{3.3}$$

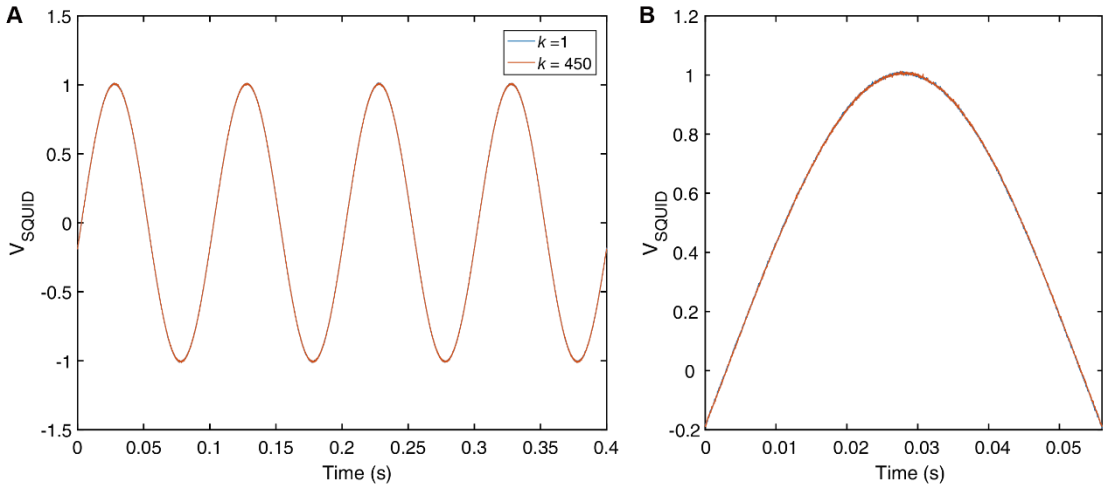

Figure 3.10 Demonstration of the synchronized sections for the time domain measurement. (A) Comparison of section k =1 and section k =450 under sinusoidal magnetic field (f = 10 Hz). (B) Zoom-in image of (A).

3.3.2 Frequency domain measurement

Frequency domain measurements were performed by using a lock-in amplifier, which is essential to the magnetic susceptibility and monopole complex conductivity measurements. The working principle of the frequency domain measurement is that the lock-in amplifier picks up the in-phase and out-of-phase components from the SQUID voltage output comparing to the reference signal. That is,

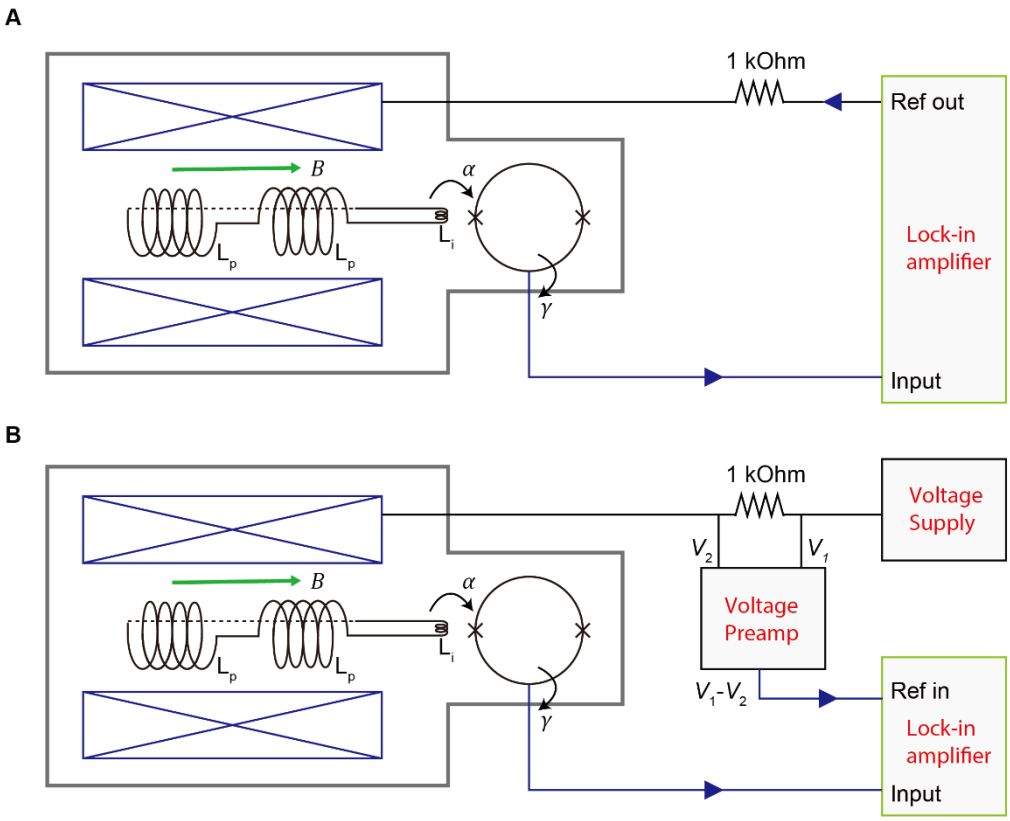

Figure 3.11 (A) Circuit diagram of the frequency-domain conductivity measurement using internal reference from SR830. (B) Circuit diagram of the frequency-domain conductivity measurement with external reference source from the voltage drop of the resistor in series of the primary coil.

$$V(t) = V_X \sin(2\pi f t) + V_Y \cos(2\pi f t) \tag{3.4}$$

Therefore, we can derive the in-phase flux and the out-of-phase flux as

$$\Phi(t) = \Phi_X \sin(2\pi f t) + \Phi_Y \cos(2\pi f t) \tag{3.5}$$

Experimentally, the lock-in circuitry can be categorized based on the usage of an internal or external reference source (Figure 3.11). Internal reference is preferable for the low frequency (f < 10 Hz) measurement since the lock-in amplifier has more phase noise when detecting the external sinusoidal reference at low frequency (0.005 deg for external, <0.0001 degree for internal at 1kHz). Also, the TTL waveform (binary signal) is

suggested for external reference at low frequency. On the other hand, the lock-in circuitry with the external reference is shown as Figure 3.11B. The waveform generator produces an AC sinusoidal drive to the primary coil in the typical frequency range of 10 Hz to 10000 Hz, and the reference of the lock-in amplifier is set by measuring the actual current using the voltage drop across the 1 kΩ resistor in series. This is to compensate the phase change due to the LR circuit of the primary coil especially at high frequency. For both types of circuitry using internal or external reference, the zero phase is set by performing a calibration experiment without a sample for the frequency range from 10 Hz to 5 kHz (see Appendix A.4). Typically, the sensitivity of SQUID is set at range 500 for better SNR. The sensitivity and the time constant of the lock-in measurement are chosen specifically based on different frequency ranges.

3.3.3 Noise spectroscopy

One of the most powerful functions of SQUID spectrometers is noise spectroscopy. As mentioned in Chapter 1, noise spectroscopy is the key experimental tool that unravels the fine monopole dynamics which are hidden in other experimental techniques. With the capability of applying magnetic fields, studying the monopole noise under different excitations becomes possible. Conventionally, measurement of the noise spectrum can be achieved by using a spectrum analyzer, lock-in technique, or datalogging (ADC). A spectrum analyzer is the most time-efficient tool to measure power noise spectrum which records the power when scanning through different frequency bins with narrow band-pass filters. However, spectrum analyzers normally have limited frequency bins and thus the lowest detectable frequency is also constrained. Furthermore, spectrum analyzers cannot perform noise spectroscopy under dynamical fields as the alternating

field at certain frequencies disturbs the overall spectrum by lifting up the floor of the power spectrum. On the other hand, the lock-in technique calculates the power noise from the fluctuation of the in-phase and out-of-phase channel and thus is capable of measuring the noise under the AC field. Yet, the tradeoff is the long acquisition time and that it can only probe single frequency at a time. Overall, probing the noise spectrum from the time series recorded by the datalogger is a balanced method meaning that the power spectrum converges quickly with the acquisition while preserving the capability of a wide frequency scan. Experimentally, the data acquisition and analysis procedure of calculating the power noise spectrum from the recorded time series flux can be categorized based on whether the external field is dynamical.

Zero field/static field noise spectroscopy

The noise spectroscopy performed under zero field is calculated from the recorded $\Phi(t)$ whose average $\langle\Phi(t)\rangle = 0$. For the static field, the SQUID can be reset and offset to 0 and thus the noise spectrum can be calculated in the same manner. More specifically, the one-sided power spectral density (PSD) $S_\Phi(\omega_n)$ is calculated from the time series data $\Phi(t_j)$ first by dividing the flux data into *k* sections (Eqn. 3.1). Each section contains N_t data points with a time interval Δt set by the sampling rate. The PSD at each section $S_\Phi^i(\omega_n)$ can be obtained from

$$S_\Phi^i(\omega_n) = \frac{1}{\pi N_t}\left|\sum_{j=1}^{N_t} e^{-i\omega_n t_j}\Phi_i(t_j)\right|^2 \tag{3.6}$$

where $\omega_n = \frac{2\pi n}{(N_t-1)\Delta t}\left(n = 0, 1, \ldots \frac{N_t}{2}\right)$.

Similarly, to enhance the SNR, the averaged PSD is given by

$$\langle S_\Phi(\omega_n)\rangle = \frac{1}{k}\sum_{i=1}^{k} S_\Phi^i(\omega_n) \tag{3.7}$$

It is apparent that for a time series with a fixed length, the data point number N_t is inversely proportional to the section number *k*. The former determines the lowest frequency and the latter determines the error bar for each PSD data. Thus, practically the experiment is performed continuously for a long time to have the optimal frequency range with a converging error bar. Another important property of the noise is the variance of the time series data, which can be calculated by

$$\sigma_{\Phi}^2 = \frac{1}{N_t}\sum_{j=1}^{N_t} \Phi^2(t_j) \tag{3.8}$$

Dynamic field noise spectroscopy

The data acquisition procedure of the noise spectroscopy under dynamical field is different from zero/static field because the time duration of each section is constrained by the frequency of the alternating field. To examine the noise, we can define the flux deviation of each section from the averaged flux response by

$$\delta\Phi_i(t_j) = \Phi_i(t_j) - \langle\Phi(t)\rangle \tag{3.9}$$

Note that $\langle\Phi(t)\rangle$ is no longer zero in this case. The variance at each time of a section can thus be obtained by

$$\sigma^2(t_j) = \frac{1}{k}\sum_{i=1}^{k} \delta\Phi_i^2(t_j) \tag{3.10}$$

In the dynamic field study, it is important to examine whether the variance exhibits time-dependence or field-dependence, which requires detailed scrutiny on the smaller time cut. Therefore, it is useful to define variance in a smaller time section such that

$$\sigma_{sec}^2 = \frac{1}{N}\sum_{t_1}^{t_2} \sigma^2(t_j) \tag{3.11}$$

where t_1 and t_2 represent the starting point and the end point of a certain section. And $N = \frac{t_2 - t_1}{\Delta t}$.

In summary, in chapter 3, I have introduced in detail the design of the home-built SQUID spectrometer. The data acquisition and the analysis procedure for time-domain, frequency-domain measurements and the noise spectroscopy has also been introduced. In the later chapters of this thesis, these techniques are exploited for the direct observation of dichotomous dynamics of the monopole fluid, the method of measurement of monopole charge, and the discovery the dynamical heterogeneity of the supercooled monopole fluid.

Chapter 4 Dichotomous Dynamics of Magnetic Monopole Fluids

Part of this chapter appear as
Hsu et. al., Proc. Natl. Acad. Sci. U.S.A. ***121****, e2320384121 (2024).*

In Chapter 4, I discuss the first major work performed on ANDROMEDA. Experimental investigations using the monopole current spectroscopy reveal the dichotomous dynamics of monopole current under DC and AC magnetic field and in the simultaneous measured noise spectroscopy (*56*).

4.1 Motivation and Experimental Design

A recent study of emergent magnetic monopoles in spin ice has discovered that monopole motion is restricted to dynamical fractal trajectories (*27*) thus explaining the anomalous noise color of magnetic monopole noise (*39, 46*). The fundamental origin of such fractal transport is from the existence of two distinct spin-flipping rates (*49*), and hence a dichotomous monopole hopping rate, even for a pristine crystal. However, neither the presence of another spin flipping process nor the dynamical fractal pattern of magnetic monopoles has been experimentally observed, and thus the precise transport theory for magnetic monopoles in spin ice remains to be experimentally confirmed.

To further examine the theory, Monte Carlo simulation applying the novel concepts have been carried out (Chapter 2.2). The major consequence is the presence of the termini where the monopole cannot move in the preferred direction under field. Due to the termini, theory predicts a fast decaying reconfiguration current in the monopole

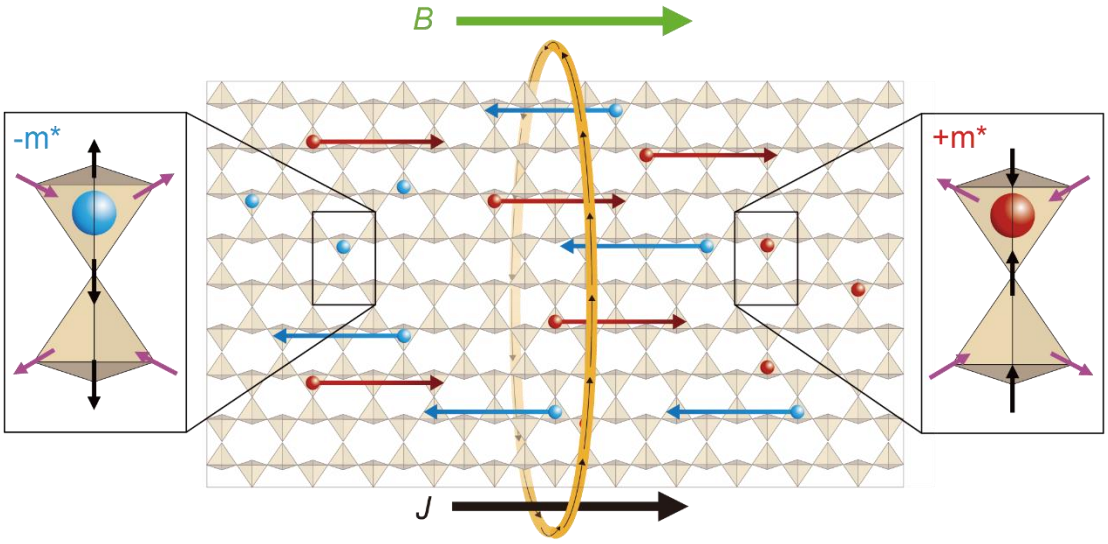

Figure 4.1 Conceptual representation of magnetic field driven monopole current $J(t)$ passing through a superconducting loop (yellow). Positive charged monopoles (red) are driven to the right by an applied field B, and negatively charged (blue) to the left. These rapid monopole currents are occasionally terminated when the spin-flip rate is suppressed by specific local spin conformations, magnified within the smaller panels at left and right.

current transient and the characteristic frequency dependence of the dissipative loss angle of the monopole complex conductivity Therefore, experimental observation of the phenomenon from the termini becomes pivotal. ANDROMEDA, the home-built monopole current/noise spectrometer, is thus a perfect platform to explore the dynamics of the field-driven monopole currents.

With the technique of simultaneous control of monopole current and time-domain measurement, the field-driven monopole currents threading through the pickup coil can be detected by the SQUID, as shown in Figure 4.1. More specifically, the net monopole current is contributed from the rate $\dot{N}_+$ of positive charge passing through the pickup coil

(red, Figure 4.1) and the rate $\dot{N}_-$ of the oppositely driven negative charge. That is, the net monopole current is given by

$$J(t) = m\dot{N}_+ - (-m)\dot{N}_- = \dot{\Phi}(t)/\mu_0 \quad (4.1)$$

To maintain the flux in the superconductive pickup coil circuit, a spontaneous electrical current (marked by the arrow on the yellow loop in Figure 4.1) will be induced whenever the flux changes by the monopole current.

4.2 Sample Preparation

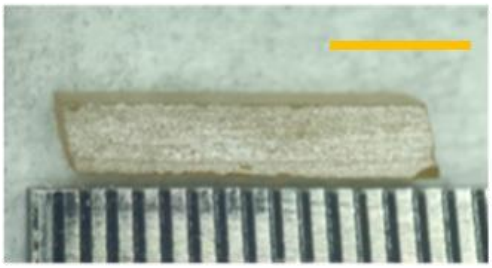

Figure 4.2 Photograph of the $Dy_2Ti_2O_7$ sample. The yellow bar marks the length of 5mm. The long axis of the rod-shaped sample is along the [351] crystal direction.

To study the phenomenon caused by the termini, we choose the canonical spin ice material $Dy_2Ti_2O_7$. The single crystal samples of $Dy_2Ti_2O_7$ were grown using the floating zone method. High purity Dy_2O_3 (99.99%), and TiO_2 (99.99%) were mixed and heated to 1400° C for 40 hours and then again for 12 hours after intermediate grinding. This powder was then packed into a rod which was sintered at 1400° C for 12 hrs. A longer piece of the sintered rod was used as a feed rod and a smaller piece was used as a seed in the floating zone furnace. The growth was carried out in a 0.4 MPa oxygen pressure at 4 mm/hr using a two mirror NEC furnace where the seed and feed rods were counter rotated

at 30 rpm. The $Dy_2Ti_2O_7$ crystal was then cut into a rod-shaped sample with the approximate geometry of 1.3 mm x 1.3 mm x 6.5 mm and with the long axis along the [351] direction (see Figure 4.2). It is important to mention that the sample preparation was done by Sudarshan Sharma and Graeme Luke. I then cut and polished the sample into the rod shape.

4.3 Magnetic Monopole Current Dichotomy

By inserting the DTO sample into one pickup coil of one chirality and applying sequences of magnetic field, we investigated the transient of monopole current in the temperature range from 1.7 K to 4.5 K. This is achieved by using an excitation field designed to be a step-wise magnetic field in both positive and negative directions. Figure 4.3 shows a pedagogical example of such a step-wise magnetic field where the field strength is set at approximately 55 nT. The field excitation remains for 2.5 ms and is followed by a zero field period for 10 ms. The monopole current initiation (MCI) time

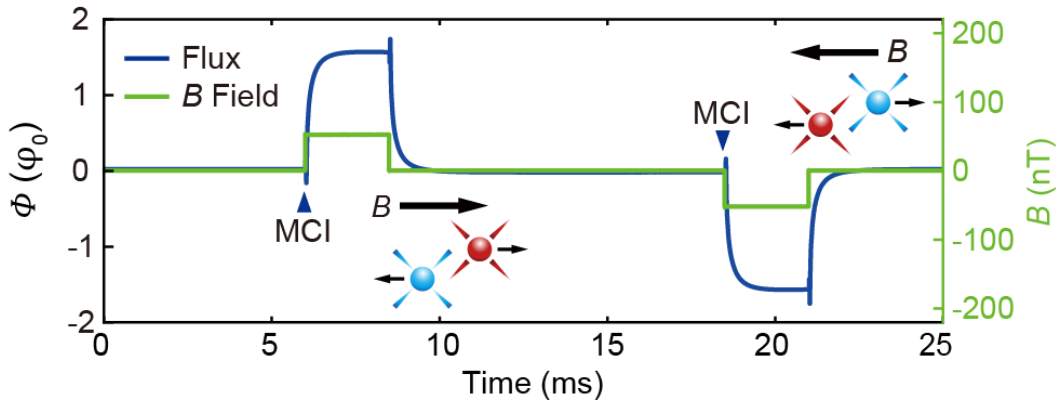

Figure 4.3 Typical example of monopole current control system in operation. The blue trace is the time dependence of flux $\Phi_S(t)$ measured at the SQUID while the green curve shows the magnetic field as a function of time. MCI time marked by the blue sign is set to 0 for each current transient.

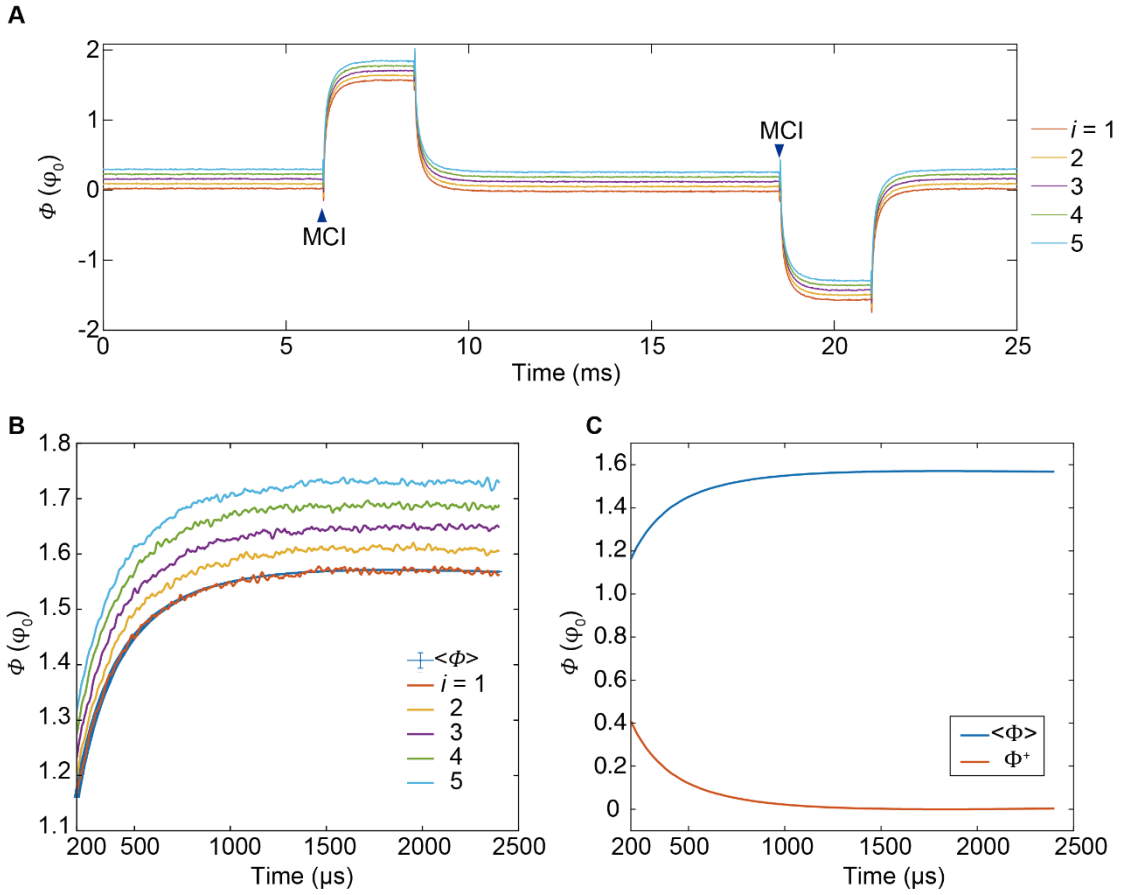

Figure 4.4 Schematic illustration of the averaging process for time domain measurement. (A) Typical example of flux response cut into *k* sections where first five sections are shown and are shift for clarity. (B) The zoom-in for the first 2500 μs after the MCI at 6 ms in (A). The averaged flux response demonstrates significantly improved SNR. (C) Comparison of averaged flux $\langle \Phi(t) \rangle$ and Φ^+, where the $\Phi^+ = \langle \Phi(t = 1.8\ \text{ms}) \rangle - \langle \Phi(t) \rangle$.

when the magnetic field is turned on within 1 μs is marked by the blue arrow. Notably, MCI is set to $t = 0$ for each transient. Typically, the overall duration of measurement is over 2 minutes, with over 1000 transients at each measured temperature. Experimentally, the analog-digital converter (ADC) datalogger records the output voltage from the SQUID at the sample rate of 1MSa/s. Also, as mentioned in Chapter 3.3, the SQUID has a flux feedback equilibration time of about 200 μs, which can be seen around MCI.

Therefore, all the time series analysis in the later section excludes the first 200 μs.

According to Eqn. 3.1 and 3.2, the flux is cut into k sections and thereby averaged for all transients at each temperature. To remove the contribution of the flux offset at zero field, the flux in the positive field direction is subtracted by the offset at t = 1.8 ms. Also, to further compare the flux response with the simple exponential decay, the sign flip of flux is imposed, with

$$\Phi^{+} = -\big(\langle\Phi(t)\rangle - \langle\Phi(t_j = 1.8\ \mathrm{ms})\rangle\big). \tag{4.2}$$

Similarly, in the negative field direction the flux response is calculated as

$$\Phi^{-} = \langle\Phi(t)\rangle - \langle\Phi(t_j = 1.8\ \mathrm{ms})\rangle. \tag{4.3}$$

A typical example of the measured $\log\Phi_S(t)$ after Eqn. 4.2 and 4.3 is shown as Figure 4.5, with a time window from 200 to 1000 μs after MCI at 1.7 K. A clear transition occurs at short times t < 600 μs with a time constant τ_1. At long times t > 600 μs, we observe a conventional exponential decay in $\Phi_S(t)$ (linear line in the $\log\Phi_S(t)$ plot). A linear fit for the long times is plotted as a grey dashed line in Figure 4.5 as a guide to the eye. Since the monopole current $J(t) = (d\Phi/dt)/\mu_0$, the transition at short timescale to a conventional exponential decay for $\Phi_S(t)$ reveals two distinct monopole current regimes. This observation in the real time measurement corroborates the first prediction of the current dichotomy of bSM model as shown in Figure 2.5.

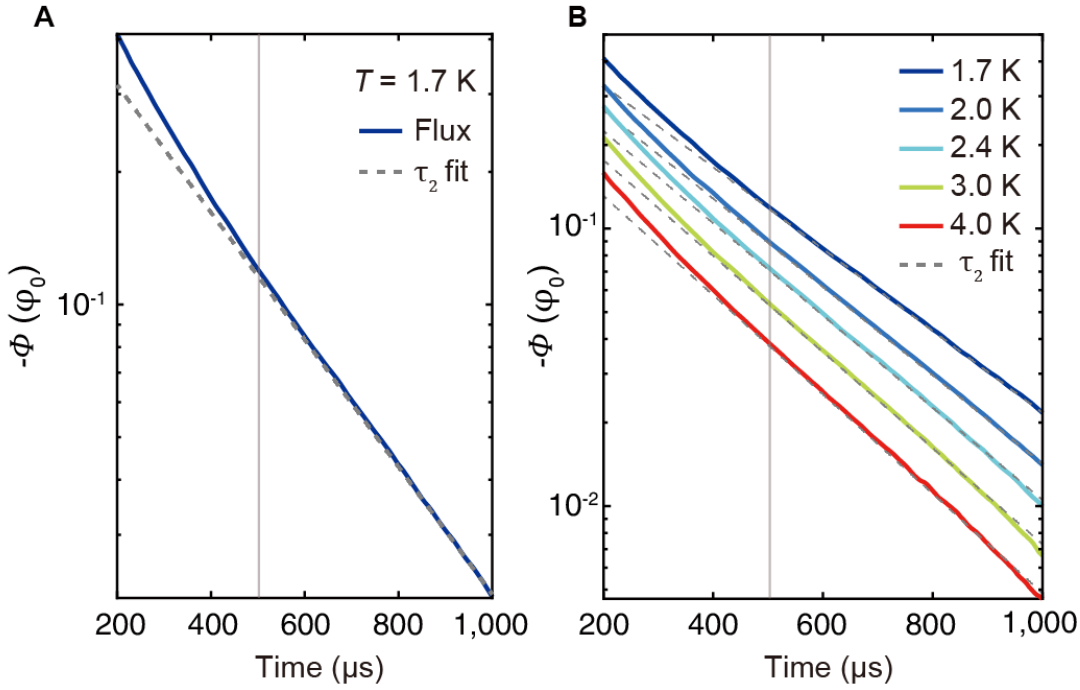

Figure 4.5 (A) Typical example $\log\Phi_S(t)$ from 200 μs after MCI at t = 0. Since the monopole current $J(t) = (d\Phi/dt)/\mu_0$, the deviation of a single timescale exponential decay for $\Phi_S(t)$ reveals two distinct monopole current regimes. (B) Measured $\log\Phi_S(t)$ evolution for T = 1.7, 2.0, 2.4, 3.0, and 4.0 K, and for both positive and negative magnetic field directions. For all transients at long times the time constant $\tau_2(T)$ is measured by a linear fit (grey dashed line). At short times t < 500 μs for all these transients, a transition occurs to a faster time constant $\tau_1(T)$ for monopole current decay (fit in Figure 4.7B).

4.3.1 Separation of Two Timescales

From the direct measurement on how the flux response decays in time (Figure 4.5), two regimes of monopole current are clearly visualized. To further examine the properties of these two currents (reconfiguration current and polarization current), we separate the currents by direct fitting in the semilog plot. Axially, the magnetic field in the positive direction B^+ and in the negative direction B^- are symmetric, and the monopole currents $J^{\pm} \propto \dot{\Phi}_S^{\pm}(t)$ generated by both directions are studied throughout.

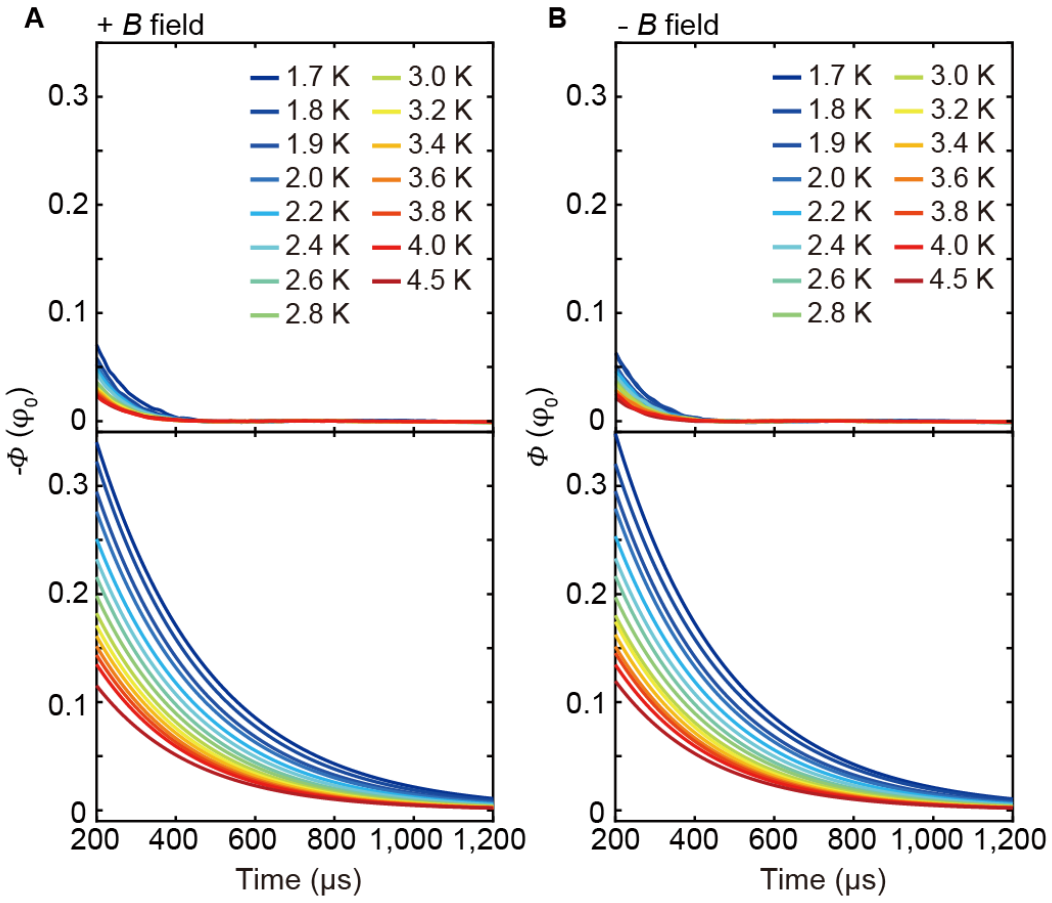

Figure 4.6 (A) Extracted $\Phi_1(t)$ and $\Phi_2(t)$ for fast-decaying current (upper panel) and slow-decaying current (lower panel) in the positive *B*-field direction These fast-decaying currents have ceased for t > 600 μs from MCI. (B) Extracted $\Phi_1(t)$ and $\Phi_2(t)$ in the negative *B*-field direction.

More specifically, the flux responses are decomposed into Φ_1 and Φ_2, such that

$$\Phi^{\pm}(t,T) = \Phi_1^{\pm}(t,T) + \Phi_2^{\pm}(t,T) \tag{4.4}$$

where Φ_1 and Φ_2 represents the contribution from currents with fast and slow time constant, respectively. In the long-time limit, Φ_1 would approach zero and thus we fit the function of

$$\log \Phi_2(t,T) = C(T) - t/\tau_2(T) \tag{4.5}$$

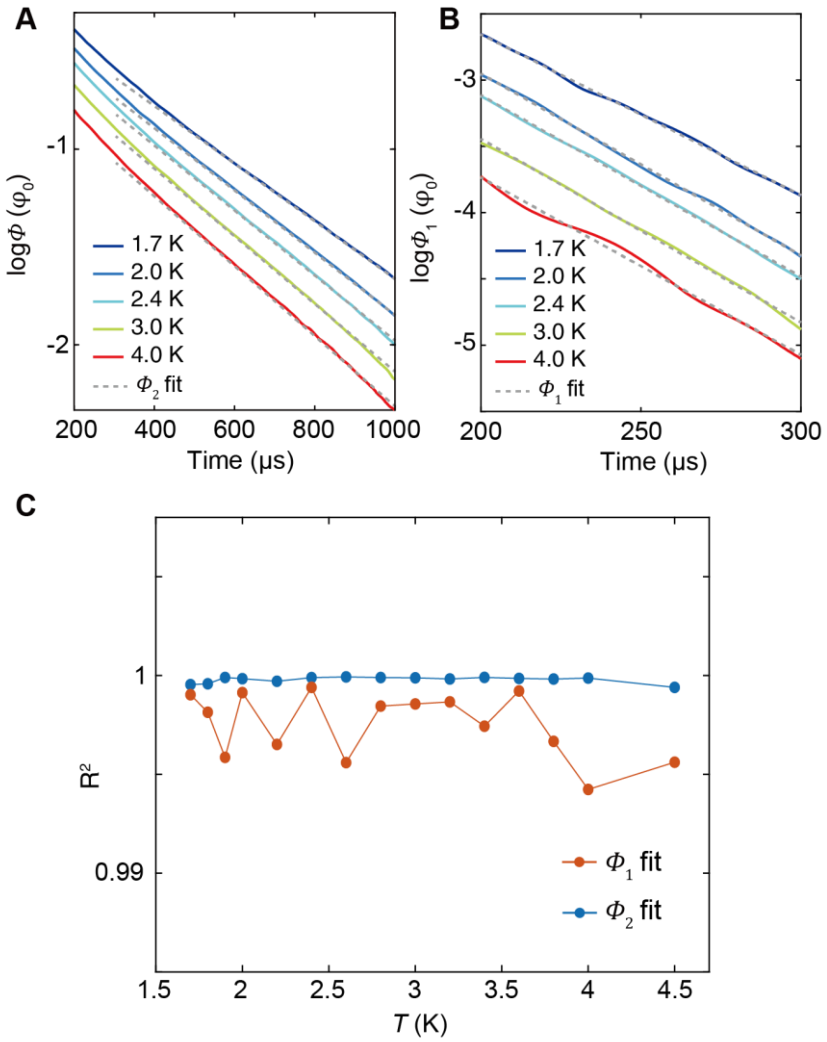

Figure 4.7 (A) Linear fit of $\log \Phi_2(t,T)$ showing in the range to 1000 μs. The fitting curve is extended to 300 μs as a guidance for deviation. (B) Linear fit of $\log \Phi_1(t,T)$ from 200 μs to 300 μs. (C) Exanimation of fitting quality from the R^2 of the linear fit of Φ_1 and Φ_2 for the measured temperature range. Note that fitting the data with only single timescale lead to $R^2 < 0.96$.

between times 600 μs $< t <$ 1200 μs for the long time constant $\tau_2(T)$. The extracted Φ_2 for all temperatures are plotted in the lower panels in Figure 4.6. On the other hand, Φ_1 is derived from the subtraction of Φ_2 from the total flux and by fitting with the function

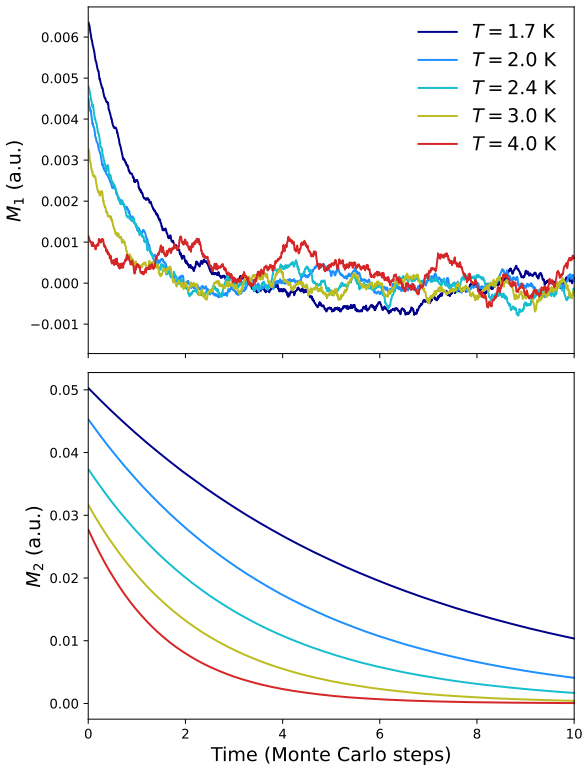

Figure 4.8 Extracted fast and slow magnetization response from Monte Carlo simulations when a field of strength 30 mT is suddenly applied at $t = 0$. The plotted contributions are defined as $M_1 = M_{\text{sat}} - M - A_2 e^{-t/\tau_2}$ and $M_2 = A_2 e^{-t/\tau_2}$ (*56*). The simulation is performed by Jonathan Hallén with details described in Chapter 2.3.

$$\log \Phi_1(t, T) = A(T) \; - t/\tau_1(T) \tag{4.6}$$

The examples of the fitting curves are shown in Figure 4.7 with a consistent fit quality factor $R^2 > 0.99$ (Figure 4.7C). The extracted Φ_1 for all the measured temperatures and in both magnetic field directions are exhibited in the upper panels of Figure 4.6. An approximate ratio of 1/3 between the amplitude of Φ_1 and Φ_2 can be seen for all temperatures, providing more insights for the relation of reconfiguration (fast-decaying) and polarization (slow-decaying) current. In comparison to the theoretical extraction of the two current regimes (Figure 4.8), both theory and experiment reveal the fast-decaying current, which becomes stronger for lower temperature, while in the simulation, the ratio

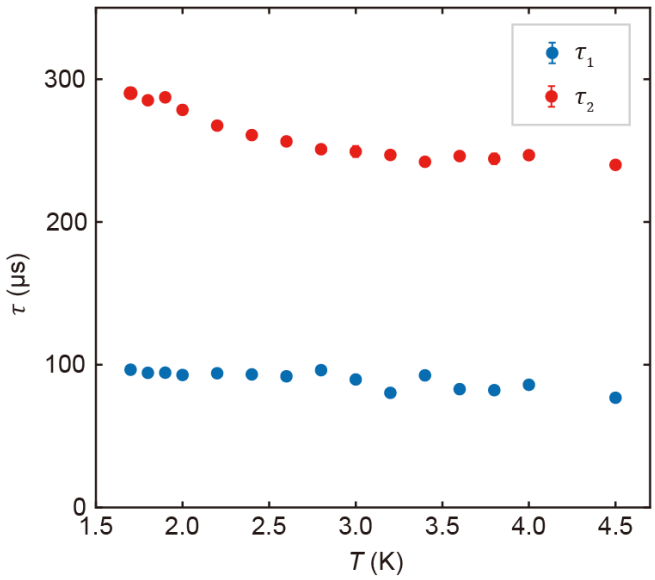

Figure 4.9 Experimentally determined relaxation time constants from all measured temperatures. Slow-decaying time constant is denoted as τ_2 in solid red; fast-decaying monopole current time constant τ_1 in solid blue. Error bars are smaller than the dots.

between the two currents is more drastic. The possible explanation for this observation is discussed in later sections.

Lastly and perhaps most importantly, by fitting Eqn. 4.5 and 4.6, the relaxation time constants for Φ_1 and Φ_2 can be measured. As shown in Figure 4.9, the τ_1 for the fast-decaying reconfiguration current remains a constant throughout the temperature range. Since τ_1 is not dependent to the temperature, this implies that flipping process is not thermally activated and indicates the quantum nature of the spin-flipping process. On the other hand, τ_2 for the time constant of the slow-decaying polarization current grows as the temperature is lowered. Note that τ_2 is not another spin-flipping rate at the monopole termini. Instead, it corresponds to the collective monopole relaxation from the polarization process. The ratios of τ_1/τ_2 for all the measured temperatures are compared with simulation and other experiments later.

4.3.2 Polarization and Depolarization

Interestingly, by applying a step-wise magnetic field excitation, we can not only study the current transient from the zero-magnetization state, but also the current transient for the depolarization process from finite magnetization state to zero magnetization. In the monopole picture, the polarization and depolarization processes are in fact asymmetric. As introduced in Chapter 2.1, in the polarization process, the magnetic current is induced by the external field against the entropic force, while for the depolarization from a finite magnetized state, the magnet current is driven purely by the entropy (see Eqn. 2.8 when $H = 0$). Hence, these two processes should be asymmetric. Motivated by this, we examine the depolarization current in the same procedure. Figure 4.10 shows the comparison of the flux response from the polarization (left) and depolarization process (right) from the same data set with the same temperature and field

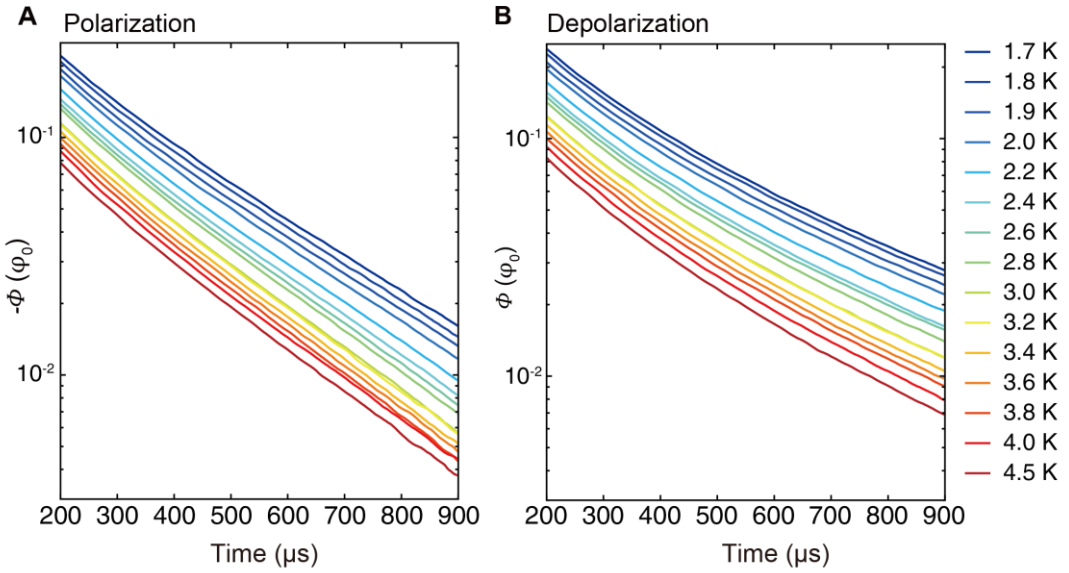

Figure 4.10 Comparison of measured flux $\Phi_S(t)$ for the polarization and the depolarization process for all measured temperatures. (A) $\Phi_S(t)$ of zero magnetization to finite magnetization. (B) $\Phi_S(t)$ of finite magnetization to zero magnetization state.

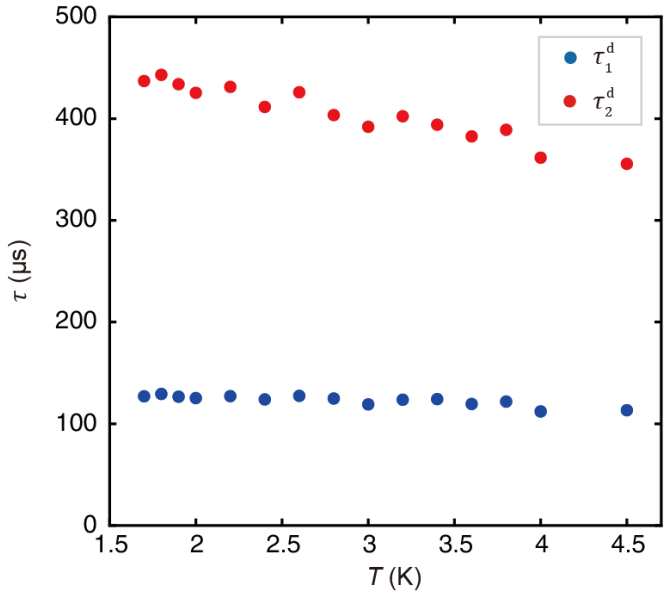

Figure 4.11 Relaxation time constants for the depolarization process from all measured temperatures. Similarly, τ_1^d (blue) and τ_2^d (red) represents time constant for fast-decaying monopole current and slow-decaying current.

condition. Interestingly, although the applied field is extremely small (B = 55 nT) and the system is considered to be in the linear response regime, the depolarization process clearly has a longer overall relaxation time than the polarization. Similarly, by fitting the flux response with Eqn. 4.5 and 4.6, one can derive the relaxation times τ_1^d and τ_2^d for the fast-decaying and slow-decaying currents for the depolarization. The extracted time constants are plotted in Figure 4.11, showing a similar trend of temperature dependence. For the depolarization, τ_1^d stays constant and is basically equivalent to the τ_1 of the polarization. As for τ_2^d, despite diverging similarly with lower temperature, the relaxation time is consistently longer than τ_2 by about 100 μs. This causes depolarization curves (Figure 4.10B) to look more non-linear. The difference between τ_2 and τ_2^d is expected to be larger at a lower temperature, which may relate to the magnetic hysteresis (*20*) and the memory effect (*54, 73*) when the experimental timescale sits between τ_2 and τ_2^d.

4.4 Magnetic Monopole Complex Conductivity

Since the time domain measurement reveals two current regimes, it is interesting and illuminating to resolve the current dichotomy in the frequency domain. To probe this possible presence of dichotomy, we study the monopole complex conductivity through the application of an AC sinusoidal magnetic field. As demonstrated in Figure 4.12A, the magnetic field $B_0(t) = B\cos(2\pi ft)$ with $B = 11$ nT (green trace) is applied in the typical frequency range from 10 Hz to 6000 Hz. The consequent flux response is shown as the dark blue trace in Figure 4.12A. Simultaneously, the monopole current, or the time derivative of the flux, is recorded after feeding the SQUID voltage output to the differentiator amplifier (light blue curve in Figure 4.12A). With the lock-in technique, the embedded amplitude and phase change of the monopole current can be determined by the measured flux over the frequency range. Under the alternating sinusoidal field, the flux response is recorded as Eqn. 3.4 and 3.5 in the lock-in measurement, and the monopole current is expressed as

$$J(t) = J_X \sin(2\pi ft) + J_Y \cos(2\pi ft) \tag{4.7}$$

Since the monopole current $J = \dot{\Phi}/\mu_0$, we can derive from Eqn 3.5 that

$$\dot{\Phi}(t) = -2\pi f\Phi_Y \sin(2\pi ft) + 2\pi f\Phi_X \cos(2\pi ft) \tag{4.8}$$

Therefore, the in-phase J_X is

$$J_X(f) = \frac{-2\pi f\Phi_Y(f)}{\mu_0} \tag{4.9}$$

while the out-of-phase part is

$$J_Y(f) = \frac{2\pi f\Phi_X(f)}{\mu_0} \tag{4.10}$$

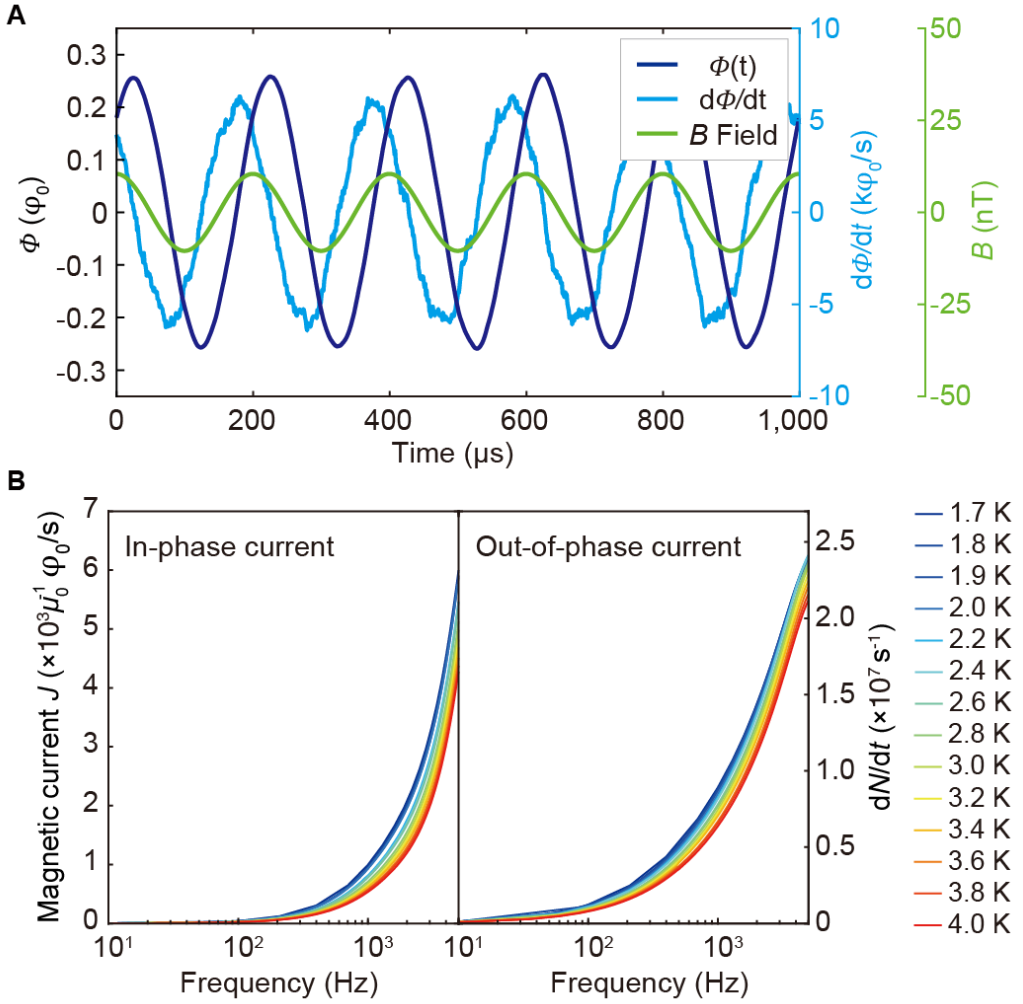

Figure 4.12 (A) Typical example of sinusoidal monopole current generation and detection, showing the magnetic field $B_0(t)$ (green trace), flux $\Phi_S(t)$ at the SQUID (dark blue trace) and $d\Phi_S(t)/dt$ (light blue curve). (B) The measured in-phase current $J_X \equiv -(2\pi f \Phi_Y)/\mu_0$ and out-of-phase current $J_Y \equiv (2\pi f \Phi_X)/\mu_0$. The corresponding rate $\dot{N}$ of the number of monopoles is shown as the right axis (Eqn. 4.11). The detailed quantitative value of monopole conductivity is shown in Appendix B.

Now the theoretical expression for monopole current $J(t)$ is clear. Experimentally, the lock-in circuit diagram is depicted in Figure 3.11B, which uses an external reference source to compensate the phase change from the LR effect. The time constant of the lock-in amplifier was set at 1 s for frequency below 100 Hz and 100 ms for frequencies above

100 Hz. The low pass filter was set at 18 dB/oct for all frequencies. The sensitivity of the lock-in amplifier was set to be 5 mV for all the frequencies. The measured in-phase monopole current J_X and the out-of-phase current J_Y are shown in Figure 4.12B at T = 1.7 to 4 K. In Figure 4.13, monopole current is plotted together with the corresponding rate $\dot{N}$ of number of monopole threading through the pickup coil, which can be estimated by

$$\dot{N} = \dot{\Phi}_S(t)/\mu_0 m = J/m \tag{4.11}$$

Interestingly, both in-phase and out-of-phase current grows rapidly with higher frequency, which is significantly different from the free electron Drude model, which has a complex electric conductivity of $\sigma_e(\omega) = \sigma_{e0}/(1 - \mathrm{i}\omega\tau)$. In Drude model, the real part of conductivity follows $\frac{\sigma_{e0}}{1+\omega^2\tau^2}$ and is more conductive at low frequency. For the imaginary part, Drude model follows $\frac{\sigma_{e0}\omega\tau}{1+\omega^2\tau^2}$ and thus has a maximum at $\omega = 1/\tau$. On the other hand, the monopole conductivity is more dielectric like, with increasing conductivity with higher frequency. This resembles the electric conductivity of the ionic water (*74*).

4.4.1 Dissipative Loss Angle Dichotomy

Since both in-phase and out-of-phase current have similar frequency dependence in our measured temperature range, to vividly visualize the underlying dichotomy, we analyze the loss angle, which takes the ratio between two currents. As with any fluid dynamics, the loss angle is defined as

$$\theta_{\mathrm{d}}(f) \equiv \arctan\left(\mathrm{Im}J_f/\mathrm{Re}J_f\right) \tag{4.12}$$

In practice, the loss angle is calculated from the in-phase and out-of-phase flux as

$$\theta(f) = \arctan\left(\frac{J_Y(f)}{J_X(f)}\right) = \arctan\left(-\frac{\Phi_X(f)}{\Phi_Y(f)}\right) \tag{4.13}$$

The loss angle for the measured temperature is shown in Figure 4.13, and a clear bump-

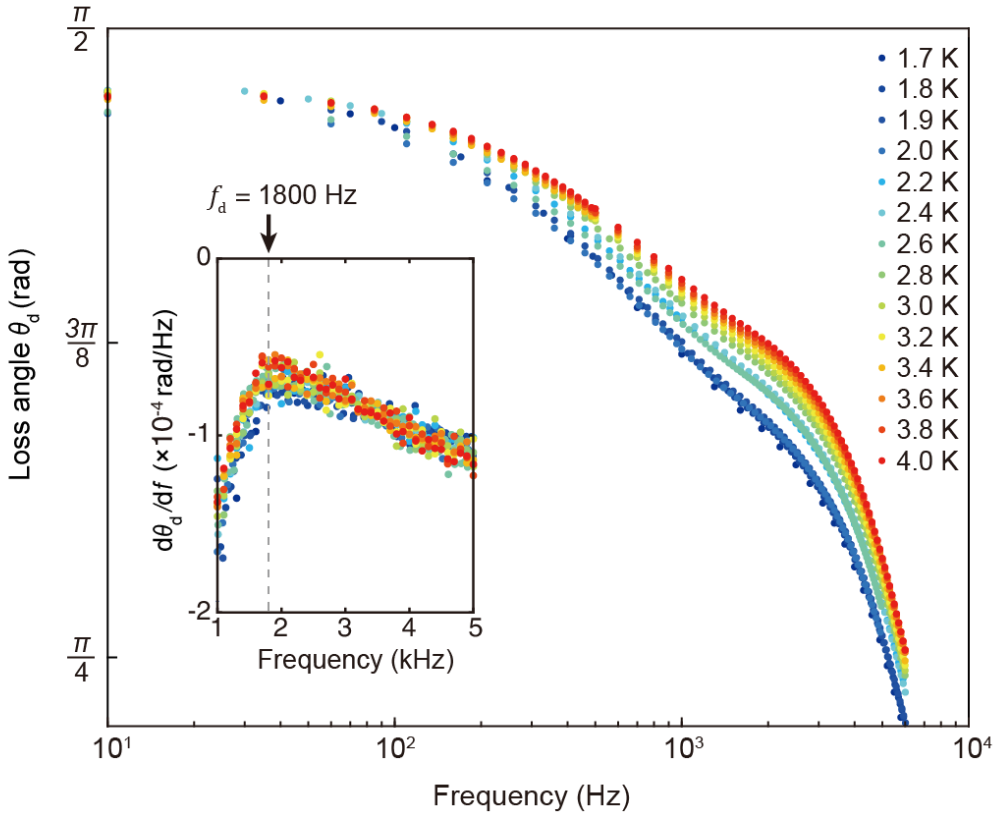

Figure 4.13 Measured $\theta_d(f)$ = arctan (ImJ_f/ReJ_f) from all temperatures studied. Inset shows the $\mathrm{d}\theta_d/\mathrm{d}f$, which reveals a dissipation transition occurs at $f_d \cong 1.8$ kHz.

like feature can be clearly seen in the intermediate frequency. This observation matches the expectation from the Monte Carlo simulation where the inflection point in the loss angle is due to the monopole being periodically driven into and out of the termini in the frequency range $\tau_{\mathrm{P}}^{-1} < f < \tau_{\mathrm{R}}^{-1}$. The inflection point in the loss angle indicates an increase of conductivity at the corresponding frequency. To pinpoint the characteristic frequency f_{d} associated with the change in $\theta_{\mathrm{d}}(f)$, we estimate $\mathrm{d}\theta_{\mathrm{d}}/\mathrm{d}f$ through a line wise numerical derivative

$$\frac{\mathrm{d}\theta_d}{\mathrm{d}f} = \frac{\Delta\theta_i}{\Delta f} \tag{4.14}$$

The loss angle derivative over frequency is plotted in the inset of Figure 4.13. Clearly, the

local maximum in $\mathrm{d}\theta_\mathrm{d}/\mathrm{d}f$ shows an inflection point around $f_\mathrm{d} \cong 1.8$ kHz, which is consistent for all loss angle studied and thus is temperature independent. Note that the existence of an inflection point marks the difference with the single timescale. For the single timescale model (e.g. Drude model), one would expect that the loss angle follows $\arctan(-\omega\tau)$ and without an inflection point. Therefore, it is important to plot the relaxation time constant corresponding to the inflection point, which can be deduced by

$$\tau_d = \frac{1}{2\pi f_d} \tag{4.15}$$

Figure 4.14 shows the corresponding τ_d for the loss angle measurement and exhibits a constant timescale. τ_d is consistent with the τ_1 extracted from the DC experiments and they are plotted together in Figure 4.21. Similarly, since τ_d is not dependent of the temperature. This again implies τ_d is not thermally activated and its quantum nature of the spin flipping.

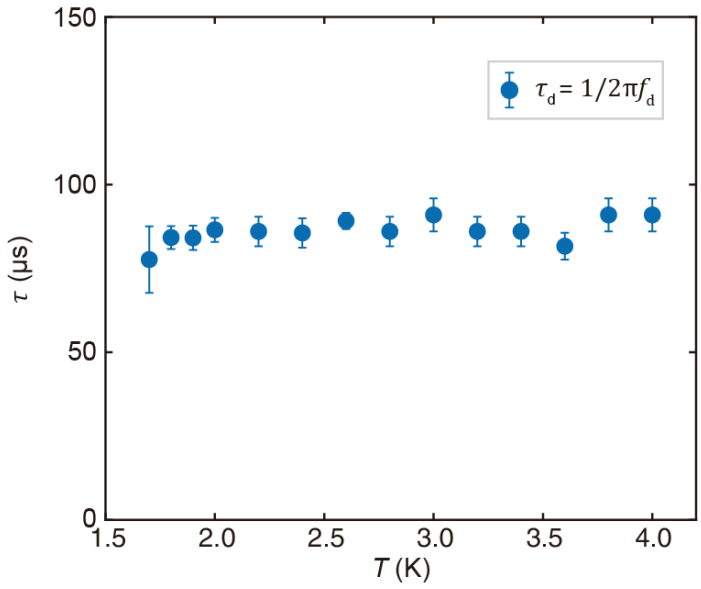

Figure 4.14 Relaxation time constant extracted from inflection point of dissipative loss angle where $\tau_d = 1/2\pi f_d$ with $f_d \approx 1.8$ kHz for all measured temperatures.

4.5 Magnetic Monopole Noise Dichotomy

Finally, besides the monopole current dichotomy and the dissipative loss angle dichotomy, we search for the change of the magnetic noise. One would expect the power of the magnetic noise in the reconfiguration current regime due to the excessive number of mobile monopoles that are not yet trapped in the monopole termini. To compare the magnetic noise in two regimes, I first discuss the zero-field monopole noise that is measured in ANDROMEDA.

4.5.1 Zero Field Magnetic Monopole Noise

As a sanity check and to make the foundation for comparing the noise in the fast-decaying current regime, we first study the zero-field magnetic monopole noise. The circuit diagram uses the configuration as in Figure 3.9 but with an additional voltage amplifier SR560 before the input 1 of the Moku ADC. The additional voltage amplifier serves as a bandpass filter from 0.1 Hz to 100 kHz at 6dB and provides extra gain of 10 to increase the SNR. Figure 4.15 shows the monopole noise PSD that is calculated from the measured 200 seconds flux time series recorded at 50 kSa. At each temperature, the time series data is divided into 1000 sections and performed PSD analysis through Eqn. 3.6 and 3.7. Furthermore, the noise spectrum is fitted with Eqn. 1.15 to extract the parameters such as spectral variance σ_Φ^2 and noise relaxation time τ_{PSD}. The extracted τ_{PSD} from the monopole noise is also shown in Figure 4.15. Both the overall noise spectral shape and the extracted parameters are in good agreement with previous works (*39, 46*).

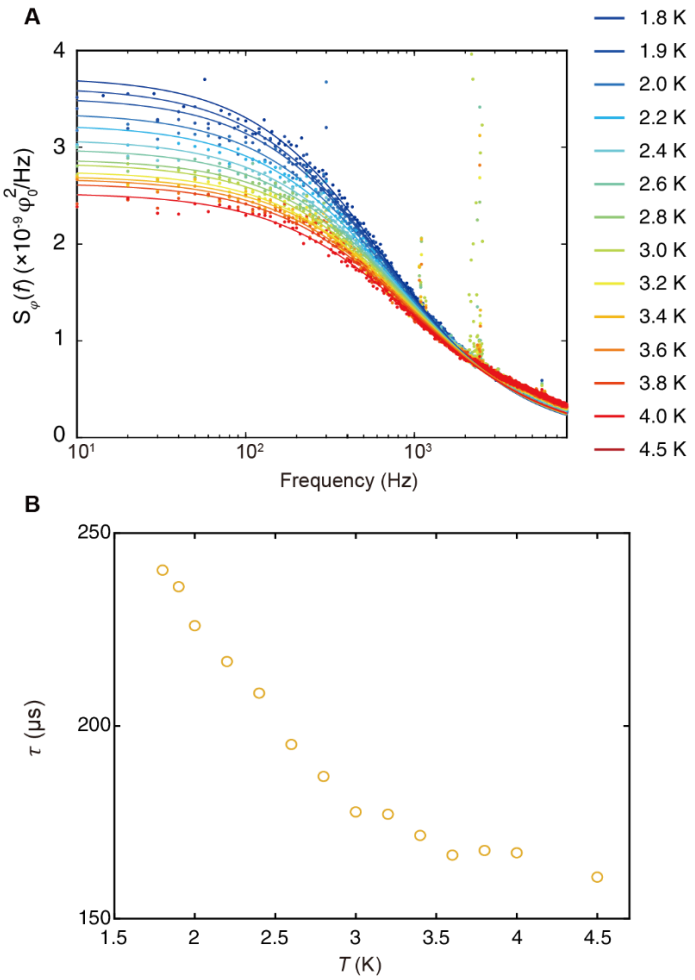

Figure 4.15 (A) Raw data of zero field monopole noise measured in ANDROMEDA. (The data out of the curve may be due to unwanted flux signal from the external vibration coupled to the SQUID spectrometer). (B) Extracted τ_{PSD} from (A) based on Eqn. 1.15.

4.5.2 Excessive Noise in Reconfiguration Current Regime

Now we turn our attention to the noise under a dynamical magnetic field. Since the magnetic response is also dynamical, we study how the noise intensity varies in time. The noise intensity is calculated first by obtaining the deviation of flux response $\delta\Phi(t)$ from the average flux response from Eqn. 3.9. Figure 4.16 shows the $\delta\Phi(t)$ from over 1000 transients. Clearly, $\delta\Phi(t)$ already appears to have larger deviation at times close to MCI.

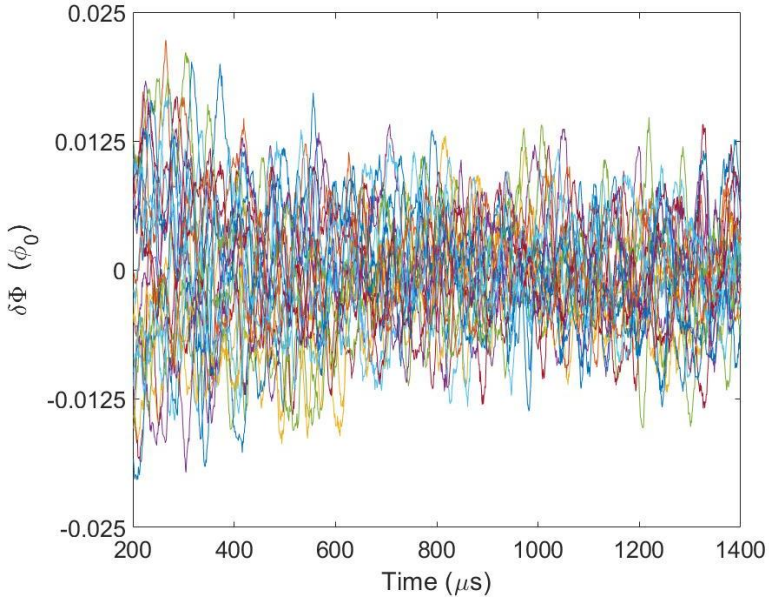

Figure 4.16 Examples of $\delta\Phi(t)$ over 1000 transients at $T = 2$ K, showing a clear stronger noise near MCI.

Next, to estimate quantitatively how much the noise increases in the fast-decaying current regime, we calculate the variance $\sigma^2 = \langle \delta\Phi^2 \rangle$ in time with Eqn. 3.10 and 3.11 by choosing a certain time window for averaging. That is,

$$\sigma_n^2(t_j) = \sum_{t_j = nt_{\text{shift}}}^{nt_{\text{shift}}+t_{\text{bin}}} \sigma^2(t_j) \quad (n = 0, 1, 2\ldots) \tag{4.16}$$

where t_{bin} represents the time interval for each averaging while t_{shift} is for the time shift for each iteration of the running averaging. For instance, Figure 4.17A shows variance over time with t_{bin}= 50 μs, t_{shift}= 50 μs. From the figure, the noise intensity decreases from MCI and saturates to the background value corresponding to zero field monopole noise power. This change in noise is also universal at all measured temperatures, as shown in Figure 4.17B.

Lastly, for best representing the specific noise power when the fast current exists, the time series variance σ_1^2 is averaged within the first 100 μs. That is, according to Eqn. 3.11, σ_1^2 is given by

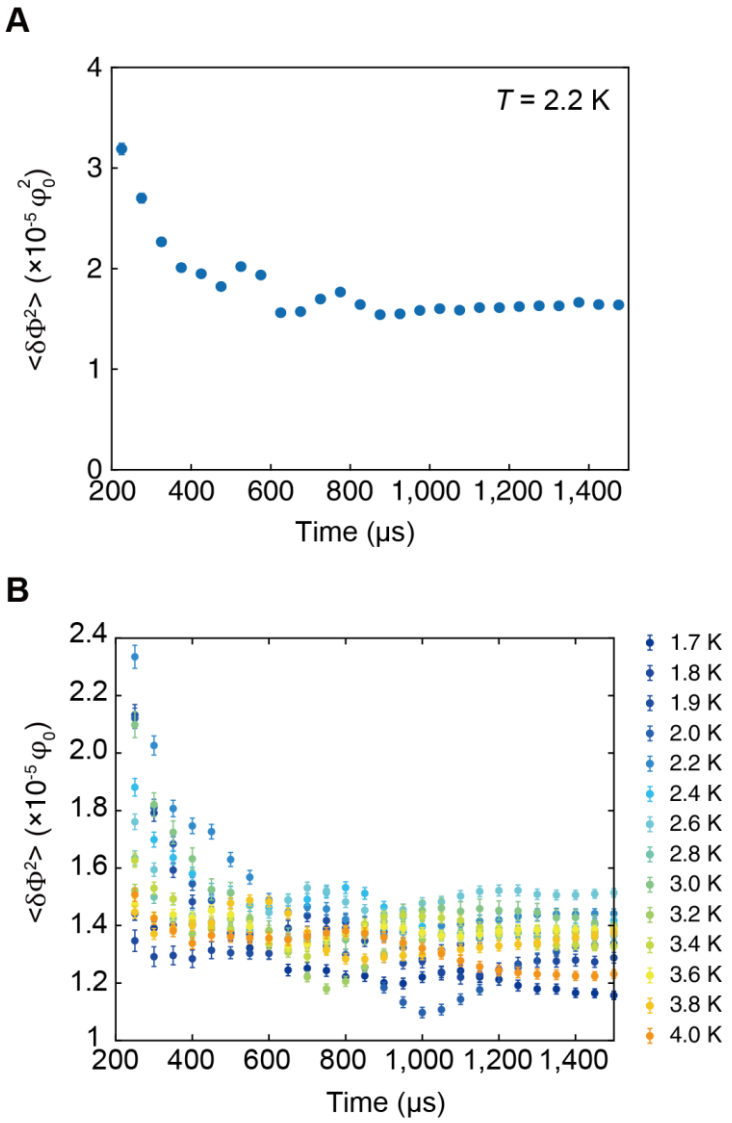

Figure 4.17 (A) Time series flux variance at 2.2 K. Each variance point is an average of a bin within 50 μs. (B) Temperature dependence of time series of flux variance. Each variance point is calculated by t_{bin}= 100 μs, t_{shift}= 50 μs.

$$\sigma_1^2 = \frac{1}{100}\sum_{t_j=200\ \mu s}^{300\ \mu s}\sigma^2(t_j) \tag{4.17}$$

On the other hand, the magnetization noise intensity σ_2^2 at the slow-decaying current is calculated in the time interval from 600 μs to 800 μs after MCI. That is,

$$\sigma_2^2 = \frac{1}{200}\sum_{t_j=600\ \mu s}^{800\ \mu s}\sigma^2(t_j) \tag{4.18}$$

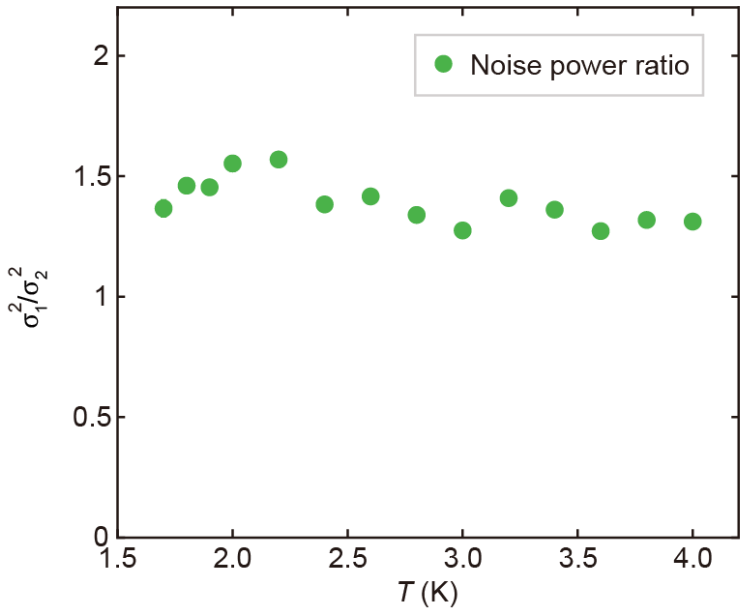

Figure 4.18 Ratio of monopole current driven magnetization noise intensity between fast-decaying current and slow-decaying currents (σ_1^2/σ_2^2). This ratio is constant at around 1.5 for all temperatures.

Taking the ratio between the noise power from two regimes provide an important quantitative description for the reconfiguration and polarization currents. Their ratio (σ_1^2/σ_2^2) is shown as Figure 4.18, where a constant ratio around 1.5 is seen for all measured temperatures. Hence, the current-driven magnetization noise power indeed drops steeply with the absence of fast-decaying current at $t \approx 600$ μs after MCI, which is expected from the number of immobile monopoles in termini.

4.6 Discussion

The three major experimental findings – monopole current dichotomy, inflection in the loss angle, and the steep drop of magnetization noise during current transient, are all interconnected with the preeminent feature of two distinct timescales. The two

timescales in monopole current transient, implying the two distinct spin flipping rate, is the essential ingredient for the bSM theory. Therefore, it is natural to relate the experimentally measured τ_1 and τ_2 directly to the τ_R and τ_P of the reconfiguration current and polarization current predicted in the bSM theory. In Figure 4.19, τ_1 and τ_2 from current dichotomy are plotted with the predicted τ_R and τ_P for comparison. Overall, bSM simulation and experiment exhibit good agreement that the ratio of two times $\frac{\tau_1}{\tau_2}$ hovers around 1/3 within T = 2.5 – 4 K. It is certainly notable that the Monte Carlo simulated τ_P increases significantly faster than the experimentally observed τ_2 upon lowering the temperature below 2 K. Neither the monopole density and the transport dynamics at high temperature above 3 K (see Appendix C) nor the demagnetization factor from the sample geometry (see Appendix D) could give rise to this discrepancy. The origin of the difference remains to be understood and can possibly be due to the field dependence of the monopole dynamics. Despite the fact that the MC simulation

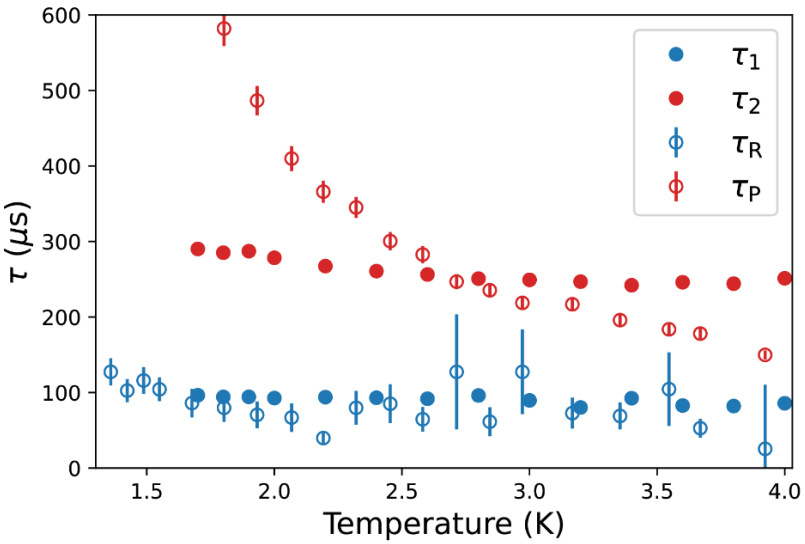

Figure 4.19 Comparison of experimental measured time constants τ_1 and τ_2 of fast and slow-decay currents with simulated τ_R and τ_P of reconfiguration and polarization currents.

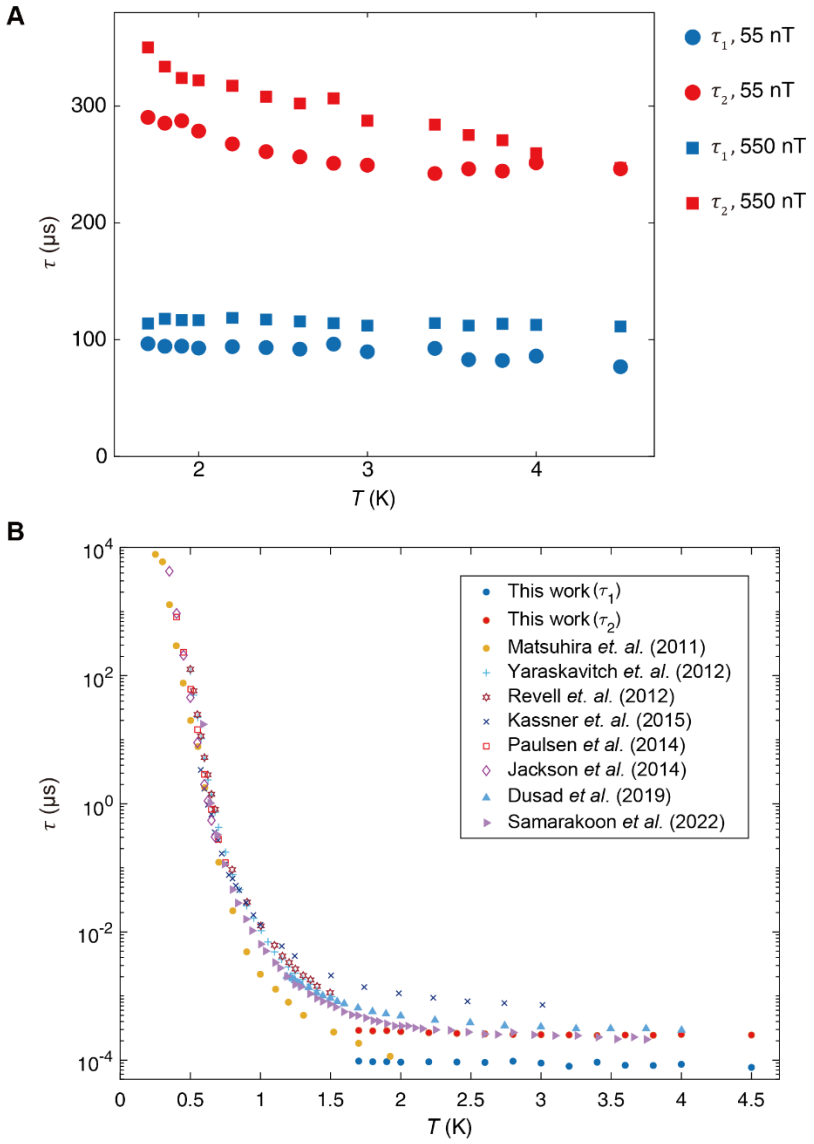

Figure 4.20 (A) Temperature dependence of τ_1 and τ_2 at two magnetic field strength (55 nT & 550 nT). (B) Temperature dependence of the measured relaxation time constant. The τ_1 and τ_2 from this work are plotted with the relaxation time constants from references in AC susceptibility data (*21, 22, 24*), correlation (*75*), DC magnetization (*76, 77*), and noise spectrum (*39, 46*).

shows negligible dependence on the field strength and the crystal orientation for the relaxation time constants, the current dichotomy experiment does reveal small changes in relaxation time constant at least for the slow-decaying current. As shown in Figure 4.20A,

by conducting the time-domain measurement in a ten times higher field (550 nT), the τ_1 corresponding to the fast spin flipping rate remains almost a constant, yet the slow-decaying current time constant increases more upon lowering the temperature. The fact that the simulation is performed at milli-Tesla range could explain the quantitative discrepancy. Furthermore, such field dependence is crucial when relating the relaxation time constant from this work to the time constants measured in the literature (Figure 4.20B) since the fit function and the applied field vary with experiments. The experimental result on the field dependence also implies that the microscopic monopole dynamics may be altered by the different magnetic field strengths. We leave further investigation of this potential field dependence as an avenue for future work.

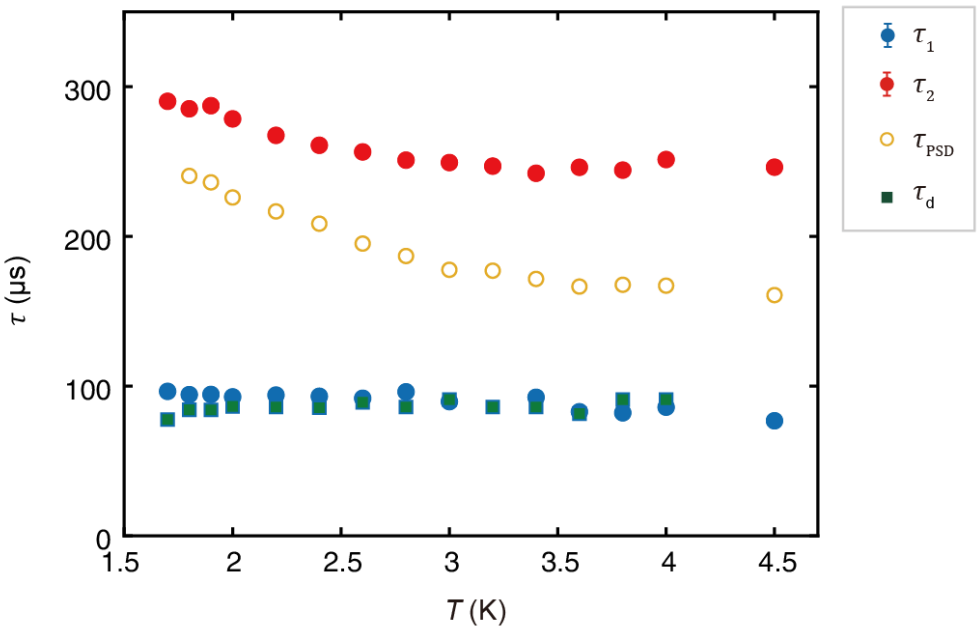

Figure 4.21 A combined plot of relaxation time constants derived by three different experimental techniques (DC, AC measurement, and noise spectrum).

Finally, I would like discuss the time constants extracted from the three techniques of the monopole current/noise spectrometer (DC, AC, and noise). Figure 4.21 shows the

combined plot of τ_1, τ_2, τ_{PSD}, and τ_d. Amazingly, the almost perfect match between τ_1 and τ_d throughout the measured temperatures strengthens the evidence for the quantum mediated fast spin-flipping process in $Dy_2Ti_2O_7$ of approximately 90 μs. Moreover, τ_2 and τ_{PSD} have two slightly different quantitative values despite having similar trends in temperature. Surprisingly, the observation that τ_{GR} sits exactly in the middle between τ_1 and τ_2 possibly indicates that the essence of zero field noise as a mixture of two hopping processes.

Overall, the discovery of a dynamical fractal pathway governing the equilibrium motion of monopoles in the canonical spin ice $Dy_2Ti_2O_7$ motivates the development of a new transport theory for the magnetic monopole current in spin ice. With the bSM Monte-Carlo simulation introduced in Chapter 2, this theory anticipates the dichotomy of driven current dynamics with measurable signatures. The cutting-edge monopole current/noise spectrometer developed to explore these predictions discovers the strong dichotomy in the current response under instantaneous field change, and in the dissipative loss angle in terms of the appearance of inflection point, as well as in the magnetization noise. Remarkably, in the scenario of monopole dynamics involving monopole termini to the motion, the mechanism involves the geometry of allowed trajectories due to dynamical constraints. This new paradigm is from self-generated dynamical heterogeneities in quantum magnets, not solely attributed to interactions or sample geometric constraints or quench disorder. Ultimately, this mechanism reveals a new avenue for exploring self-constrained quantum transport in other categories of quantum magnets.

Chapter 5 Discovery of Dynamical Heterogeneity in a Supercooled Magnetic Monopole Fluid

Part of this chapter appear as Dasini et. al., arXiv:2408.00460 *(2024).*

In Chapter 5, I discuss the work searching for the emergence of dynamical heterogeneity in DTO when entering the supercooled state (*78*) by looking after the coexistence of fast and slow relaxation time. Using the monopole noise spectroscopy, the exploration reveals the sharp bifurcation in the noise histogram, manifesting as current burst fluctuations whose magnitude evolves rapidly with falling temperature. Also, by measuring the noise and magnetic susceptibility simultaneously, the FDT relation in spin ice is examined extensively. The thorough investigation shows a transition from consistency to the violation of FDT in spin ice towards the ground state.

5.1 Dynamical Heterogeneity in a Glass-forming Liquid

One of the most challenging question in condensed matter physics is to understand the mechanism for the glass transition (*79*). What makes the theory for glass a fascinating and difficult conundrum is its mixture of characteristics from both fluid and crystalline. With falling temperature, glassy materials normally first transition from the liquid state to a supercooled state under experimental condition, then eventually to the glass state. Since glass can be regarded as a solid that flows or a highly viscous liquid, there are various approaches to tackle the problem, including the thermodynamic approaches (*80*), dynamic facilitation (a method where local relaxation time is dependent of the relaxation time of its vicinity) (*81*), elasticity approach (*82*), and geometrical frustration (*83, 84*). In

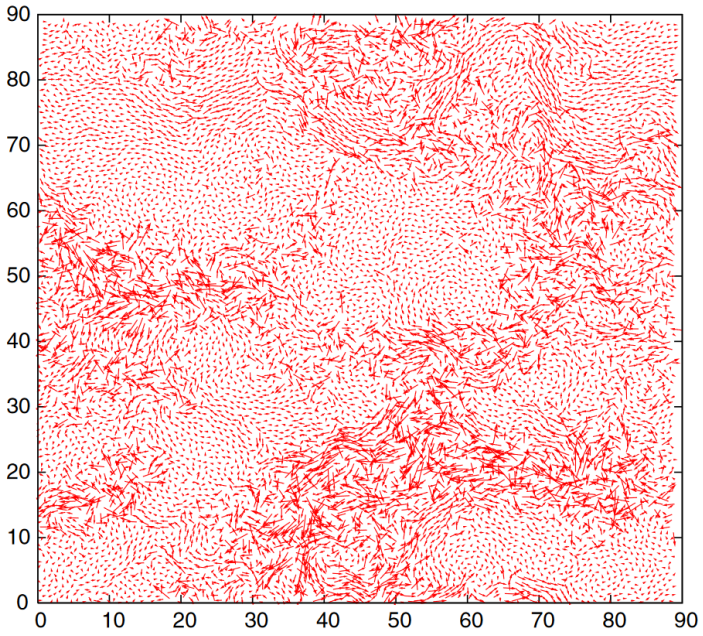

Figure 5.1 An example image of dynamical heterogeneity from the spatial map of single-particle displacement from supercooled liquid simulation. The length of arrow is plotted proportional to the inverse of its local structural relaxation time. Figure adapted from ref. (*85*).

addition, dynamical heterogeneity, which describes the phenomenon of nontrivial spatiotemporal fluctuations (see Figure 5.1 adapted from ref. (*85*)) emerging in the supercooled liquid (*85, 86*), is a substantial component of the glass-forming theory. Experimentally, dynamical heterogeneity is often characterized by the super-Arrhenius temperature-dependence of relaxation rate, the broad distribution of relaxation time and the non-Gaussian statistics of the fluctuations (*87*). It is fundamentally interesting and important to understand whether the spin analogue of the glass-forming liquids also possesses dynamical heterogeneity phenomena and how its nature resembles and differs from other glassy systems. In our macroscopic measurement, dynamical heterogeneity would be the coexistence of the magnetization excitations with different timescales.

For the canonical spin ice materials, a previous work (*21*) has shown that the emergent monopole fluid enters the supercooled state below 1 K, as identified by the Vogel–Tammann–Fulcher (VTF) form of relaxation time. That is,

$$\tau(T) = \tau_0 \exp(DT_0/[T - T_0]) \tag{5.1}$$

where D is the fragility index and T_0 is found to be ≈ 240 mK (*21*). Furthermore, the relaxation time is extracted from the magnetic susceptibility parametrized by the Havriliak-Negami (HN) form with broadened relaxation time distribution. More explicitly,

$$\chi(\omega, T) = \chi_\infty + \chi_0(T)/\left(1 + (i\omega\tau(T))^{\alpha_{\mathrm{HN}}(T)}\right)^{\gamma_{\mathrm{HN}}(T)} \tag{5.2}$$

where $\alpha_{\mathrm{HN}}(\mathrm{T})$ and $\gamma_{\mathrm{HN}}(T)$ describe the broadening and asymmetry of the relaxation rates. It was claimed (*21*) the consistency of HN form magnetic susceptibility in $Dy_2Ti_2O_7$ implies the entry into the supercooled state and suggests out that dynamical heterogeneity may exist (*88*). Moreover, two recent theories based on the extended spin ice model (spin ice model that considers second and third nearest neighbor exchange interaction) predict some form of dynamical heterogeneity: the spin slush model (*89*) and the dynamical fractal transport theory (*27*). In the spin slush model where a broader ground state manifold is considered, dynamical heterogeneity emerges as spatially local clusters from a broader ground state manifold (or spin slush), while in the beyond standard model (bSM), dynamical heterogeneity appears naturally due to the distinct spin flipping rate permeating throughout the crystal. In particular, a secondary slower spin flipping process causes the trajectory of a monopole to be confined in a fractal percolative cluster. Due to the common feature of dynamical heterogeneity in these models, these models motivate us to search for the empirical existence and phenomenology for dynamical heterogeneity of monopole fluid and how it enters from the supercooled state to the glassy state.

To search for dynamical heterogeneity in $Dy_2Ti_2O_7$, we employ simultaneous high precision magnetic susceptibility and magnetization noise measurements to validate the fluctuation-dissipation theorem in DTO. By using SQUID-based noise spectrometer as a direct probe of magnetization fluctuation, we scrutinize the statistics of the monopole random dynamics throughout the temperature range 15 mK< T< 3 K on a cryofree dilution refrigerator. It is expected from the spin slush model (*89*) that approximately 2-4% of Dy spins remain active even as the $T \rightarrow 0$.

5.2 Examination of Fluctuation-Dissipation Theorem

Dynamical heterogeneity in glass-forming liquids often accompanies the violation of the FDT relation (*90, 91*). Furthermore, the loss of the ergodicity is predicted theoretically, caused by the growing dynamical heterogeneity when the spin-spin correlation diverges upon lowering the temperature (*21, 62*). Therefore, we first examine the fluctuation-dissipation theorem in DTO at varying temperatures and in a wide frequency range (0.1 – 1000 Hz). To probe the low frequency regime below 10 Hz, an internal reference is used and the time constant is always chosen three times more than the inverse of the measured frequency ($\tau_{LI} \geq 3/f_{\min}$). As for the low frequency noise measurement, an extra SR560, which serves as a band-pass filter (f_{HP} = 0.03 Hz; f_{LP} = 3 kHz), is added after the SQUID output before the recording from the GHz ADC. The frequency domain noise spectrum is then calculated from time series data based on Eqn. 3.6. Figure 5.2A shows an example of measured frequency-dependent magnetic susceptibility $\chi'(\omega, T)$, $\chi''(\omega, T)$ and magnetization noise PSD $S_M(\omega, T)$ at T = 700 mK. The full set of magnetic susceptibility data and the conversion from the SQUID voltage output is described in Appendix E.

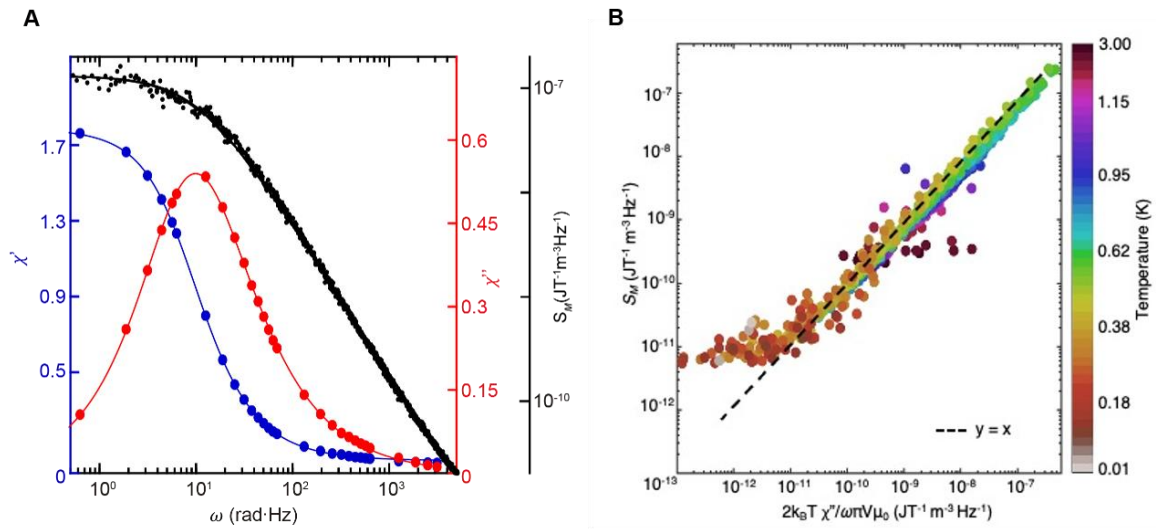

Figure 5.2 (A) Typical examples of simultaneously measured $Dy_2Ti_2O_7$ magnetic susceptibility $\chi'(\omega,T)$, $\chi''(\omega,T)$ and $S_M(\omega,T)$ at T = 700 mK. (B) Magnetization noise $S_M(\omega,T)$ versus $2k_BT\chi''(\omega,T)/\omega\pi V\mu_0$ as a function of angular frequency and temperature. Temperature dependence is marked by the color code and the y = x dashed line is shown for guidance.

For an ergodic random process of a magnetic system, FDT links $\chi''(\omega,T)$ and $S_M(\omega,T)$ through Eqn. 2.16. To visualize and explore the evolution of FDT over the temperature range 14 mK $< T <$ 3000 mK, $S_M(\omega,T)$ versus $2k_BT\chi''(\omega,T)/\omega\pi V\mu_0$ is plotted in Figure 5.2B. If FDT relation holds, the quantitative value for $S_M(\omega,T)$ and $2k_BT\chi''(\omega,T)/\omega\pi V\mu_0$ should be equivalent and thereby exhibit a straight line with slope = 1. That is, by defining the ergodicity function $X(\omega,T)$ as

$$X(\omega,T) = 2k_BT\chi"(\omega,T)/\omega\pi V\mu_0 S_M(\omega,T) \quad (5.3)$$

$X(\omega,T)$ should be observed constant at 1 if FDT is valid. Clearly, in Figure 5.2B, FDT relation holds at high temperature $T >$ 500 mK. However, below T~500 mK, $Dy_2Ti_2O_7$ slowly exits the ergodic regime, manifesting a departure between S_M and the measured $2k_BT\chi''(\omega,T)/\omega\pi V\mu_0$. It is evident that below $T <$ 250 mK, FDT is strongly

violated and the monopole random dynamics are non-ergodic. In addition, $\bar{X}(T)$ is the average of $X(\omega, T)$ for all measured frequencies at a certain temperature, which is plotted in Figure 5.11(ii). An example of frequency dependence of $X(\omega)$ is also shown in Appendix E.

5.3 Monopole Current Burst

A key signature of dynamical heterogeneity, or the coexistence of slow and fast relaxation regions whose nature can be compact or fractal, would be random monopole current bursts (*89*). Therefore, we examine the time series of the monopole current $J(t, T)$ over a wide temperature range. Each point in time of $J(t, T)$ is acquired from the numerical derivative of the flux signal (Eqn. 4.1, $J = \dot{\Phi}_p/\mu_0$).

$$\dot{\phi}_p(t) = \frac{\phi_p(t+\Delta t)+\phi_p(t-\Delta t)}{2\Delta t} \tag{5.4}$$

Then, to suppress any artifacts in numerical derivatives, $\dot{\phi}_p$ is further averaged within every 80 μs. As a result, since there is no net current under zero field, the typical monopole current fluctuation magnitude $|J(t)|$ is shown in Figure 5.3A. Clearly, between 0.5 K to 1.5 K, a rapid change in the monopole current can be observed frequently within the time window, manifesting the existence of the current burst. The corresponding probability distribution of $|J(t)|$ is presented in Figure 5.3B. Strikingly, the monopole current fluctuation throughout the temperature ranges over four orders of magnitude.

Figure 5.4A exhibits the complete temperature dependence of the time rate of $r_{|J|}$ of the monopole current. $r_{|J|}$ is calculated by counting the number of data n_J with

magnitude $|J|$ over a finite time interval t_J ($r_{|J|} = n_J/t_J$). To visualize the change of the monopole current bursts, Figure 5.4B shows the temperature evolution of average monopole current. It is clear that the average monopole current reaches a maximum at around 1 K and drops rapidly once entering the supercooled state. One possible scenario for now the monopole current bursts can happen is that synchronized monopole transport occurs locally as the monopoles in proximity could trigger the motion of one another. For example, monopole motion can be unblocked from the local cluster (like the fractal percolative cluster in dynamical fractal theory). This unblocking of local magnetic monopoles releases the dynamical motion and thus generating current bursts of different intensities.

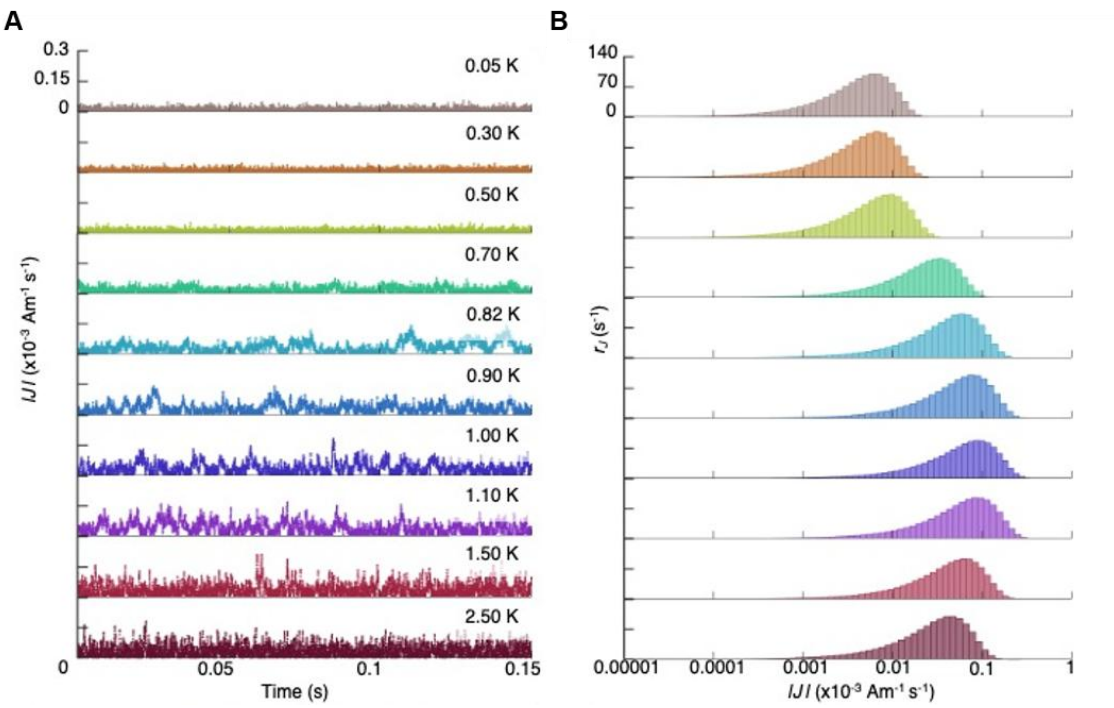

Figure 5.3 (A) Typical measured time sequences of monopole current magnitude $|J(t)|$. (B) The corresponding probability distribution calculated from the count n_J of current J within a fixed time interval t_J ($r_{|J|} = \frac{n_J}{t_J}$). versus the monopole current bursts $|J(t)|$ in (A).

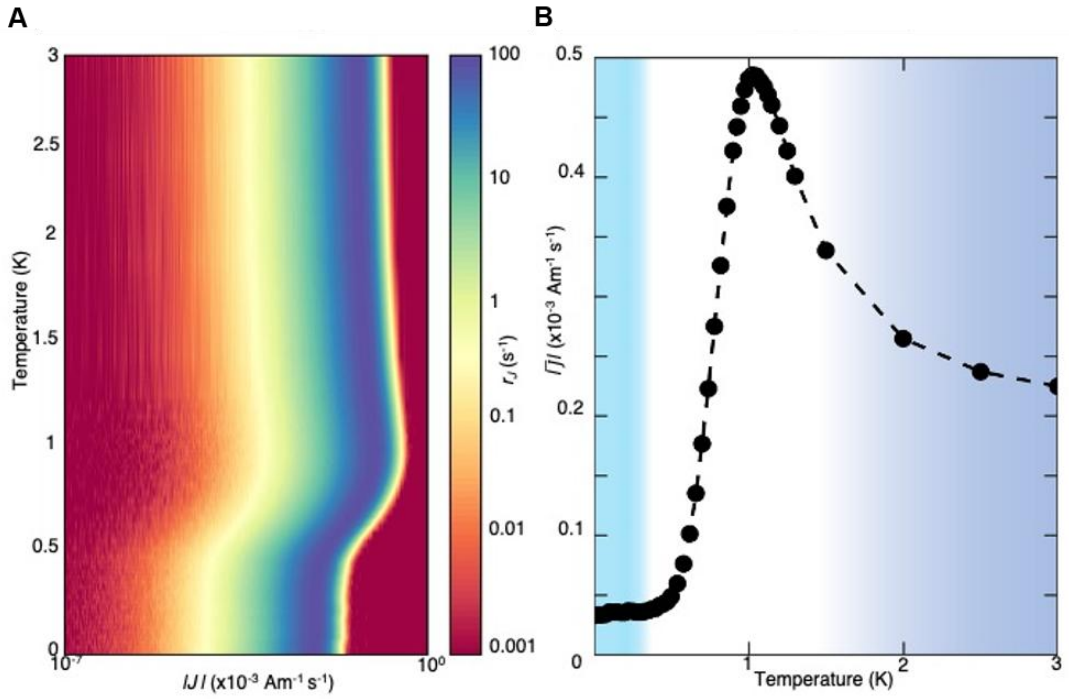

Figure 5.4 (A) Temperature dependence occurrence rate $r_{|J|}$ ($r_{|J|} = \frac{n_J}{t_J}$). of monopole current bursts with magnitude $|J|$. The horizontal line cut of this figure would be Figure 5.3B. (B) Temperature evolution of average measured intensity of monopole current bursts $\overline{|J|}$.

5.4 Noise Bifurcation and Dynamical Heterogeneity

5.4.1 Bifurcation of Magnetic Monopole Noise

Since the monopole current statistics reveal interesting characteristics of monopole motion which hint at dynamical heterogeneity, it would be equally interesting to study the relevant energy. The energetic characteristic may be hidden in the overall noise spectrum and thus the statistics of time series of flux is investigated thoroughly. For example, Figure 5.5A shows a typical time series of flux (green) in comparison to the background noise without sample (black), demonstrating a strong magnitude of flux noise from the DTO crystal. Based on the circuitry of the pickup up (Figure 3.9), the energy ε related to the change of the monopole configuration is restored in the energy of a inductor.

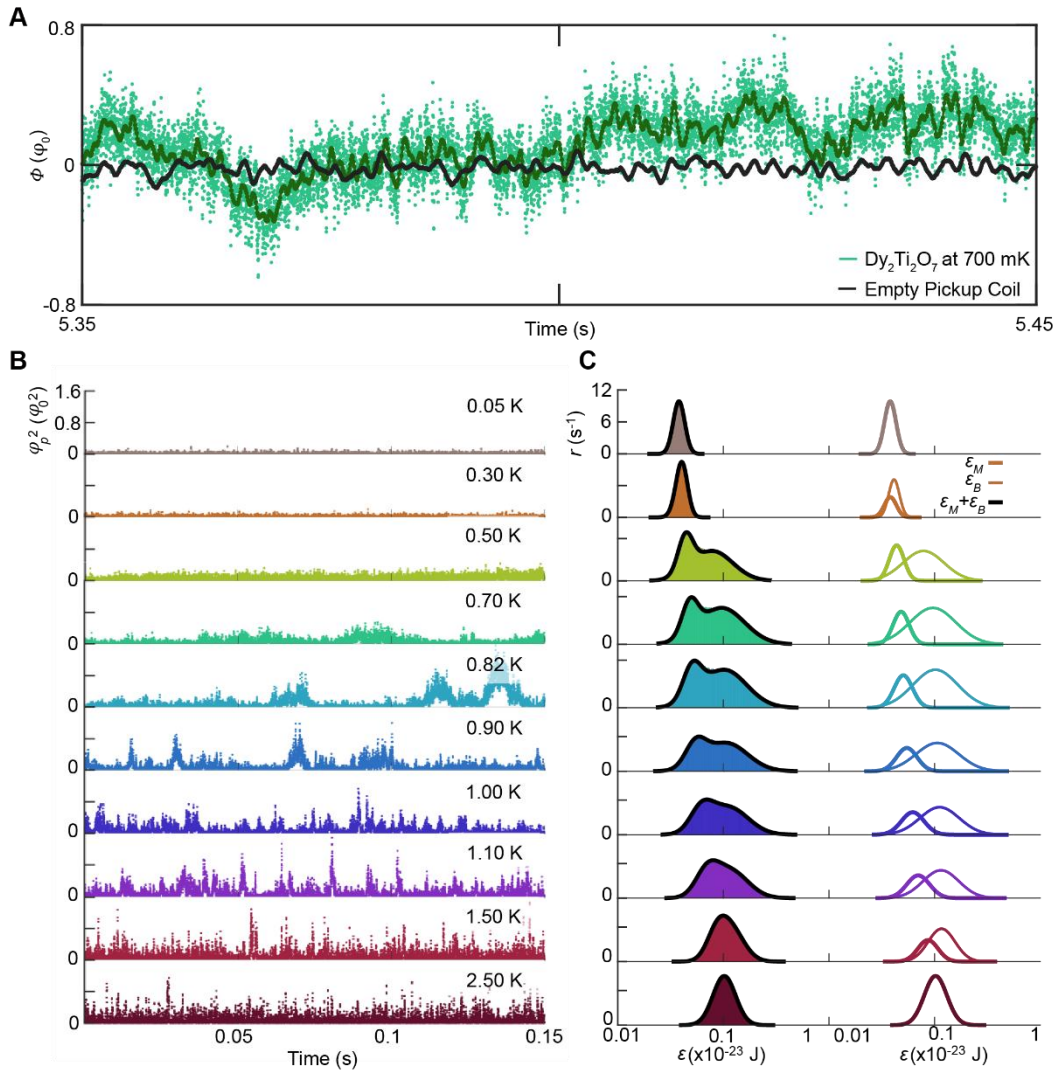

Figure 5.5 (A) Typical example of $\Phi_p(t)$ for DTO flux noise with current bursts (green) and for the absence of sample (black). (B) Typical examples of the $\Phi_p^2(t)$ from directly measured time series spontaneous magnetic flux from T = 50 mK to 2500 mK. (C) The corresponding flux energy occurrence rate histogram to (B). The right panel shows the result of bi-modal fitting.

Therefore, this energy can be derived from the measured flux as

$$\varepsilon \equiv \Phi_p^2(t,T)/2L_p \tag{5.4}$$

where L_p is pickup coil inductance ($L_p = 0.71$ μH). To visualize the change of flux noise and its corresponding energy events across temperatures, Figure 5.5B shows examples of

flux square at pickup coil $\Phi_p^2(t,T)$ for the time interval about 150 ms from 50 mK to 2500 mK. Strikingly, one can already see a crossover from a powerful Gaussian noise to a random process with temporal spikes around 1 K, then eventually noise power drops rapidly back to Gaussian noise at the lowest temperature. Next, we analyse rate of occurrence $r(\varepsilon,T)$ for each energy event ε at certain temperature. Likewise, $\Phi_p^2(t,T)$ is averaged within 80 μs boxcar to avoid numeric error then is converted into $\varepsilon(t,T)$ with Eqn. 5.4 (see Figure 5.6). As a result, Figure 5.5C plots the rate of occurrence $r(\varepsilon,T)$ histogram, which is defined by counting the number of events $n_\varepsilon(\varepsilon)$ over the time interval t_ε ($r(\varepsilon,T) = n_\varepsilon(\varepsilon,T)/t_\varepsilon$), versus the ε corresponding to Figure 5.5B. Clearly, a deviation from a pure Gaussian distribution can be observed between 0.5 K and 1.1 K from the sharp bifurcation of noise peak in the distribution. By lowering the temperature from T = 3 K, the flux noise first appears with narrow Gaussian distribution. Accompanied by random monopole current bursts, the noise distribution reveals a combination of bi-modal Gaussian peaks (marked by $\bar{\varepsilon}_M$ and $\bar{\varepsilon}_B$). Thus, in the right panel of Figure 5.5C, the overall distribution is fitted by

$$\varepsilon_M + \varepsilon_B = A_M \exp\left(-\frac{(\varepsilon-\bar{\varepsilon}_M)^2}{2\sigma_M^2}\right) + A_B \exp\left(-\frac{(\varepsilon-\bar{\varepsilon}_B)^2}{2\sigma_B^2}\right) \quad (5.5)$$

$\bar{\varepsilon}_M$ can be attributed to conventional monopole noise that is observed blow 4 K (*39*), while $\bar{\varepsilon}_B$ is the additional distribution from the current bursts. In the case of T >1.5 K or T < 300 mK where the bi-modal fitting fails (either one distribution is vanishingly small or two distributions are essentially overlapping), we infer that the current bursts are no longer a prominent effect in the flux signal. Further lowering the temperature below T < 250 mK, flux noise shows a re-entrant Gaussian distribution together with the disappearance of the monopole bursts.

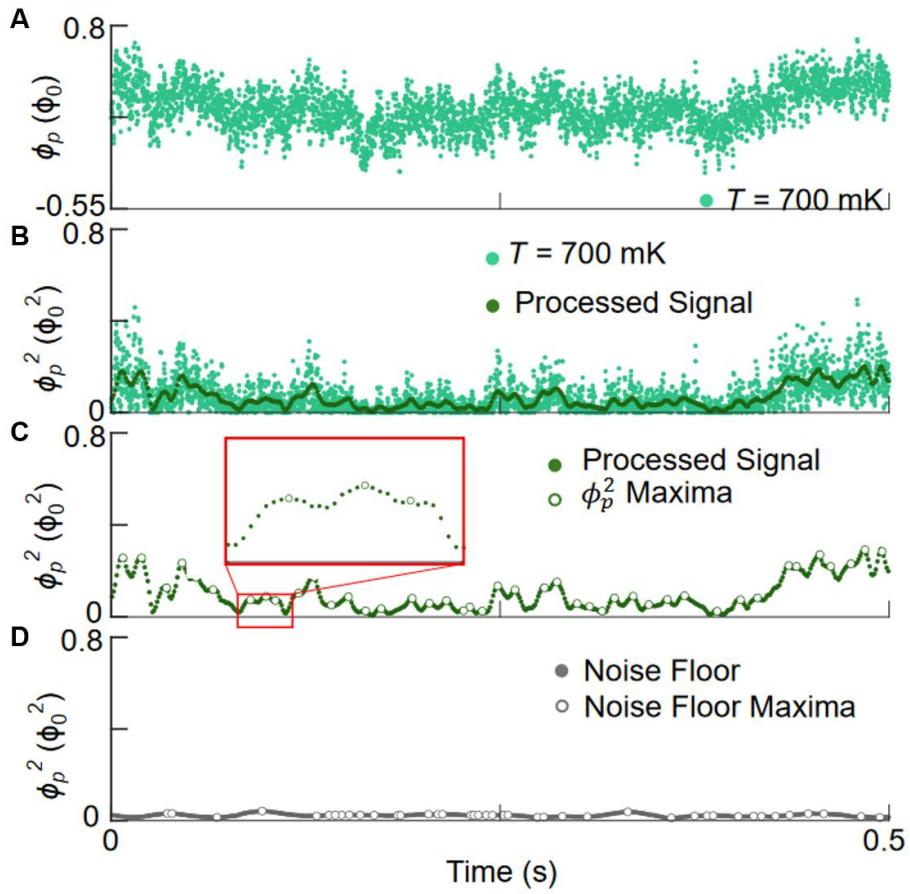

Figure 5.6 Step-by-step procedure for extracting energies from flux time series. (A) Typical flux time series signal Φ_p (B) Flux square signal Φ_p^2 and its average within every 80 μs. (C) Local maxima of averaged Φ_p^2. (D) Comparison of flux signal without sample.

To identify the peaks in the flux energy distribution and study how $\bar{\varepsilon}_M$ and $\bar{\varepsilon}_B$ evolve with temperature, the complete set of flux square occurrence rates $r(\varepsilon, T)$ is shown as a two-dimensional histogram in Figure 5.7A. The monopole bifurcation phenomenology is characterized by fitting the bi-modal distribution and tracing the local maximum, as marked by the dotted curves corresponding to $\bar{\varepsilon}_M$ and $\bar{\varepsilon}_B$. The extracted traces for the relative intensities of monopole current burst $\bar{\varepsilon}_B$ and GR noise $\bar{\varepsilon}_M$ are then plotted in Figure 5.7B. These two traces identify three distinct regimes for the temperature dependent of the monopole dynamics. These are (I) dark blue region with thermally

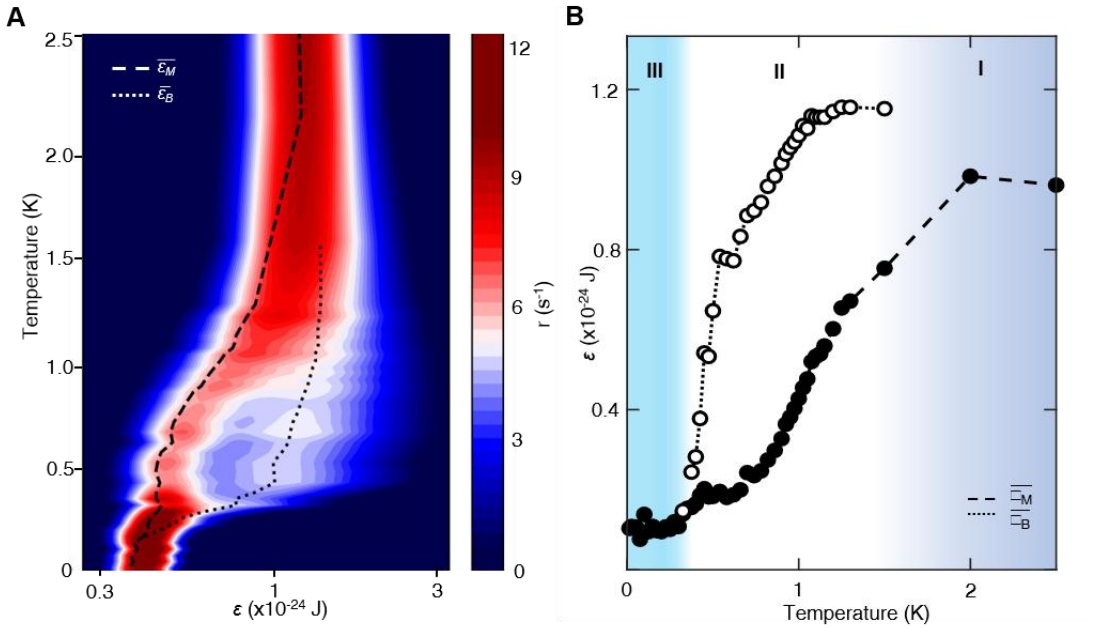

Figure 5.7 (A) 2D flux energy occurrence rate histogram versus temperature. Local maximum for conventional monopole noise distribution $\bar{\varepsilon}_M$ and monopole current bursts $\bar{\varepsilon}_B$ are marked by the dash/dot curve. (B) Extracted average energy of $\bar{\varepsilon}_M$ and $\bar{\varepsilon}_B$ from (A), revealing three regimes of monopole dynamics. Note that theoretically a monopole passing through the pickup coil could produce a flux with $\Phi = \mu_0 m$. By taking experimental parameters into accounts, one monopole produces $2 \times 10^{-3} \varphi_0$, corresponding to an energy event of $\varepsilon = 1.3 \times 10^{-29}$ J.

activated diffusive monopole fluid, (II) white region with monopole dynamical heterogeneity accompanied by random monopole current bursts, and (III) light blue region where the two peaks merge back to the single Gaussian distribution. Especially for regime (III), it is unexpected that magnetization dynamics remains finite even below the freezing temperature (see also Figure 5.10B that the signal is always above the background noise floor).

5.4.2 Monopole Dynamical Heterogeneity Energy Analysis

Now the flux noise contributed by the monopole current bursts has been identified

to exist below $T \ll 1500$ mK. Notably, the measured $r(\varepsilon)$ reveals a unique distribution for the energy configuration that was unexplored before. For the conventional supercooled fluid, the energy configuration, or the energy landscape is often studied. We thus consider the heterogeneous monopole and its surrounding spin configurations (labeled as i and with energy E_i) whose energies are explored dynamically through thermal activation. In this scenario, we evaluate the local maximum energy E of the monopole current burst, which is derived from the local maxima of $\varepsilon(t)$, or Φ_p^2. As demonstrated in Figure 5.6C, local maxima of Φ_p^2 are extracted, and hence its corresponding energy is

$$E = \phi_{p,\max}^2(t,T)/2L_p \tag{5.6}$$

Similarly, the rate of occurrence $R(E)$ for energy E can be calculated by the count of events $n_E(E)$ in a given time interval ($R(E,T) = n_E(E,T)/t_E$). Typical results of $R(E,T)$ versus the energy E are plotted in Figure 5.8A. It can be vividly observed that $R(E,T)$ shows an exponential distribution in energy E, manifesting as a straight line in the semi-log plot. The complete set of $R(E,T)$ is shown in Figure 5.8B, revealing the temperature dependence. To explore the energy landscape, we consider a simplified model relating the probability of a transition with energy E to be

$$P(E,T) = N(T)\exp\left(\frac{-E}{kT}\right)/Z(T) \tag{5.7}$$

where $Z(T)$ is the partition function, while $N(T)$ is the number of magnetic monopoles following the temperature dependence of $N(T) = N_0\exp(-\frac{\Delta}{kT})$. Clearly, the logarithmic function of the probability would be

$$\mathrm{In}P(E,T) = -\ln Z - \frac{\Delta+E}{kT} + C_0 \tag{5.8}$$

Thus, the slope of $\mathrm{In}(E,T) - E$ graph should measure $\delta = \partial(\ln P(E,T))/\partial(E/kT)$,

which lies around 0~1. Such relation is observed below 450 mK (Figure 5.9), while in the high temperatures the occurrence rate deviates from this simplified model.

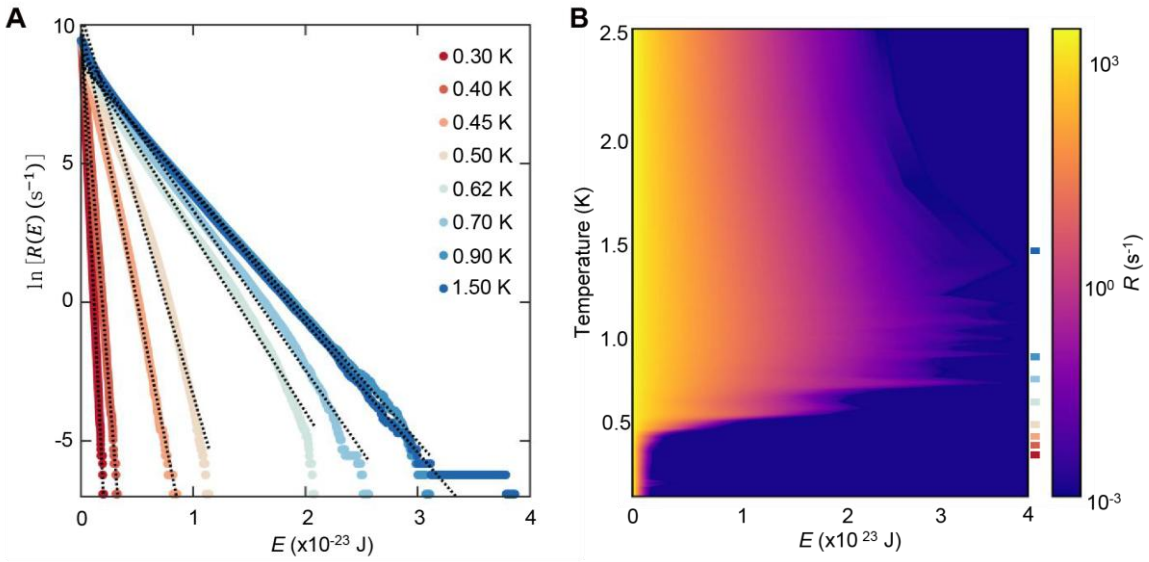

Figure 5.8 (A) Typical semi-log plot of monopole current bursts occurrence rate $R(E)$ versus the energy E at temperatures T = 300 mK to 1500 mK. (B) The colormap of $R(E)$ with complete temperature dependence of monopole current bursts versus energy E.

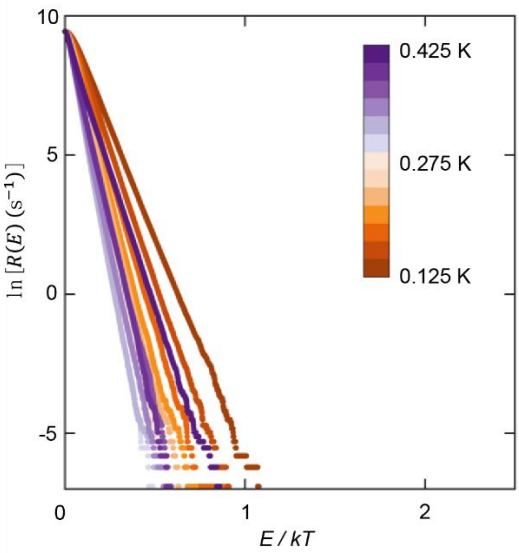

Figure 5.9 $\ln R(E,T)$ versus E/kT between 250 mK < T < 450 mK.

5.5 Temperature Evolution of Dynamical Heterogeneity

To further characterize the zero-field frequency domain noise spectrum, we investigate the complete set of temperature-dependent data. The overall temperature evolution of magnetization noise $S_M(\omega, T)$ is shown in Figure 5.10 together with the empty coil noise (black) with the absence of DTO sample. Fitting the noise spectrum with

$$S_M(\omega, T) \propto \frac{\tau_{GR}(T)}{1+\omega^b \tau_{GR}^b(T)} \tag{5.8}$$

yields the resulting parameters $b(T)$ as shown in Figure 5.11 (iv). The detailed comparison of $b(T)$ with previous literatures is shown in Appendix E. Consistent with previous studies (*39, 46*), $b(T)$ grows gradually with decreasing temperature and saturates towards 1.5 in regime (II) at around 1 K. By lowering the temperature below 1K, the drop in $b(T)$ is observed. In regime (III), the noise power at lower temperature tends to collapse towards 1/*f* noise as $b(T) < 1$, causing Eqn. 5.8 to be no longer a suitable fitting function below 300 mK.

Despite the rapid drop of magnetic noise power, the monopole noise persists with detectable signal even at our lowest measured temperature (Figure 5.10B). It is interesting to consider how many monopoles remain active for $T \to 0$. By evaluating the power of magnetization noise S_M through $\sigma_M^2(T) = \int d\omega \; S_M(\omega, T)$, we estimate the noise fraction as

$$f_{\sigma^2}(T) \approx \frac{\sigma_M^2(T)}{\sigma_M^2(1.5K)} \tag{5.9}$$

The result of the flux variance is illustrated in the bottom panel of Figure 5.11, which shows a vanishing power as it is cooled through the supercooled regime and the variance eventually reaches a steady finite power. In the $T \to 0$ limit, the noise fraction f_{σ^2}

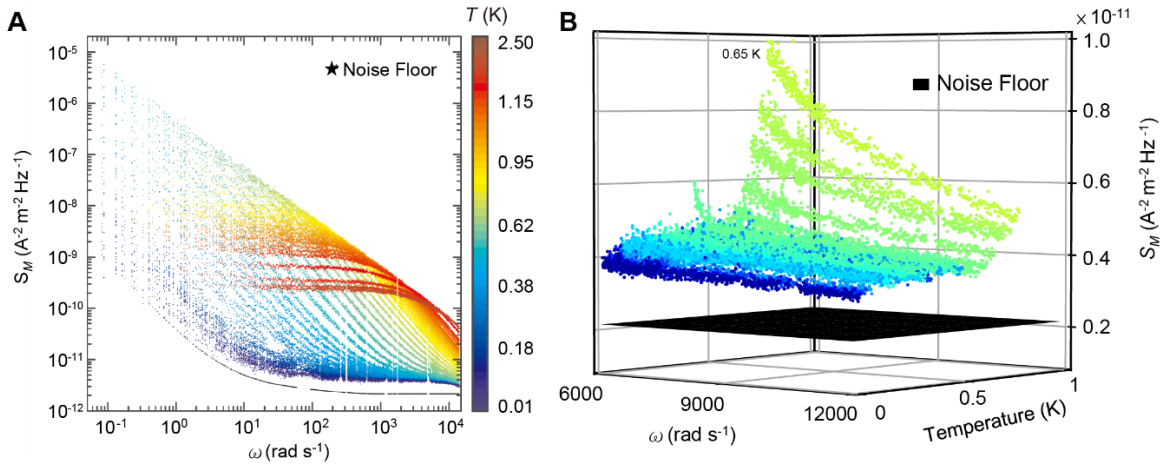

Figure 5.10 (A) Temperature and frequency dependence of DTO magnetization noise $S_M(\omega, T)$ between 10 mK< T < 3000 mK. The black star marks the noise floor without sample. (B) $S_M(\omega, T)$ at high frequency for T < 800 mK. The empty-coil noise floor is plotted as a black surface.

saturates around 10%. Since it is widely accepted that the noise variance scales with the square of the monopole number (i.e. $\sigma^2 \propto N^2$) (*39*), it can be deduced that the monopole density in the low temperature limit is

$$\rho_\phi(T) \approx \rho_N(1.5\text{K})\sqrt{f_{\sigma^2}} \tag{5.10}$$

Using the Debye-Hückel theory with $\rho_N(T) = 2\exp(-\Delta/T)/(1 + 2\exp\left(-\frac{\Delta}{T}\right))$ and $\Delta \approx 4.35$ K for rough estimation of $\rho_N(1.5\text{K})$ yields $\rho_\phi \sim 2\%$ in the low temperature limit. This residual noise even at $T \to 0$ indicates the remaining dynamical spins are perhaps not thermally activated since the spins are considered to be frozen at these temperatures (*20, 89, 92*). Another possible explanation for the magnetic fluctuation could be due to other types of active spins (e. g. impurity spins), not necessarily monopoles. For example, ghost spins are dipoles at the missing spins (Dy vacancies) which could alter the local dipolar interaction and be fluctuating at low temperatures (*93*).

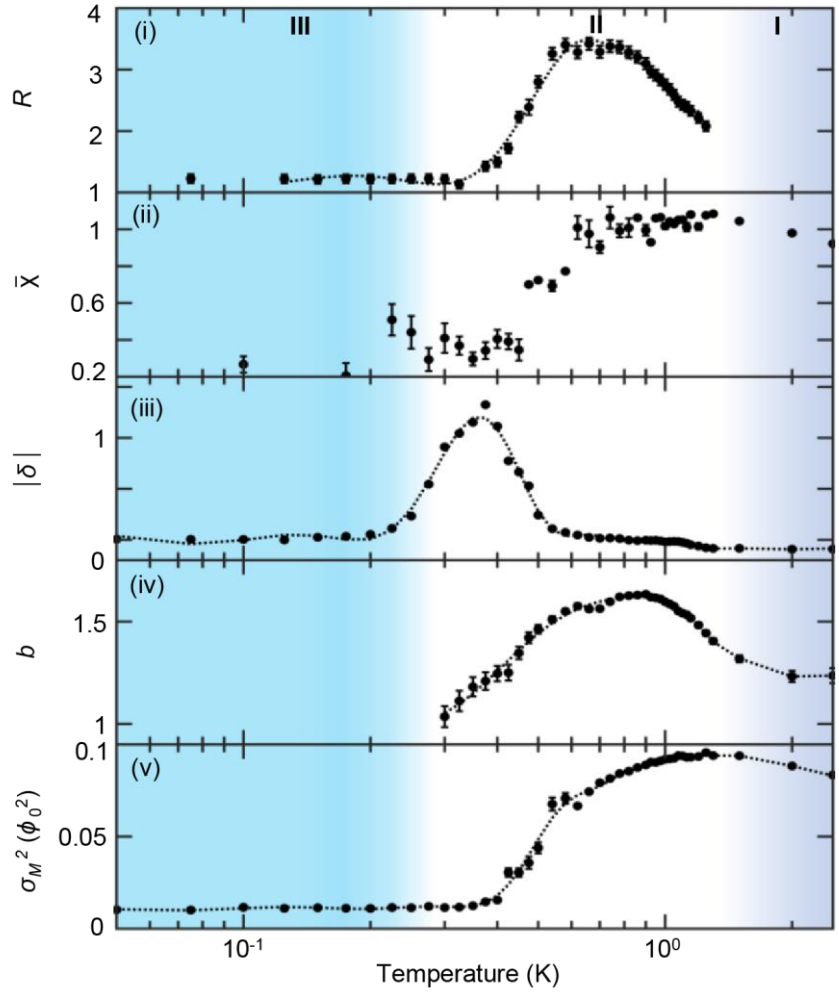

Figure 5.11 Aggregation of noise characteristic of $Dy_2Ti_2O_7$. (i) Ratio of maximal monopole current bursts energy ε_B relative to the average conventional monopole noise energy $\overline{\varepsilon_M}$ ($\mathcal{R} = \max(\varepsilon_B)/\overline{\varepsilon_M}$). (ii) Average of ergodicity function $\overline{X}(T)$ over the measured frequencies. (iii) Slope $|\delta|$ in occurrence rate probability over energy from Figure 5.8A. (iv) Frequency-dependent power law $b(T)$ of magnetization noise by fitting Eqn. 1.15. (v) Variance $\sigma_M^2(T)$ of magnetic monopole noise.

It is useful to compare the phenomenological observation associated with the flux noise statistic in one plot (Figure 5.11) to characterize the emergent dynamical heterogeneity. These include (i) the ratio $\mathcal{R}$ between monopole current burst energy at maximum occurrence rate and average monopole GR noise energy, which is represented

as

$$\mathcal{R} = \max(\varepsilon_B)/\overline{\varepsilon_M} \tag{5.11}$$

(ii) FDT ratio $\overline{X}(T)$ representing a measure of ergodicity by averaging the defined ergodicity function $X(\omega, T)$ over all measured frequencies. (iii) The slope $|\delta|$ of logarithmic monopole current burst probability $\ln P(E, T)$ versus its transition energy E/kT. (iv) Power component of the noise spectrum from Eqn. 1.15. (v) Variance of the time series of flux noise. Notably, throughout the supercooled regime ($T < 1$ K) where the dynamical heterogeneity is in prevalent, the energy ratio $\mathcal{R}$ grows by lowering the temperature from 1 K to 600 mK and collapses when entering the glassy state. A similar trend can be observed for the noise component $b(T)$ where $b(T)$ reaches its maximum at around 1.5. By lowering the temperature below 600 mK, $b(T)$ shifts gradually towards 1. In addition, in regime III we observed a vanishing noise component $b(T)$ when the overall noise spectrum becomes $1/f$ noise and thus the fitting function is no longer valid. As for the temperature dependence ergodicity function $\overline{X}(T)$, $\overline{X}(T)$ starts to deviate from 1 when lowering the temperature below 600 mK, indicating the violation of the FDT relation. The onset of the regime III is marked by temperature when $\overline{X}(T)$ saturates at a lower value around 0.2-0.4.

To summarize, by directly observing the microsecond precision magnetization dynamics $M(t)$ of $Dy_2Ti_2O_7$ across a broad temperature range, we gain a unique perspective on the thermal evolution of magnetic monopole fluids and a clearer understanding of the ground state when approaching zero temperature. Key characteristics are identified including the discovery of dynamical heterogeneity in supercooled monopole fluids from the observation of monopole current bursts, the

transition to the loss of ergodicity, and remaining high-frequency active spins (not necessarily monopoles) even at $T \to 0$. Three distinct regimes of monopole dynamics can now be categorized, as the conventional magnetic quasi-free monopole fluid at $T \gtrsim 1500$ mK, the dynamical heterogeneity regime between 250 mK and 1500 mK with diminished energy barriers and intense monopole current bursts, and a third regime of the loss of ergodicity with a noise spectrum showing saturated noise variance (Figure 5.11(v)). These findings offer a comprehensive empirical understanding of microscopic dynamics of supercooled monopole fluids, which are virtually undetectable in other supercooled liquids.

I would like to mention my contribution of developing noise spectroscopy and susceptibility measurement technique on this work. I have developed the magnetic susceptibility measurement protocol and assisted the measurements. Jahn and Chaia have performed the noise experiments and the data analysis. Sudarshan Sharma and Graeme Luke have grown the sample and provided the sample preparation.

Statement of Authorship for joint/multi-authored papers for PGR thesis

The statement shall describe the candidate's and co-authors' independent research contributions in the thesis publications.

Title of Paper	Discovery of Dynamical Heterogeneity in a Supercooled Magnetic Monopole Fluid
Publication Status	Submitted for Publication
Publication Details	J.Dasini, C.Carroll, C.-C.Hsu, H.Takahashi, J.Murphy, F.Jerzembeck, S.Blundell, G.Luke, J.C.S.Davis, and J.Ward, "Discovery of Dynamical Heterogeneity in a Supercooled Magnetic Monopole Fluid", arXiv:2408.00460 (2024)

Student Confirmation

Student Name:	Chun-Chih Hsu		
Contribution to the Paper	Developed monopole noise spectroscopy technology and carried out experimental measurements		
Signature	Chun-chih Hsu	Date	27/08/24

Supervisor Confirmation

By signing the Statement of Authorship, you are certifying that the candidate made a substantial contribution to the publication, and that the description described above is accurate.

Supervisor name and title: Professor J. C. Séamus Davis		
Supervisor comments Excellent.		
Signature Séamus Davis	Date	28/08/24

Chapter 6 Precise Measurement of Magnetic-Charge of Monopoles in Spin Ice

In Chapter 6, I discuss the last work of this thesis regarding to the measurement of the magnetic charge in the canonical spin ice material. Measuring the charge of emergent quasiparticles in quantum materials has always been a crucial yet challenging topic. For instance, fractional charge has been proposed to explain the fractional quantum Hall effect. However, not until it was directly measured through advanced shot noise experiments did people widely accept the concept of fractional charge (*94*). Although magnetic monopoles in spin ices are not quasiparticles (as monopoles are not quantum coherent), measuring the quantitative value of magnetic charge is still important to validate the monopole theory. Thus, the majority of my PhD has focused on exploring different techniques to measure the magnetic charge in spin ices precisely. At last, the most promising method is through the balance between the magnetic Coulomb force and the entropic force. By using the monopole current spectrometer, the flux equilibrium caused by self-magnetization under an applied field is examined carefully. It is described that such flux equilibrium is purely related to the magnetic charge and other experimentally controllable parameters (*15*). Thus, the magnetic charge is derived as a function of temperature and magnetic field. Eventually, in the end of the chapter, I will show the measured magnetic charge in high precision, which is consistent with the theoretical value with around 2% difference.

6.1 Measuring Magnetic Charge with Entropic Force

As introduced in Chapter 2, the equation of motion for the non-interacting magnetic monopoles is derived under an application of magnetic field (Eqn. 2.8). That is, under an external field application, the monopole dynamics are governed by the internal entropic force and the magnetic field. From Eqn.2.8 ($j_m + D\nabla\rho = \sigma_m(\mu_o H - \frac{\Sigma\Omega}{m^2})$), by assuming that in the low field scenario the monopole density is basically homogenous ($\nabla\rho \sim 0$), the monopole dynamics can be simplified as

$$j_m = \sigma_m \left[\mu_0 H - \frac{\Sigma\Omega}{m^2}\right] \tag{6.1}$$

Since $j_m = \frac{dM}{dt}$ and $\Omega = M$, the equation becomes a first order differential equation $\frac{dM}{dt} = \sigma_m \left[\mu_0 H - \frac{\Sigma M}{m^2}\right]$. Therfore, the transient of magnetization under an application of magnetic field is

$$M(t) = -\frac{m^2\mu_0 H}{\Sigma} e^{-\frac{\sigma\Sigma}{m^2}t} + \frac{m^2\mu_0 H}{\Sigma} \tag{6.2}$$

One can immediately notice that $M(t)$ converges to $m^2\mu_0 H/\Sigma$ and most surprisingly that the quantitative value of magnetic charge m can be obtained from the ratio of the magnetization at equilibrium to the applied field with a coefficient containing all measurable parameters. Experimentally, the equilibrium state has great utility and can be measured with the monopole current spectrometer. Initially, at the zero field, monopoles are bundled with the Dirac strings. Under the magnetic field application, the end state is reached when monopole current stops and the monopole pairs are interconnected as always through the Dirac strings (Figure 6.1A). In this picture, it is clear that a reduction of entropy is caused by the self-magnetization (*30, 31*) where the reduced entropy can be expressed by Eqn. 2.3 (Figure 6.1B). In this scenario, Φ_s threading through the

superconductive loop is produced from the penetrating Dirac strings. The flux from the sample is thus given by

$$\Phi_S(\infty, T, H) = \mu_0 \overrightarrow{A_s} \cdot \vec{M}(\infty, T, H) \tag{6.3}$$

where A_s is the cross sectional area of the spin ice sample. Hence, by substituting M in terms of the applied field and the temperature, the equation can be converted to

$$\Phi_S(T, H) = m^2 \frac{\sqrt{3}}{16} \frac{A_s {\mu_0}^2}{a_d k_B} \frac{H}{T} \tag{6.4}$$

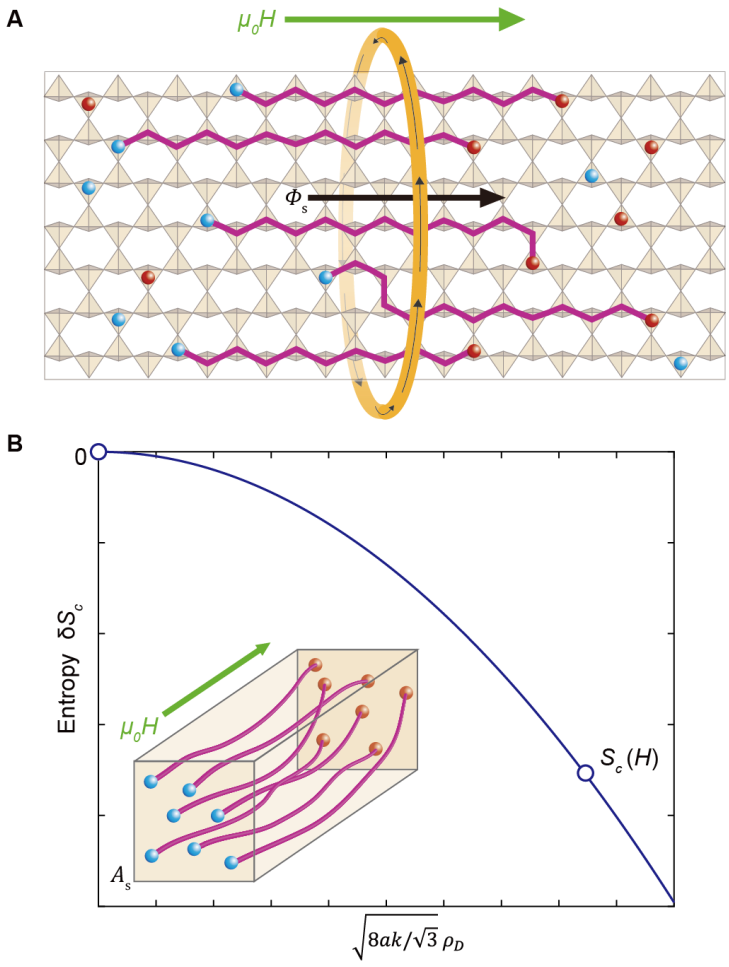

Figure 6.1 (A) Schematic illustration of monopole configuration reaching equilibrium under applied field and the monopole current stops. The flux is due to the Dirac string threading the superconducting loop. (B) Representation of reduced of entropy due to external field. ρ_D denotes the Dirac string density.

Based on this equation, we propose a precise measurement of magnetic charge by measuring flux with controlled magnetic field and temperature. In that case,

$$m(T,H) = \sqrt{\frac{16a_d k_B}{\sqrt{3}A_s\mu_0^2}\left(\frac{T}{H}\right)\Phi_S(T,H)} \tag{6.5}$$

Therefore, by recording $\Phi_S(T,H)$, the precise measurement for magnetic charge and its temperature and magnetic field dependence becomes possible. Now, since Φ_S is the intrinsic flux generated by sample and its geometry, we should also consider experimental parameters from the pickup coil. Furthermore, the SQUID outputs voltage signal that is proportional to the flux ($\Phi_S = V_S/\alpha\gamma$). By taking these into account, Eqn. 6.5 becomes

$$m(T,H) = \sqrt{\frac{16a_d k_B}{\sqrt{3}\alpha\gamma A_s\mu_0^2}\left(\frac{T}{H}\right)V_S(T,H)} \tag{6.6}$$

where the parameters are SQUID transfer coefficient γ, and pickup coil coupling constant α (Detailed explanation in Appendix A). In this work, these parameters (γ, α) can be calibrated together through a superconducting sample, while the sample cross sectional area A_s is measured separately by optical microscopy.

6.2 ANDROMEDA II

In this experiment, the spectrometer is mounted on a cryo-free 3He fridge for a broader temperature range. The main structure of the SQUID spectrometer is the same as the spectrometer described in previous chapters and in Appendix A. The major modification of the SQUID spectrometer is that the pickup coil is wound on a macor holder with 9 turns, which is attached to a sapphire rod for direct and efficient thermalization. To ensure an accurate and precise thermalization of the sample, the sample is glued with GE varnish inside the sample holder, and the Cernox thermometer is mounted 20 mm away from the sapphire rod. Typically, the error for the temperature is

less than 0.5%. In addition, Star SQUID is used for wider frequency bandwidth, for up to 10 kHz. The overall geometry and the dimension are illustrated in Figure 3.7. The drive coil are the same for the work in Chapter 4 and this Chapter.

6.3 Sample geometry and Calibration

In order to measure the magnetic charge precisely through Eqn. 6.6, a delicate calibration must be done to avoid the overwhelming systematic error and to increase accuracy. Notably, in Eqn 6.6, three factors ($\gamma, \alpha,$ and A_s) could lead to systematic error (see Appendix A). The first is the transfer function γ, which is calibrated accurately to be 0.099 V/φ_0 for the Star SQUID. Secondly, the coupling constant α is calibrated by measuring a superconductor (Nb) in its Meissner state. That is, by applying a DC field to the Nb encapsulated in the pickup coil, the flux Φ_D^{Nb} generated by the niobium is

$$\Phi_D^{Nb} = \alpha\Phi_{Nb} + \Phi_D^E = -\alpha A_{Nb}\mu_0 H + \alpha A_I \mu_0 H \tag{6.7}$$

where A_{Nb} is the cross sectional area of the Nb sample and is measured to be $1.05\ \text{mm}^2 \pm 1.9\%$ by the optical microscope (Figure 6.2). A_I accounts for the residue of the external field caused by the imbalance of the two counter-wound coils and can be measured with the absence of sample under an application of magnetic field. In this scenario, the flux detected by SQUID is given by

$$\Phi_D^E = \alpha A_I \mu_0 H \tag{6.8}$$

Therefore, α can be derived through the subtraction Φ_D^{Nb}-Φ_D^E. The DC field sweep result for Nb is shown as Figure 6.4 and the coupling constant α is calibrated to be $6.88 \pm 0.04 \times 10^{-3}$. Thus, the imbalance A_I is calculated to be $A_I = 5.53 \pm 0.03 \times 10^{-8}$ [m^2]. Lastly, the sample cross section area A_s is measured separately with an optical

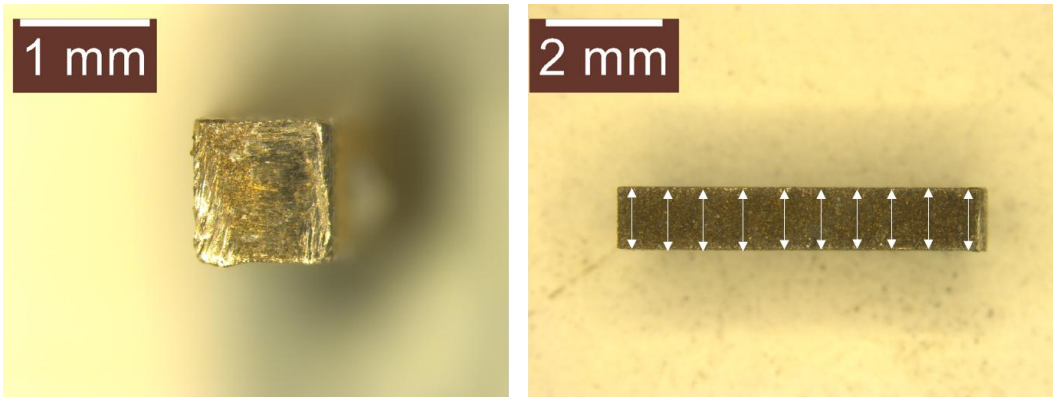

Figure 6.2 Left: cross-section view of the Nb with $A_s = 1.05\ \text{mm}^2$. Right: side view of the Nb for error estimation which marks 10 line cuts with standard deviation of 0.012 mm.

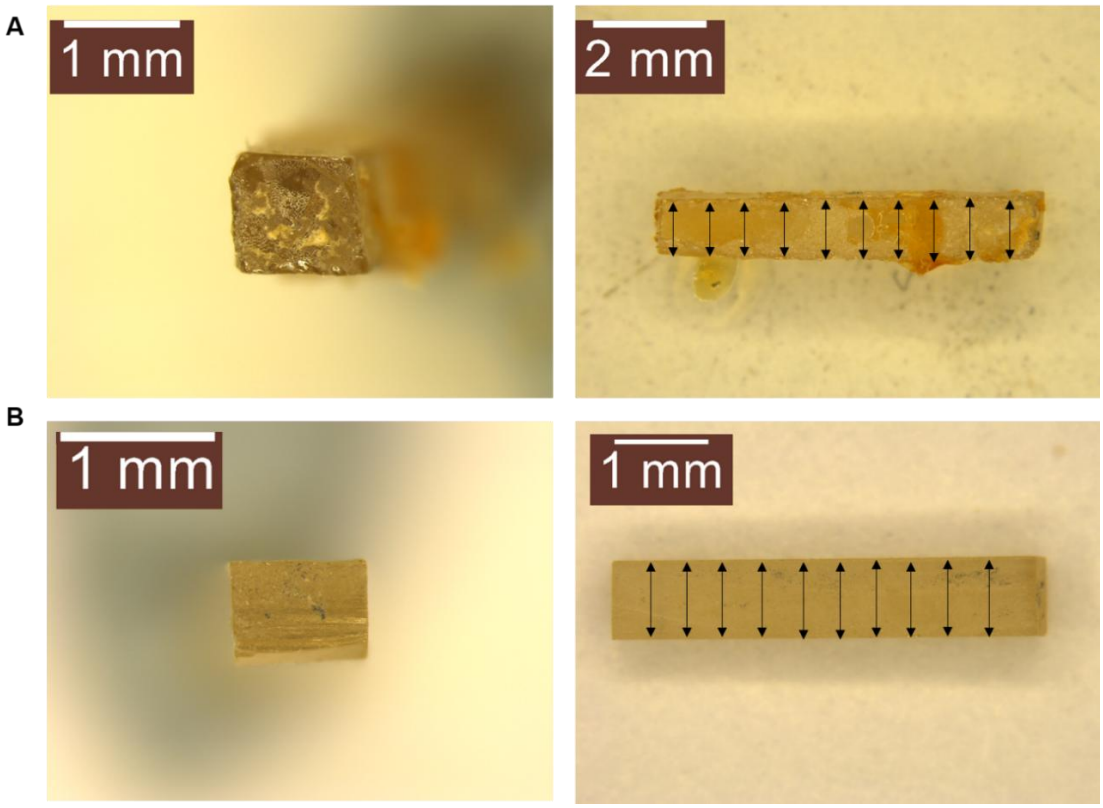

Figure 6.3 Left: Cross-section view of the DTO sample for the study. $A_s = 1.06\ \text{mm}^2$. Right: Side view of the DTO sample for error estimation of the area. The black arrow marks the 10 line cuts with standard deviation of 0.025 mm.

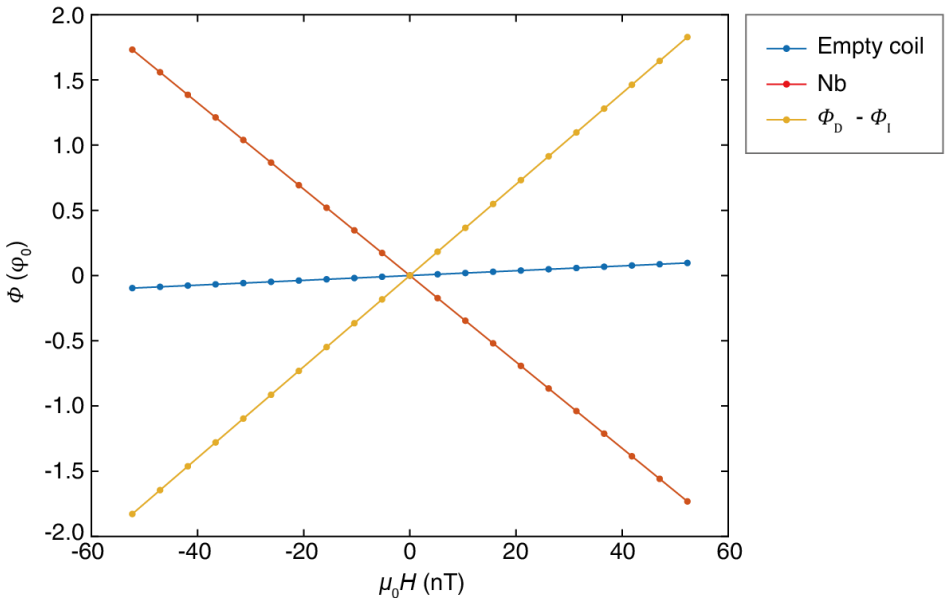

Figure 6.4 The measured flux under the DC magnetic field sweep for empty coil (blue), Nb (red), and their subtraction (yellow). The fit of Φ_D^{Nb}-Φ_D^E yields the coupling constant $\alpha = 6.88 \pm 0.04 \times 10^{-3}$.

microscope (see Figure 6.3). The cross sectional area A_s of the DTO is measured 1.06 ± 0.012 mm^2, and the error in the sample area is estimated from the width change on the side view, with length of 1.110 ± 0.010 mm and 0.957 ± 0.007 mm for the square cross-section.

6.4 Temperature and Field Dependence of Flux Equilibrium

The precisely calibrated experimental parameters validate further flux measurements for the spin ice material DTO. To explore the magnetic dynamics and the equilibrium fluxes described by Eqn 6.2 and 6.3, step-wise magnetic fields in both positive and negative field directions is applied to the DTO mounted into the spectrometer. The measurement was performed by exciting the magnetic state for over 200 sequences.

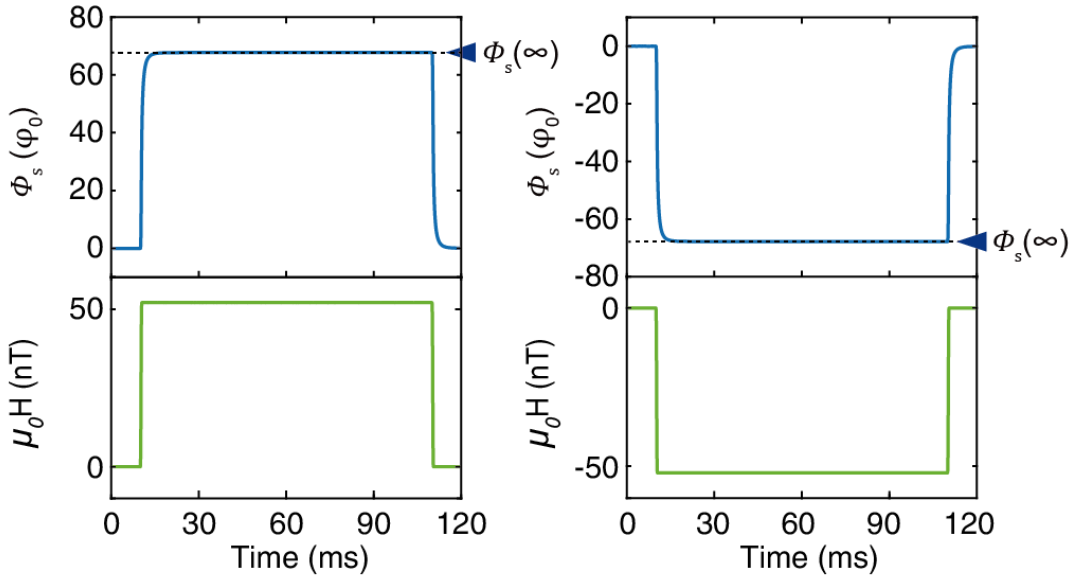

Figure 6.5 Typical example of monopole current control with the step-wise magnetic field in positive (left) and negative (right) field direction. The blue arrow marks the flux at equilibrium $\Phi_S(\infty)$.

To ensure that DTO reaches equilibrium flux, each sequence of the magnetic field stays at a constant for more than 80 ms. As described in Chapter 3 and 4, the recording is further averaged for all the sequences. Figure 6.5 shows the demonstration of the applied field and the flux response. As expected, the positive field and the negative field show symmetric results.

By performing the measurement protocol at varying magnetic fields and temperatures, we therefore record a matrix of $\Phi_S(\infty, T, H)$. Figure 6.6A shows the temperature sweep of $\Phi_S(t, T, H)$ and the flux equilibrium $\Phi_S(\infty, T, H)$ at a fixed magnetic field at B = 52.5 nT, while Figure 6.6B, on the other hand, shows the magnetic field sweep at the fixed temperature T = 2.2 K. In combination, the complete matrix containing all the measured temperatures and magnetic fields is illustrated in Figure 6.7

as a 2D colormap. Clearly, the flux at equilibrium quantitatively evolves over two orders of magnitude across the experimental parameter space, with T up to 6 K and B over 200 nT.

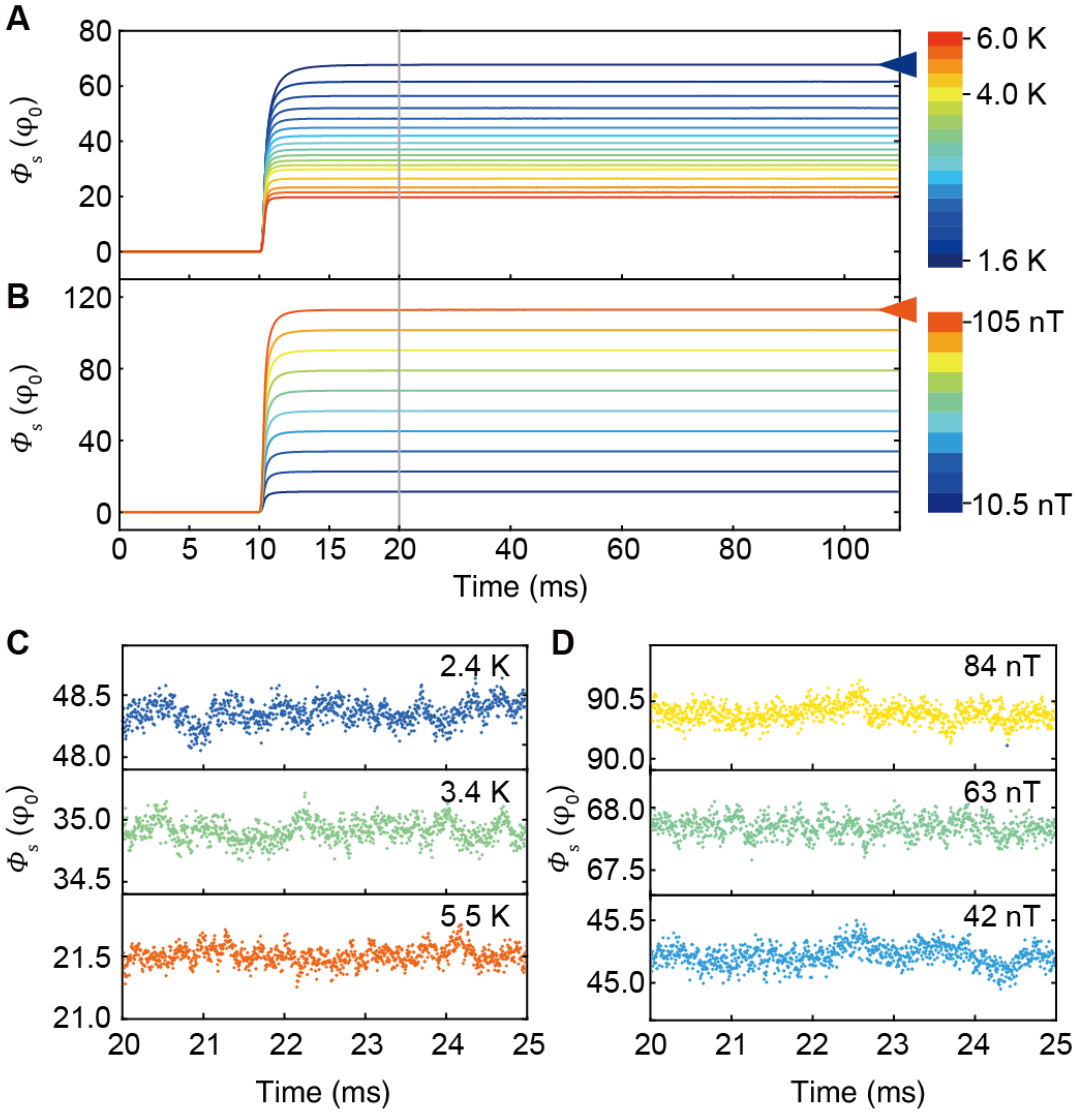

Figure 6.6 (A) The temperature dependence of averaged $\Phi_S(t,T,H)$ at $B = 54$ nT (B) The magnetic field dependence of averaged $\Phi_S(t,T,H)$ at $T = 2.2$ K. (C) and (D) Typical high resolution examples of measured $\Phi_S(t,T,H)$ versus t from (A) and (B).

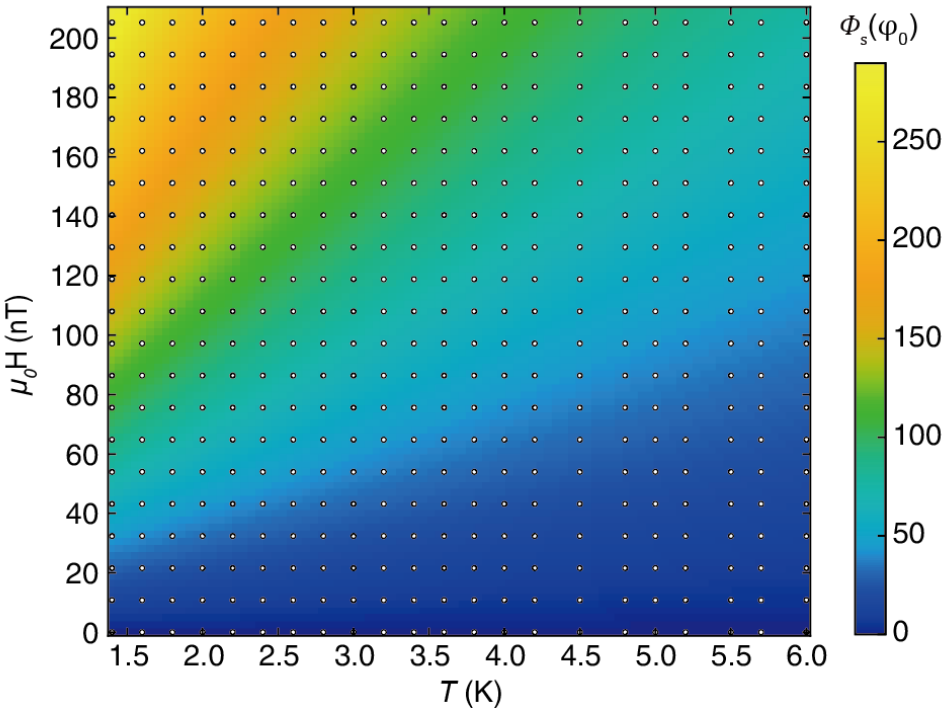

Figure 6.7 2D colormap of all measured $\Phi_S(\infty, T, H)$ ranging over almost two orders of magnitude in the experimental window. The measured points are marked by white dots.

6.5 Magnetic Charge Measurement

To investigate Eqn. 6.6, the complete matrix of flux equilibrium at varying magnetic fields and temperatures is collected. Now the magnetic charge can be acquired by collapsing all the data points in a single plot. Figure 6.8 plots the $\Phi_S(\infty, T, H)$ in both magnetic field directions versus $\frac{\sqrt{3}}{16}\frac{A_S{\mu_0}^2}{a_d k_B}\frac{H}{T}$. Amazingly, despite ranging over two orders of magnitude, the overall $\Phi_S(\infty, T, H)$ follows merely a simple linear dependence in $\frac{H}{T}$. Furthermore, the slope of Figure 6.8 is m^2, and by performing a linear fit, the slope is estimated to be 1.897×10^{-13} $\mathrm{A^2m^2}$ and 1.899×10^{-13} $\mathrm{A^2m^2}$ for positive and negative field, leading to a direct measurement of magnetic charge as

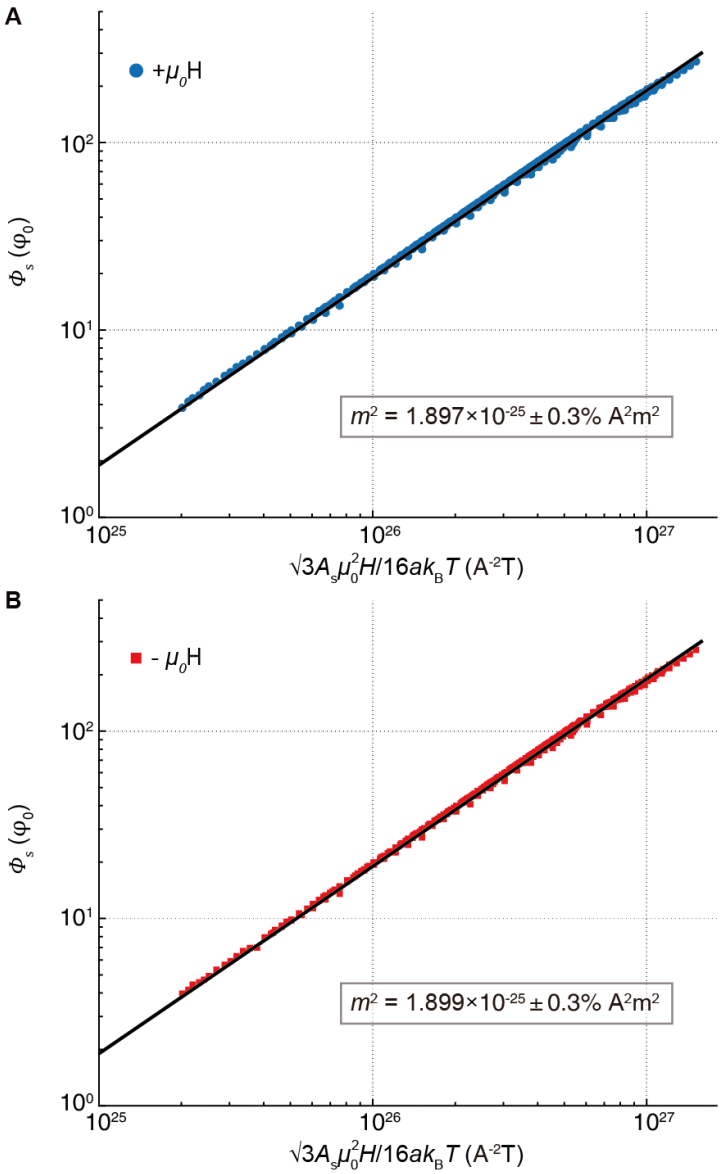

Figure 6.8 Simultaneous plot of all of measured $\Phi_S(\infty, T, H)$, versus $\frac{\sqrt{3}}{16}\frac{{A_S\mu_0}^2}{a_d k_B}\frac{H}{T}$. The fitted line is plotted in black with a slope of m^2 for (A) positive and (B) negative field.

$$m = 4.36 \times 10^{-13} \pm 0.25\% \text{ [Am]} \tag{6.9}$$

which is extremely close to the theoretical value ($m = 4.24 \times 10^{-13}$ Am) as proposed in Ref. (*14, 15*) (see Appendix F). This result directly corroborates the validity of the monopole picture to describe the magnetic state of spin ice materials. It is also noticeable

that once the temperature drops below 1.4 K, the measured charge deviates more from a constant (see Appendix F). The observation is consistent with the finding of emergence of dynamical heterogeneity where the spin ice no longer behaves like a free monopole fluid. How the complex monopole dynamics at low temperatures could affect the deviation requires more theoretical and experimental works. We leave this investigation as potential works in the future.

In summary, in this work we demonstrate the monopole current spectrometer as a precise tool to measure magnetic monopole charge. By using simultaneous control of monopole current and high-speed data logging, high precision quantitative monopole charge measurement is achieved, and the charge is measured to be $m = 4.36 \times 10^{-13}$ Am. The excellent agreement between the measured charge and the theory validates the monopole picture as a good description of spin ices. The match between theory and experiment also marks the importance of entropic force in the monopole transport theory in spin ice where the monopole motion has halted in equilibrium state. It is noticeable that although there are plenty of theoretical (*95, 96*) and experimental (*9, 92, 97*) works on temperature dependence DC susceptibility, very few studies compare the theory and the measurement quantitatively. This work provides a high precision quantitative measurement of temperature dependence DC susceptibility, and the comparison between theory and the measurement below 1.4 K could be interesting work in the future.

Chapter 7 Outlook

We have demonstrated that the monopole current/noise spectrometer is a powerful tool for investigating the intrinsic magnetic dynamics of the spin ice material $Dy_2Ti_2O_7$. This conclusion is supported by three distinct studies. Firstly, by analyzing the time-dependent current and noise under simultaneous application of magnetic field, we discovered that the magnetic dynamics exhibit dichotomous behavior, characterized by two distinct relaxation rates, indicative of two separate spin flip processes. Secondly, our investigation into the statistics of magnetic noise revealed significant dynamical heterogeneity below 1 K, and we identified a violation of the fluctuation-dissipation theorem at temperatures below 300 mK. Lastly, by recording the equilibrium of magnetic flux under step-wise magnetic field and its temperature and field dependence, we were able to calculate the magnetic charge, providing a direct measurement of the fundamental charge in spin ice.

These findings underscore the effectiveness of the monopole current/noise spectrometer in capturing and characterizing complex magnetic behaviors in spin ice materials. Looking forward, further refinement and application of this spectrometer could yield deeper insights into low-temperature magnetic phenomena and contribute to the development of new theoretical models. Future research may focus on exploring other spin ice materials and extending measurements to higher magnetic fields where the ground state manifold changes significantly. This could potentially alter the scenario of a free monopole fluid as the ground state and deepen our understanding of magnetic dynamics in frustrated systems.

Expanding the application of the monopole current/noise spectrometer to other materials where monopoles are predicted, such as iridate systems, presents an exciting future direction. Due to different strengths of magnetic dipoles, a completely distinct relaxation time and magnetic dynamics may arise. Furthermore, how quantum effects could affect the monopole picture remains elusive in quantum spin ice systems. Investigating these systems could reveal novel quantum phenomena and deepen our understanding of monopole dynamics. Last but not least, demonstrating shot noise from individual monopole excitations could provide further insights into the fundamental properties of these exotic particles. Combining the spectrometer with a scanning probe technique could enable spatial measurements, allowing for the visualization of dynamical heterogeneity at the nanoscale. This integration would offer a powerful approach to study spatially resolved magnetic dynamics, opening new avenues for research in condensed matter physics.

Appendix A Calibration

In this Appendix, I explain the calibration that has been performed on the SQUID-based monopole current/noise spectrometer. The calibration is crucially important for the quantitative description to the magnetization measurement and the magnetic field detected by the SQUID. This appendix first describes the parameters involved in the pickup coil and SQUID circuitry, which relates the measured voltage to the flux threading through the pickup coil. Later, the performance of noise spectroscopy with empty coil and its voltage response under DC/AC field is discussed. The intrinsic SQUID calibration and the noise performance are mostly based the work done by Ritika Dusad and Hiroto Takahashi. I extend the calibration method to applying DC/AC magnetic field. By bringing all the calibration method here, I hope this appendix can be a useful reference for any SQUID-based spectrometer in the future.

A.1 Coupling of Pickup Coil and SQUID

First, we start from the transfer function γ as SQUID operates by converting the sensed magnetic flux into voltage signal. The transfer function γ links the SQUID voltage output V_S and the flux at the SQUID Φ_S by

$$V_S(t) = \gamma \Phi_S(t) \tag{A.1}$$

The transfer function γ can be simply calibrated by measuring the signal out at the Tube mode of the QD SQUID. The reset of the SQUID will shift the voltage by V_Φ and transfer function thus calibrated as V_Φ per flux quanta φ_0. For the QD SQUID, the transfer function is 0.748 V/φ_0 at range 5.

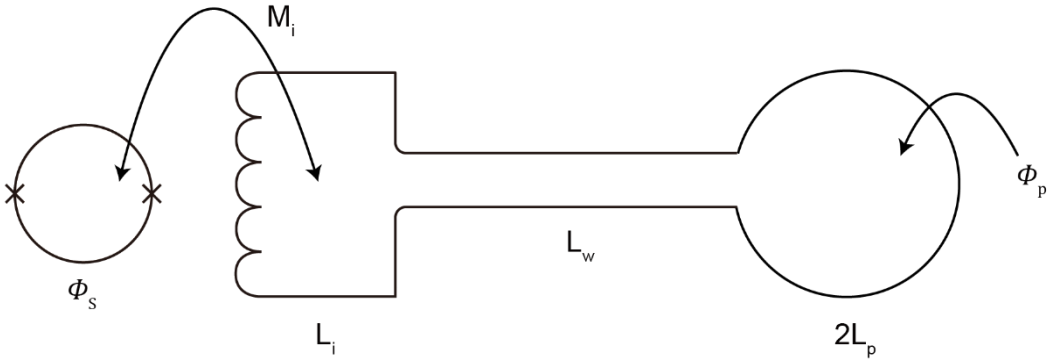

Figure A.1 Schematic illustration of a SQUID detection circuit and the related parameters. Note that inductance L_{w} for the wire is normally negligible, especially for twisted pair.

In SQUID-based spectrometer, a pickup is designed to integrate with the SQUID to detect the magnetic flux (see Figure 3.1 and Figure A.1). From the circuitry, the flux Φ_{S} that SQUID senses and the applied flux Φ_{p} are linked to each other by

$$\Phi_{\mathrm{S}}(t) = \alpha\Phi_{\mathrm{p}}(t) \tag{A.2}$$

where α is the coupling constant of the pickup coil to SQUID. α can be derived explicitly from a supercurrent I_{p} generated by the applied flux Φ_{p} such that

$$I_{\mathrm{P}} = \Phi_{\mathrm{p}}/(2L_{\mathrm{p}} + L_{\mathrm{i}}) \tag{A.3}$$

where L_{i} is the intrinsic SQUID inductance and $2L_{\mathrm{p}}$ is the total inductance of the pickup coil. (Since the pickup coil is made up of two opposite chirality coils, the total inductance is simplified to $2L_{\mathrm{p}}$ where L_{p} represents the inductance for one chirality coil). Thus, this yields the flux at the SQUID as

$$\Phi_{\mathrm{S}} = M_{\mathrm{i}}I_{\mathrm{P}} = M_{\mathrm{i}}\Phi_{\mathrm{p}}/(2L_{\mathrm{p}} + L_{\mathrm{i}}) \tag{A.4}$$

where M_i is the mutual inductance between SQUID and the pickup coil. The coupling constant is thus given by

$$\alpha = \frac{M_{\mathrm{i}}}{2L_{\mathrm{p}}+L_{\mathrm{i}}} \tag{A.5}$$

As reported by the manufacturer (Quantum Design), $M_{\mathrm{i}} \approx 9.84 \times 10^{-3}$ μH and $L_{\mathrm{i}} \approx 1.82$ μH. The total inductance $2L_{\mathrm{p}}$ is 1.7 μH measured by the LCR meter at room temperature ($L_{\mathrm{s}} - R_{\mathrm{dc}}$ mode at 500 kHz). The measured parameters yield $\alpha \sim 2.8 \times 10^{-3}$.

A.2 Background Noise Performance

For SQUID-based noise spectroscopy to work, it is essential to have low intrinsic SQUID noise and environmental flux noise. For ANDROMEDA, the noise background has been examined before inserting the DTO sample. Figure A.2A shows the intrinsic SQUID noise measured at 4 K and zero field with the SQUID pad open. Clearly, the overall flux noise is below 4×10^{-11} φ_0^2/Hz. Figure A.2B shows the flux noise of the SQUID and spectrometer apparatus without DTO sample at 4 K. The primary coil circuit is open. The overall flux noise has similar spectral shape with the intrinsic SQUID flux noise but with several peaks around 100 Hz and 1 kHz. This is potentially from the environmental magnetic field coupled with the vibrational mode of the pickup coil holder assembly. The spectrometer with Nb-shielded pickup coil has flux noise below 10^{-10} φ_0^2/Hz for the measured frequency and thus has high SNR to measure the monopole noise of the DTO.

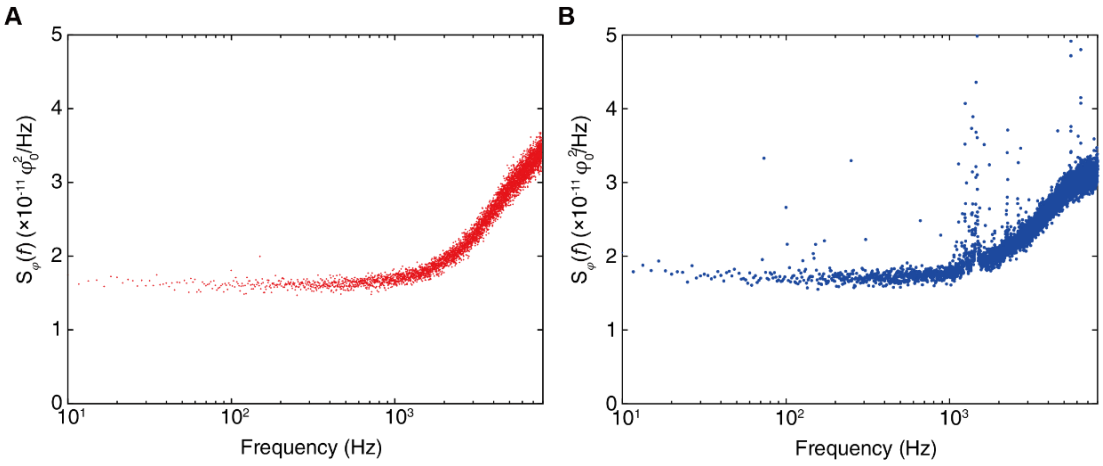

Figure A.2 (A) Intrinsic flux noise of the SQUID electronics with the pad open circuit at 4 K. (B) Noise performance of pickup coil under zero field at T = 4 K. The noise level is below 10^{-10} φ_0^2/Hz for the measured frequency.

A.3 DC Field Calibration

To measure the magnetization from the sample quantitatively, DC field calibration is essential to determine the imbalance of counter-wound pickup coil and the filling factor of a sample. The prerequisite of DC field calibration is to produce a known magnetic field quantitatively. The primary coil of ANDROMEDA contains 537 turns in 9 cm. Hence, the magnetic field can be estimated precisely from the finite size solenoid with a coil density $n_{\mathrm{coil}} = 5967\ \mathrm{m}^{-1}$

$$B_{\mathrm{coil}}/I = \mu_0 n_{\mathrm{coil}} \times \frac{L/2}{\sqrt{r^2+(L/2)^2}} = 7.22\ \mathrm{mT/A} \tag{A.6}$$

where L and r are the length and the radius of the drive coil ($L = 90$ mm and $r = 12.57$ mm). However, since the whole primary coil is surrounded by the outer Nb shield (see Figure 3.5-3.7), a counter magnetic field generated by the inner surface current of superconducting shield will compensate part of the field. Since the superconducting cylinder maintains the flux within the inner diameter to be unchanged, the residual of the

magnetic field can be estimated from the ratio of cross section area of primary coil and the Nb shield. The magnetic field after the correction can be expressed as

$$\frac{B_{\mathrm{ex}}}{I} = \frac{B_{\mathrm{coil}}}{I} \times \frac{A_{\mathrm{shield}} - A_{\mathrm{coil}}}{A_{\mathrm{shield}}} \tag{A.7}$$

where A_{shield} is the inner cross-section area of the Nb cylinder and A_{coil} is the cross-section area of the drive coil. Based on the geometry described in Chapter 3.2.2, $A_{\mathrm{shield}} = 1801\ \mathrm{mm}^2$ and $A_{\mathrm{coil}} = 496.9\ \mathrm{mm}^2$. These yield a magnetic field of

$$\frac{B_{\mathrm{ex}}}{I} = 5.25\ \mathrm{mT/A} \tag{A.8}$$

Now from the known magnetic field, the imbalance of the pickup coil can thus be calibrated. It is not surprising that two opposite chirality coils do not compensate the flux from the external field completely. The strength of the residual flux affects the SNR for the time-domain flux and frequency-domain susceptibility measurement. Especially for the AC susceptibility measurement, the remaining signal from coil itself may overwhelm the signal from the sample at extremely low and high frequency where the imaginary part of the susceptibility is normally small. In this scenario, the flux from the coil appears constant in frequency-domain susceptibility measurement and thus obscures the target signal, particularly for the loss angle. To calibrate, a DC sweep with different strength of magnetic field is implemented. The imbalance A_{Im} can be simply calculated from

$$V_{\mathrm{SQ}} = \alpha\gamma B_{\mathrm{ex}} A_{\mathrm{Im}} \tag{A.9}$$

For a primary coil driven by a voltage source, the SQUID voltage output can be further expressed as

$$V_{\mathrm{SQ}} = \alpha\gamma A_{\mathrm{Im}} \frac{V_{\mathrm{in}}}{R} \tag{A.10}$$

Figure A.3A shows the DC sweep result of the astatic coil. By fitting to Eqn. A.10, the imbalance of the pickup coil can be derived, which has an effective area about $A_{\mathrm{Im}} =$

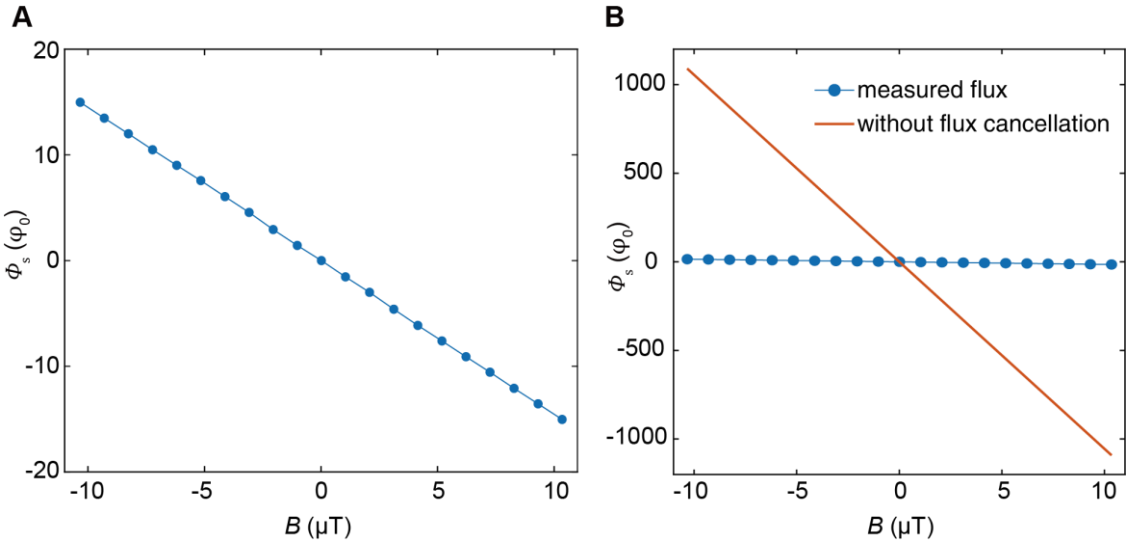

Figure A.3 Performance of the flux compensation of pickup coil. (A) The remaining flux Φ_S after the cancellation of external field which is measured with empty coil (without sample) at 4 K (B) The measured flux compared with the expected flux response if there is no compensation pickup coil (red line). Only 1.3% of the residue flux is detected when the external field is applied.

1.09 mm^2. By considering the pickup coil as 10 turns of coil with radius = 1.576 mm, the cross-section area A_p is around 78 mm^2, which leaves an imbalance of 1.396%. This can also be seen from Figure A.3B, which plots the measured flux in comparison with the expectation of response without any compensation.

The final factor to be calibrated is the filling factor of the sample, which can be done by measuring a test sample with the same sample geometry and with a known value of magnetic susceptibility. Typically, a type-I superconductor indium is used for the filling factor calibration due to its flexibility. Thanks to the Meissner effect, superconductors have huge magnetic susceptibility of -1. Therefore, by putting an indium inside the pickup coil the SQUID voltage becomes

$$V_{\mathrm{SQ}} = \alpha\gamma(A_{\mathrm{Im}}B_{\mathrm{ex}} \pm FA_{\mathrm{p}}B_{\mathrm{ex}}) \tag{A.11}$$

when indium is superconducting below T_{c}. Since all other factors are calibrated, the filling factor F can be estimated precisely. For the work in Chapter 4, the filling factor is estimated to be around 28%.

A.4 AC Field Calibration

AC field calibration is crucial for any dynamical measurements of the SQUID spectrometer. Since the dynamical measurements such as time domain transient measurement focus on the process of the transition between two states, the calibration cannot be done with the DC method. Experimentally, the frequency response of the spectrometer is affected by numerous factors including intrinsic SQUID bandwidth (set by internal lock-in), pickup coil bandwidth (LC circuit) and the environmental setup. Especially, the pickup coil can be extremely sensitive to the environmental source which is easily overlooked, resulting in a complex frequency response. For a successful frequency domain SQUID measurement, it is essential to confirm the flatness of the frequency response of spectrometer without sample.

For ANDROMEDA, the AC field calibration is carried out by performing a lock-in measurement with a frequency sweep at a fixed field. The circuitry is illustrated in Figure 3.11B. The frequency sweep results for the empty coil are shown in Figure A.4. Figure A.4A shows the effective gain $G(f)$ of the SQUID circuitry defined as

$$V_{\mathrm{SQ}}(f) = G(f)\alpha\gamma B_{\mathrm{ex}}(f)A_{\mathrm{Im}} \tag{A.12}$$

At low frequency, it is clear that the response is flat and thus showing $G(f) = 1$. Notably,

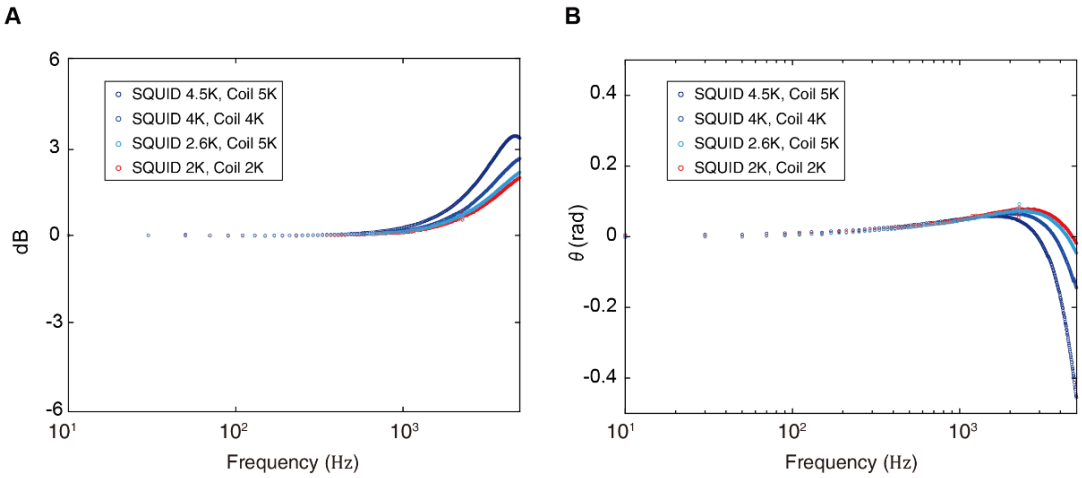

Figure A.4 Frequency response of empty coil. (A) Effective gain of the frequency response of the pickup coil. (B) The phase response of the pickup coil.

the frequency response is highly temperature dependent with the SQUID temperature changing the overall performance significantly. However, when the SQUID is held below 2.5 K, the pickup coil temperature does not change the frequency response. This may be due to the temperature dependence of the critical current of the SQUID (*98*). Therefore, experimentally, frequency domain experiments are always performed with SQUID temperature maintained the same. Overall, the 3dB bandwidth for the spectrometer is around 5 kHz. Between 5-10 kHz, the signal is still detectable yet a varying gain needs to be taken into consideration. Figure A.4B shows the phase result for the frequency sweep of the empty coil when the external reference is set to be zero phase. In general, the effective gain $G(f)$ can be expressed as a complex form with

$$G(f) = G_0(f)e^{i\theta(f)} \tag{A.13}$$

Similarly, at low frequency, $\theta(f)$ maintains flat especially below 1 kHz but with a non-zero value. This finite phase about 0.74 degree is perhaps due to the minute delay of the overall electronics and circuitry. By setting the phase of 0.74 degree as zero phase, the

phase is calibrated for the frequency domain measurement.

I believe it is equally important to mention how the environment of the spectrometer can change the frequency response. One of the most common sources is the ferromagnet at low temperature and eddy current from metallic materials (*99*). Intuitively, the design of cryostat and the machinery parts for the spectrometer would avoid ferromagnetic materials and thus the former is normally not the cause. The latter can sometimes be problematic as the presence of a normal metal in the vicinity of the pickup coil will induce frequency dependent magnetic fields. The total field B_T acting on the pickup coil is expressed as

$$B_T = \left(1 + \kappa \frac{\omega^2}{\omega^2 + \omega_E^2}\right) B + \kappa \frac{\omega_E}{\omega^2 + \omega_E^2} \dot{B} \tag{A.14}$$

where κ is the coupling of the field to the coil, and ω_E is the time constant determined by modeling the normal metal as a R-L circuit (see Eqn. 7.39 from ref. (*99*)). Therefore, the amount of normal metal near the pickup coil needs to be reduced as much as possible.

Appendix B Monopole Complex Conductivity Table

This Appendix provides a supplementary figure and table, presenting the quantitative value of monopole conductivity converted from the measured monopole current (Figure 4.12). In Chapter 4, the monopole current was measured with the lock-in technique. To acquire the complex conductivity σ_m, the measured monopole current J is normalized with the sample area A_S and the applied field B. That is,

$$\sigma_m = J/A_S B \tag{B.1}$$

Figure B.1 shows the measured in-phase conductivity and out-of-phase conductivity derived from the monopole current. As a reference, Table B.1 provides the quantitative value of the frequency-dependent conductivity at 2 K.

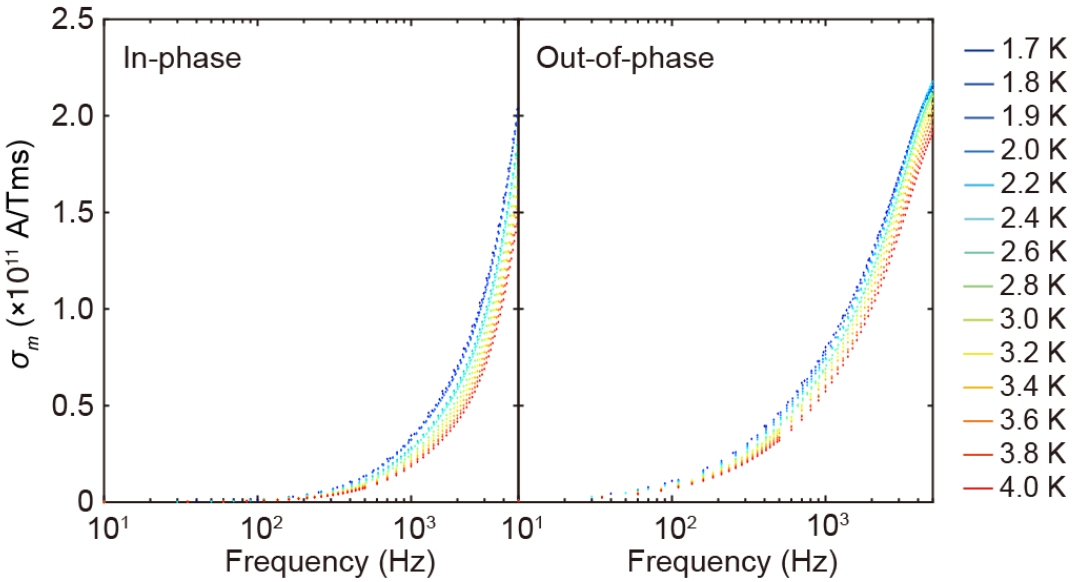

Figure B.1 The measured in-phase and out-of-phase conductivity, $Re\sigma_m$ and $Im\sigma_m$.

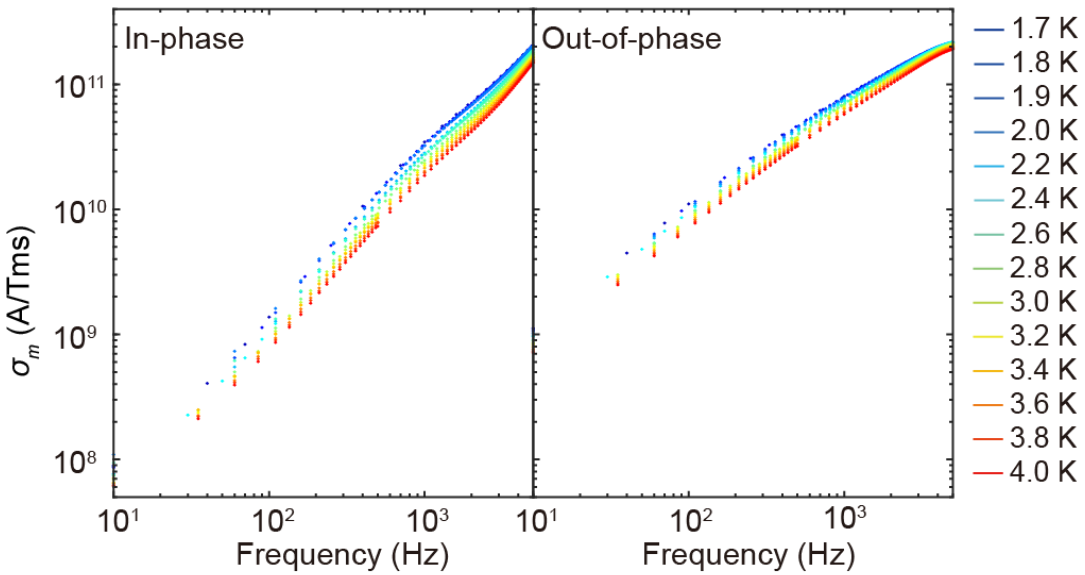

Figure B.2 The log-log plot of measured in-phase and out-of-phase conductivity, Reσ_m and Imσ_m.

f(Hz)	10	60	110	510	1000	1560	2040	3000	4920
$Re\sigma_m$ $(\times 10^{11})$	0.001	0.007	0.02	0.14	0.32	0.53	0.69	1.07	2.01
$Im\sigma_m$ $(\times 10^{11})$	0.01	0.06	0.11	0.45	0.77	1.06	1.28	1.67	2.14

Table B.1 The table of the measured in-phase and out-of-phase conductivity, $Re\sigma_m$ and $Im\sigma_m$ at selective frequencies. The unit for conductivity σ_m is A/Tms.

Appendix C Monopole Density and Transport Dynamics at High Temperatures

To systematically compare the theoretical predictions of bSM with experimental observation, it is important to note that the bSM model was previously primarily considered at temperatures around 1 K where the monopole density is relatively dilute. In this Appendix, I therefore discuss and motivate out use of the bSM model at temperatures up to 4 K.

Firstly, the primary physical argument behind the bSM model, as outlined in ref. (*27*), stems from the fact that the distribution of transverse fields across spins exhibits a bimodal pattern. One subset of spins experiences a transverse field of approximately 0.03 T, while the remaining spins encounter a transverse field of about 0.45 T. Note that these computed transverse fields incorporate contributions from monopoles, in the sense that the magnetic field from a monopole represents the cumulative effect of spins of the tetrahedron hosting the monopole. Significantly, the predominant influence on the transverse field arises from the six nearest-neighbors around each spin, with contributions from spins further away merely serving to broaden the sharp peaks originating from the nearest neighbor contributions.

Secondly, it is important to note that spins not involved in monopole transitions also undergo flipping influenced by the local transverse field. However, for such spin flips the local transverse field is significantly larger than the ~0.03 T experienced by some monopole-hopping spins. This is because the six nearest-neighbour spins almost never

have a vanishing transverse field unless in an exceedingly rare occurrence that a spin sitting between a single monopole and a double monopole of the same sign. Therefore, for bSM simulation, the time iterations not involving monopole hopping are regarded as occurring on the fast time scale (with the only exception just mentioned). It is worth noting that spin configurations that stops the monopole hopping have broader transverse field distribution than the spin configurations which enables the hopping. Thus, the main bSM approximation of only considering two flipping time scales is in fact not exactly precise. This slight difference between the two-timescale approximation and the real hopping time distribution may primarily come into effect at elevated temperatures, where spin flips incurring larger energy costs are more common. Nevertheless, the key consequence of bSM model, namely, the termini which serve as effective blockade due to the minimal transverse field remains accurately addressed.

Similarly, monopole density at higher temperature may affect the current transport. According to the Debye-Hückel theory for spin ice (*47*), the monopole density ρ_0 at equilibrium and at zero field per tetrahedron is given by

$$\rho_0 = \frac{2\exp(-\Delta/T)}{1+2\exp(-\Delta/T)} \tag{C.1}$$

where the gap energy is $\Delta = 4.7$ K. It is computed that approximately 15% of tetrahedra in $Dy_2Ti_2O_7$ host a monopole at $T = 2$ K, whereas the monopole density increases up to 40 % of sites at $T = 4$ K (Figure C.1). This implies that considering monopole transport in the independent monopole and non-interacting limit at 4 K is in fact not precise. However, as discussed above, the implication that bSM relies on the difference of the transverse field in the simulations should not be affected by the high monopole density limit.

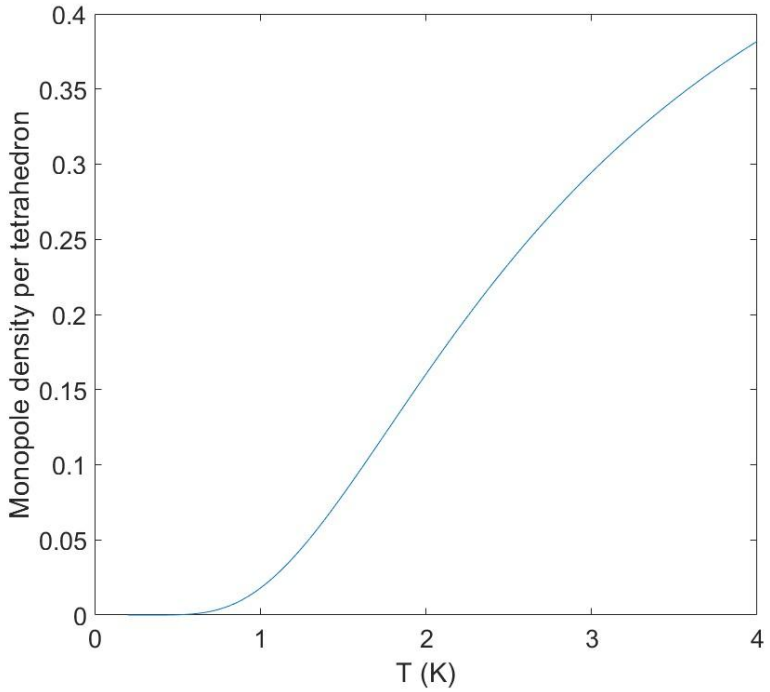

Figure C.1 Monopole densities per tetrahedron as a function of temperature, which is based on the Debye-Hückel theory (*47*).

On the other hand, the phenomenological interpretation of the results is reliant on monopoles as the dominant drivers of magnetic response. In the case of low monopole density, each monopole only needs to hop for an effective fraction of a step to relax the system for weak applied fields. Although the observation of dichotomous transport properties up to 4 K is still surprising, to some extent, since very few steps of hopping are needed, this explains why dichotomous behavior persists to relatively high temperatures. This also indicates that the impact of the transverse field distributions on the response continues to play a key role. Significantly, dichotomous properties are not observed in Monte Carlo bSM simulations at 4 K, suggesting that the simple addition of the second flipping rate may no longer be an accurate description of the system.

Another factor in the high monopole density regime is the field imposed onto a monopole by the neighboring monopole. This effect can be estimated by comparing it with the transverse field generated by the slow/fast spin configuration. The magnetic field B_m of a monopole from the neighboring monopole is given by magnetic Coulomb law as

$$\vec{B}_m = \frac{\mu_0}{4\pi}\frac{m^*}{r^2}\hat{r} \tag{C.2}$$

Assuming that a monopole sits directly next to another monopole in the neighboring tetrahedron it is estimated that this field is around 0.2 T using the lattice distance $r_d = 4.34$ Å, while the transverse field of fast spin-flipping configuration is approximately 0.45 T, and the slow spin-flipping configuration is approximately 0.03 T. This again indicates that the monopole density does not affect the discussion of bSM model since the difference of transverse field at the termini and at the fast hopping rate is larger than the field which a neighboring monopole can generate.

Appendix D Sample Demagnetization factor

Experimentally, the sample geometry and its demagnetization field can affect the magnetization measurement to some extent. For example, the claim of measuring monopole charge with Wein affect (*33*) could actually be owing to the demagnetization field of the sheet-shaped sample (*35*), which leads to some controversies. In this appendix, I briefly discuss the demagnetization factor for the DTO sample we performed for the measurements. The demagnetization factor for a sample in rod geometry with the field aligned along the rod approaches zero in the limit of infinite length. However, in practice, a finite size rod-shaped sample has a demagnetization field B_d of

$$\vec{B}_d = -N(\vec{r})\mu_0\vec{M} \tag{D.1}$$

where demagnetization factor is $N(\vec{r})$ and is position dependent. $N(\vec{r})$ for a cuboid with a dimension of 2a × 2b × 2c can be expressed as (*100*)

$$N_{ii}(\vec{r}) = \frac{1}{4\pi}\sum_{\alpha=\pm1}\sum_{\beta=\pm1}\sum_{\gamma=\pm1}\tan^{-1}(f_i(\alpha x, \beta y, \gamma z)) \tag{D.2}$$

with $i = x, y, z$. Also,

$$f_x(x,y,z) = \frac{(b-y)((c-z)}{(a-x)\sqrt{[(a-x)^2+(b-y)^2+(c-z)^2]}} \tag{D.3}$$

$$f_y(x,y,z) = \frac{(a-x)((c-z)}{(b-y)\sqrt{[(a-x)^2+(b-y)^2+(c-z)^2]}} \tag{D.4}$$

$$f_z(x,y,z) = \frac{(b-y)((a-x)}{(c-z)\sqrt{[(a-x)^2+(b-y)^2+(c-z)^2]}} \tag{D.5}$$

We argue that for the flux threading the superconducting coil which winds at the center of the DTO sample, $N_{zz}(0,0,0)$ contributes to the measurement the most. By using the dimension of 2a = 1.3 mm, 2b = 1.3 mm, 2c = 6.5 mm, this yields an effective demagnetization factor of

$$N_{zz}(0,0,0) \sim 0.0113 \tag{D.6}$$

Therefore, the estimated demagnetization factor is roughly 1%. The observations of two timescale monopole transport and the derived relaxation time are not affected by the demagnetization field. Quantitatively, a small fraction of 1% of the measured flux could be accounted for the demagnetization factor.

Appendix E Magnetic Susceptibility and Ergodicity Measurements of $Dy_2Ti_2O_7$

This Appendix serves as a supplementary to Chapter 5, where I provide the complete set of magnetic susceptibility measurement and the description of the fitting to the Havriliak-Negami (HN) equation. Furthermore, the correspondence of the full magnetic susceptibility data set to the FDT relation is presented in this appendix.

Supplementary Magnetic Susceptibility Measurement Data

To measure temperature dependence susceptibility, a lock-in technique is implemented with varying temperatures. The circuit diagram is described in the frequency domain measurement in Chapter 2. By collecting the SQUID voltage output under a sinusoidal magnetic field modulation B_{mod}, the real and the imaginary part of magnetic susceptibility can be derived from

$$\chi'(\omega,T) = \frac{V_x(\omega,T)}{B_{mod}}\left(\frac{1}{\alpha\gamma NFA_P}\right) \quad \text{(E.1)}$$

$$\chi''(\omega,T) = \frac{-V_y(\omega,T)}{B_{mod}}\left(\frac{1}{\alpha\gamma NFA_P}\right) \quad \text{(E.2)}$$

where $\alpha, \gamma, N, F, A_P$ are experimental parameters that are described in detail in Appendix A. The full set of magnetic susceptibility result for DTO at T = 20 mK to 2500 mK is shown in Figure E.1. Consistent with previous reports (*21, 22, 24, 25*), the magnetic susceptibility evolves towards longer relaxation time by lowering temperatures. It is known that DTO enters supercooled state below 1 K (*21*) and the magnetic susceptibility follows the HN equation. As indicated by Eqn. 5.2, the real and imaginary part of

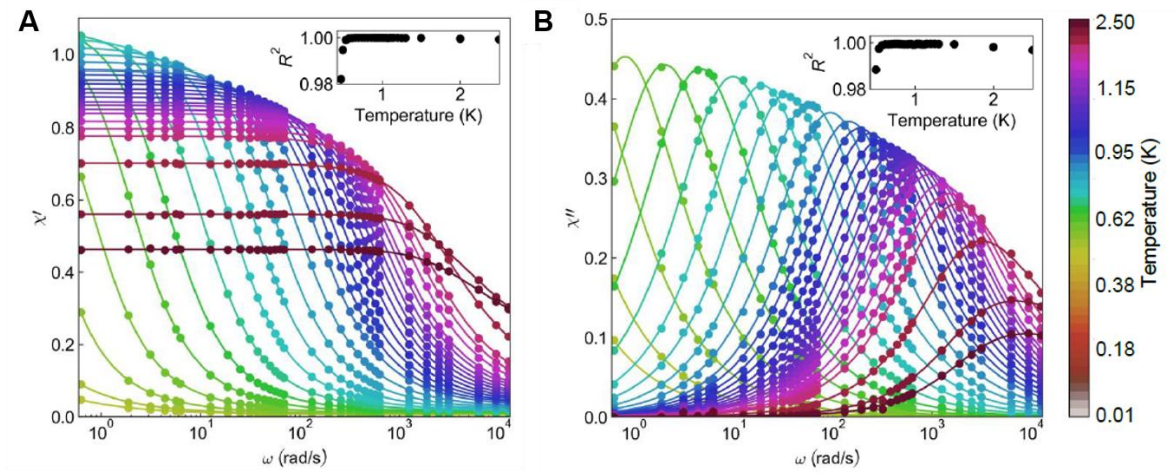

Figure E.1 (A) and (B) Real and imaginary part of AC susceptibility with frequency and temperature dependence.

magnetic susceptibility can be expressed by

$$\chi' = \chi_\infty + \chi_0 \frac{\cos(\gamma_{HN}\phi)}{\left(1+2(\omega\tau)^{\alpha_{HN}}\cos\left(\frac{\pi\alpha_{HN}}{2}\right)+(\omega\tau)^{2\alpha_{HN}}\right)^{\gamma_{HN}/2}} \tag{E.3}$$

$$\chi'' = \chi_0 \frac{\sin(\gamma_{HN}\phi)}{\left(1+2(\omega\tau)^{\alpha_{HN}}\cos\left(\frac{\pi\alpha_{HN}}{2}\right)+(\omega\tau)^{2\alpha_{HN}}\right)^{\gamma_{HN}/2}} \tag{E.4}$$

where ϕ is defined as

$$\phi = \arctan\left((\omega\tau)^{\alpha_{HN}}\sin\left(\frac{\pi\alpha_{HN}}{2}\right)/1+(\omega\tau)^{\alpha_{HN}}\cos\left(\frac{\pi\alpha_{HN}}{2}\right)\right) \tag{E.5}$$

Thus, the magnetic susceptibility data presented in Figure E.1 is fitted with Eqn. E.3 and E.4, which shows excellent agreement.

Supplementary Magnetization Noise Data and Ergodicity Analysis

Similarly, as mentioned in Chapter 5, by comparing the magnetic susceptibility and the simultaneously measured magnetization noise, the fluctuation-dissipation relation can be examined. In Chapter 5, the magnetization noise for the full measured temperature has been presented. The noise data has been fitted with Eqn. 1.15 and the noise exponent

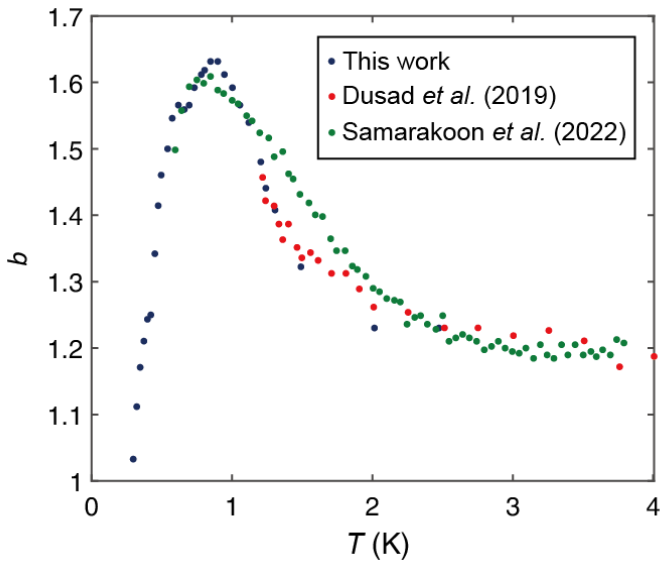

Figure E.2 Comparison of the noise exponent b with previous literatures (*39, 46*).

has been shown in Figure 5.11. Here I present the comparison of the extracted noise exponent with previous literatures in Figure E.2. Additionally, the magnetization noise of DTO from 100 mK to 620 mK is presented in Figure E.3A. To compare the consistency of FDT relation, the data points are marked with a cross for the guidance, corresponding to the cross in the magnetic susceptibility in Figure E.3B. Clearly, by plotting the measured magnetization noise against the calculated noise from susceptibility, the violation of FDT relation is observed below 300 mK (Figure E.3C). In addition, to examine the FDT relation, an ergodicity function $X(\omega, T)$ is defined in Eqn. 5.3. The result of average of ergodicity function $\overline{X}(T)$ over the measured frequencies is already shown in Figure 5.11. Here I present an additional example of frequency dependence $X(\omega)$ at 700 mK in Figure E.4. The overall function lies around 1 but with slight shift at low and high frequencies. These are perhaps due to the low frequency electronic noise and the high frequency SQUID bandwidth suppression. The averaging over the measured frequency should suppress the systematic error.

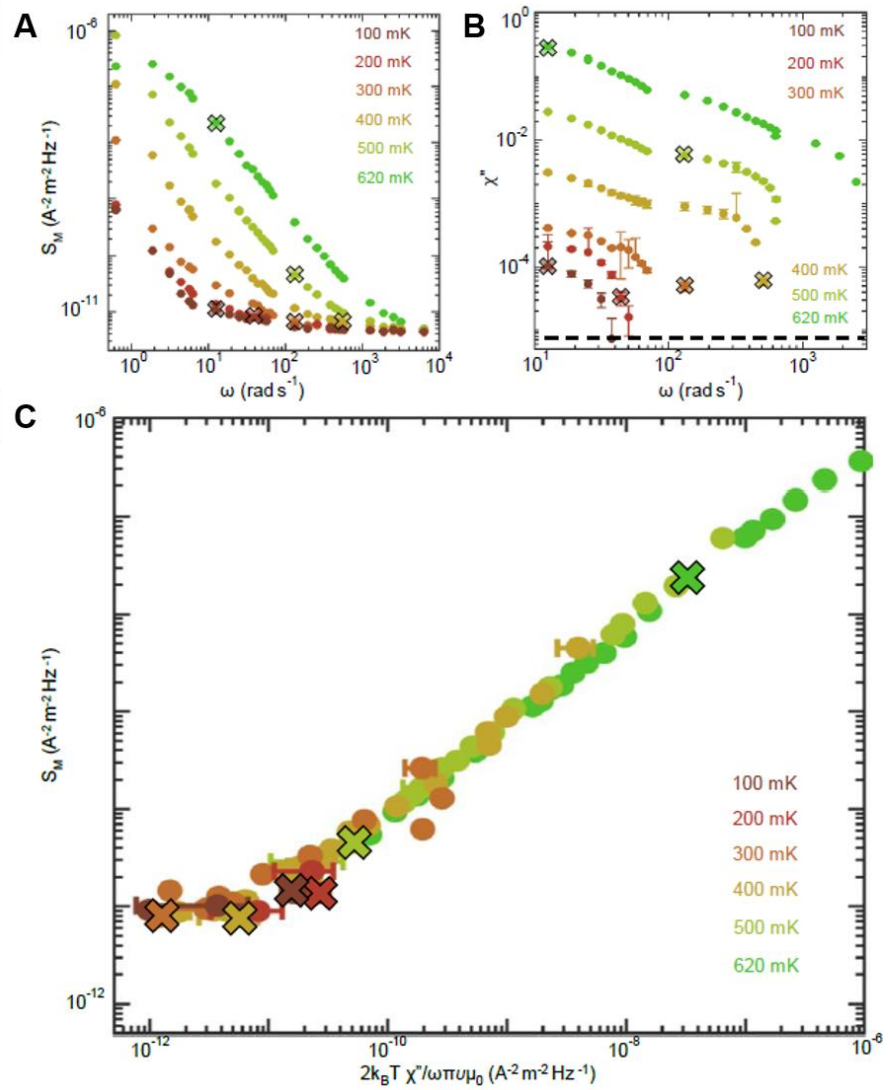

Figure E.3 (A) Magnetization noise S_M at 100 mK to 620 mK. Each curve corresponds to the magnetization noise data at frequencies matching those of the susceptibility measurements in (B). (B) Imaginary susceptibility χ'' at the same temperatures as in (a). (C) The measured magnetization noise S_M versus the noise derived from panel (B), with the same points highlighted in (A) and (B).

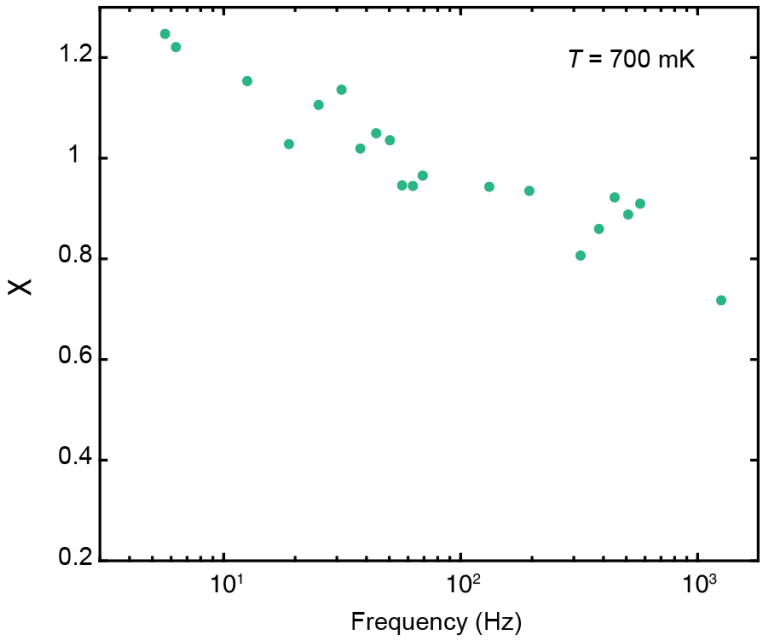

Figure E.4 An example of frequency dependence ergodicity function $X(\omega)$ at 700 mK. The slight deviation at low frequency could be affected from the $1/f$ noise of the electronics, while the high frequency part could be affected by the overall SQUID bandwidth.

Appendix F Estimation of Magnetic Charge in Spin Ice

In Chapter 6, by collecting the flux at equilibrium under the application of step-wise magnetic with varying field strength and temperatures, the quantitative value of magnetic charge is measured precisely. To compare with theory, I would like to discuss the careful estimation of theoretical value for magnetic charge in this Appendix.

Theoretical Estimation

Based on the original Hamiltonian in Ref (*14, 47*), the magnetic charge is predicted to be $m = 2\mu/a_d$. Thus, the theoretical expectation of magnetic charge can be estimated from accurate measurement of the magnetic moment of Dy^{3+} ion for DTO and from the lattice constant. Notably, the magnetic moment in terms of Bohr magneton is

$$\mu = g_J \sqrt{J(J+1)}\mu_B \tag{F.1}$$

where the g factor is expressed by

$$g_J = \frac{3}{2} + \frac{S(S+1)-L(L+1)}{2J(J+1)} \tag{F.2}$$

By plugging in the parameters for Dy^{3+} that L =5, S = 5/2, J = 15/2, Eqn. F.2 leads to $\mu = 10.64\mu_B$ from Hund's rule, while the fitting from the DC magnetic susceptibility measurement (*7*) yields a magnetic moment of 10.0(1) μ_B. On the other hand, the distance between two tetrahedron can be calculated from the lattice constant measured by the X-ray diffraction. According to Ref. (*101*), the lattice constant is measured to be a = 10.09 Å. The distance of two Dy^{3+} ion is therefore 3.568 Å, and the $a_d = \sqrt{3/2} \times 3.568$ = 4.37(2) Å. In combination, the magnetic charge in DTO is estimated to be

$$m = 2\mu/a_d = 4.57\mu_B\text{Å}^{-1} \tag{F.3}$$

Interestingly, for HTO with Ho^{3+} ions forming a pyrochlore lattice, Ho^{3+} has a magnetic moment of $\mu = 10.61\mu_B$ and a similar lattice constant of 10.07 Å. This leads to an almost exactly identical value of magnetic charge.

Additional Experimental Measurements

The detailed experimental estimation has been discussed in Chapter 6.5. The monopole charge is measured to be $m = 4.36 \times 10^{-13}$ [Am] with high precision. However, it is found out that at low temperatures, the measured monopole charge deviates from the theoretical expectation $m = 4.24 \times 10^{-13}$[Am]. Here I provide additional experimental data below 1.4 K. Figure F.1 shows the simultaneous plot of all of measured $\Phi_S(\infty, T, H)$ versus $\frac{\sqrt{3}}{16}\frac{A_S{\mu_0}^2}{a_d k_B}\frac{H}{T}$ from 0.6 K to 6 K. Since the black line marks the slope for the theoretical value, it is clear that the measured slope (charge) decreases by lowering the temperature.

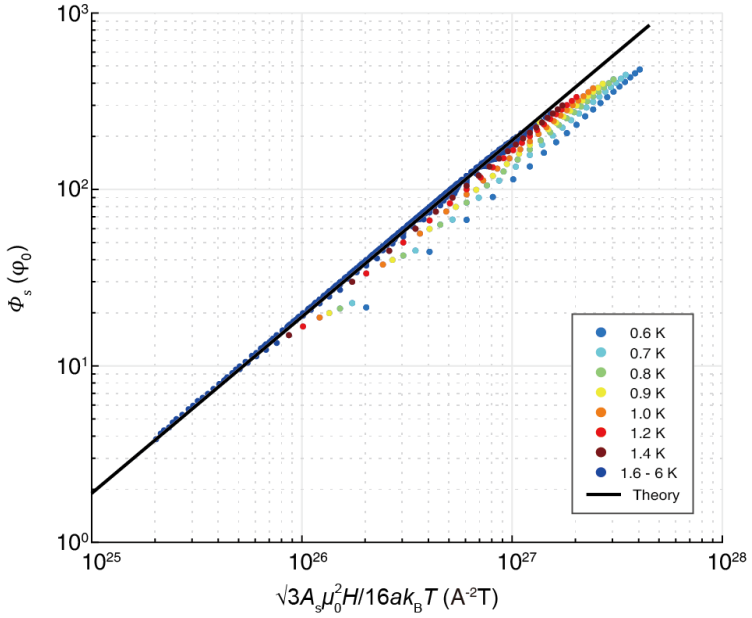

Figure F.1 Simultaneous plot of all of measured $\Phi_S(\infty, T, H)$, versus $\frac{\sqrt{3}}{16}\frac{A_S{\mu_0}^2}{a_d k_B}\frac{H}{T}$. The fitted line is plotted in black with a slope of m^2 for T = 0.6 K – 6 K.

Reference

1. C. Castelnovo, R. Moessner, S. L. Sondhi, Spin Ice, Fractionalization, and Topological Order. *Annu. Rev. Condens. Matter Phys.* **3**, 35-55 (2012).
2. S. T. Bramwell, M. J. Harris, The history of spin ice. *J. Phys. Condens. Matter* **32**, 374010 (2020).
3. S. T. Bramwell, M. J. P. Gingras, Spin Ice State in Frustrated Magnetic Pyrochlore Materials. *Science* **294**, 1495-1501 (2001).
4. M. Udagawa, L. Jaubert, in *Spin Ice*. (Springer, 2021).
5. R. Moessner, J. T. Chalker, Properties of a Classical Spin Liquid: The Heisenberg Pyrochlore Antiferromagnet. *Phys. Rev. Lett.* **80**, 2929-2932 (1998).
6. M. J. Harris, S. T. Bramwell, D. F. McMorrow, T. Zeiske, K. W. Godfrey, Geometrical Frustration in the Ferromagnetic Pyrochlore Ho2Ti2O7. *Phys. Rev. Lett.* **79**, 2554-2557 (1997).
7. H. Fukazawa, R. G. Melko, R. Higashinaka, Y. Maeno, M. J. P. Gingras, Magnetic anisotropy of the spin-ice compound $Dy_2Ti_2O_7$. *Phys. Rev. B* **65**, 054410 (2002).
8. T. Fennell *et al.*, Neutron scattering investigation of the spin ice state in $Dy_2Ti_2O_7$. *Phys. Rev. B* **70**, 134408 (2004).
9. A. P. Ramirez, A. Hayashi, R. J. Cava, R. Siddharthan, B. S. Shastry, Zero-point entropy in 'spin ice'. *Nature* **399**, 333-335 (1999).
10. R. Siddharthan *et al.*, Ising Pyrochlore Magnets: Low-Temperature Properties, ``Ice Rules," and Beyond. *Phys. Rev. Lett.* **83**, 1854-1857 (1999).
11. B. C. den Hertog, M. J. P. Gingras, Dipolar Interactions and Origin of Spin Ice in Ising Pyrochlore Magnets. *Phys. Rev. Lett.* **84**, 3430-3433 (2000).
12. T. Sakakibara, T. Tayama, Z. Hiroi, K. Matsuhira, S. Takagi, Observation of a Liquid-Gas-Type Transition in the Pyrochlore Spin Ice Compound $Dy_2Ti_2O_7$ in a Magnetic Field. *Phys. Rev. Lett.* **90**, 207205 (2003).
13. K. Matsuhira, Z. Hiroi, T. Tayama, S. Takagi, T. Sakakibara, A new macroscopically degenerate ground state in the spin ice compound $Dy_2Ti_2O_7$ under a magnetic field. *J. Phys. Condens. Matter* **14**, L559 (2002).
14. C. Castelnovo, R. Moessner, S. L. Sondhi, Magnetic monopoles in spin ice. *Nature* **451**, 42-45 (2008).

15. I. A. Ryzhkin, Magnetic relaxation in rare-earth oxide pyrochlores. *J. Exp. Theor. Phys.* **101**, 481-486 (2005).
16. S. V. Isakov, R. Moessner, S. L. Sondhi, Why Spin Ice Obeys the Ice Rules. *Phys. Rev. Lett.* **95**, 217201 (2005).
17. P. A. M. Dirac, Quantised singularities in the electromagnetic field. *Proc. R. Soc. Lond. A* **133**, 60-72 (1931).
18. L. D. C. Jaubert, P. C. W. Holdsworth, Signature of magnetic monopole and Dirac string dynamics in spin ice. *Nat. Phys.* **5**, 258-261 (2009).
19. L. D. C. Jaubert, P. C. W. Holdsworth, Magnetic monopole dynamics in spin ice. *J. Phys. Condens. Matter* **23**, 164222 (2011).
20. J. Snyder *et al.*, Low-temperature spin freezing in the $Dy_2Ti_2O_7$ spin ice. *Phys. Rev. B* **69**, 064414 (2004).
21. E. R. Kassner *et al.*, Supercooled spin liquid state in the frustrated pyrochlore $Dy_2Ti_2O_7$. *Proc. Natl. Acad. Sci. U.S.A.* **112**, 8549-8554 (2015).
22. L. R. Yaraskavitch *et al.*, Spin dynamics in the frozen state of the dipolar spin ice material $Dy_2Ti_2O_7$. *Phys. Rev. B* **85**, 020410 (2012).
23. L. Bovo, J. A. Bloxsom, D. Prabhakaran, G. Aeppli, S. T. Bramwell, Brownian motion and quantum dynamics of magnetic monopoles in spin ice. *Nat. Commun.* **4**, 1535 (2013).
24. K. Matsuhira *et al.*, Spin Dynamics at Very Low Temperature in Spin Ice $Dy_2Ti_2O_7$. *J. Phys. Soc. Jpn.* **80**, 123711 (2011).
25. K. Matsuhira, Y. Hinatsu, T. Sakakibara, Novel dynamical magnetic properties in the spin ice compound $Dy_2Ti_2O_7$. *J. Phys. Condens. Matter* **13**, L737 (2001).
26. J. Snyder *et al.*, Quantum-Classical Reentrant Relaxation Crossover in $Dy_2Ti_2O_7$ Spin Ice. *Phys. Rev. Lett.* **91**, 107201 (2003).
27. J. N. Hallén, S. A. Grigera, D. A. Tennant, C. Castelnovo, R. Moessner, Dynamical fractal and anomalous noise in a clean magnetic crystal. *Science* **378**, 1218-1221 (2022).
28. D. J. P. Morris *et al.*, Dirac Strings and Magnetic Monopoles in the Spin Ice $Dy_2Ti_2O_7$. *Science* **326**, 411-414 (2009).

29. T. Yavors'kii, T. Fennell, M. J. P. Gingras, S. T. Bramwell, $Dy_2Ti_2O_7$ Spin Ice: A Test Case for Emergent Clusters in a Frustrated Magnet. *Phys. Rev. Lett.* **101**, 037204 (2008).
30. L. D. C. Jaubert, J. T. Chalker, P. C. W. Holdsworth, R. Moessner, The Kasteleyn transition in three dimensions: Spin ice in a [100] field. *J. Phys. Conf. Ser.* **145**, 012024 (2009).
31. L. D. C. Jaubert, J. T. Chalker, P. C. W. Holdsworth, R. Moessner, Three-Dimensional Kasteleyn Transition: Spin Ice in a [100] Field. *Phys. Rev. Lett.* **100**, 067207 (2008).
32. C. L. Henley, The "Coulomb Phase" in Frustrated Systems. *Annu. Rev. Condens. Matter Phys.* **1**, 179-210 (2010).
33. S. T. Bramwell *et al.*, Measurement of the charge and current of magnetic monopoles in spin ice. *Nature* **461**, 956-959 (2009).
34. S. R. Dunsiger *et al.*, Spin Ice: Magnetic Excitations without Monopole Signatures Using Muon Spin Rotation. *Phys. Rev. Lett.* **107**, 207207 (2011).
35. S. J. Blundell, Monopoles, Magnetricity, and the Stray Field from Spin Ice. *Phys. Rev. Lett.* **108**, 147601 (2012).
36. G. Sala *et al.*, Magnetic Coulomb Fields of Monopoles in Spin Ice and Their Signatures in the Internal Field Distribution. *Phys. Rev. Lett.* **108**, 217203 (2012).
37. J. Lago, S. J. Blundell, C. Baines, μSR investigation of spin dynamics in the spin-ice material Dy2Ti2O7. *J. Phys. Condens. Matter* **19**, 326210 (2007).
38. F. K. K. Kirschner, F. Flicker, A. Yacoby, N. Y. Yao, S. J. Blundell, Proposal for the detection of magnetic monopoles in spin ice via nanoscale magnetometry. *Phys. Rev. B* **97**, 140402 (2018).
39. R. Dusad *et al.*, Magnetic monopole noise. *Nature* **571**, 234-239 (2019).
40. F. Bonani, G. Ghione, Generation–recombination noise modelling in semiconductor devices through population or approximate equivalent current density fluctuations. *Solid-State Electronics* **43**, 285-295 (1999).
41. K. S. Champlin, Generation-recombination noise in semiconductors—The equivalent circuit approach. *IRE Transactions on Electron Devices* **7**, 29-38 (1960).

42. R. Müller, in *Noise in Physical Systems,* D. Wolf, Ed. (Springer Berlin Heidelberg, Berlin, Heidelberg, 1978), pp. 13-25.
43. A. V. Klyuev, M. I. Ryzhkin, A. V. Yakimov, Statistics of Fluctuations of Magnetic Monopole Concentration in Spin Ice. *Fluct. Noise Lett.* **16**, 1750035 (2017).
44. A. B. Eyvazov *et al.*, Common glass-forming spin-liquid state in the pyrochlore magnets $Dy_2Ti_2O_7$ and $Ho_2Ti_2O_7$. *Phys. Rev. B* **98**, 214430 (2018).
45. D. Pomaranski *et al.*, Absence of Pauling's residual entropy in thermally equilibrated $Dy_2Ti_2O_7$. *Nat. Phys.* **9**, 353-356 (2013).
46. A. M. Samarakoon *et al.*, Anomalous magnetic noise in an imperfectly flat landscape in the topological magnet $Dy_2Ti_2O_7$. *Proc. Natl. Acad. Sci. U.S.A.* **119**, e2117453119 (2022).
47. C. Castelnovo, R. Moessner, S. L. Sondhi, Debye-H\"uckel theory for spin ice at low temperature. *Phys. Rev. B* **84**, 144435 (2011).
48. L. Onsager, Deviations from Ohm's Law in Weak Electrolytes. *J. Chem. Phys* **2**, 599-615 (2004).
49. B. Tomasello, C. Castelnovo, R. Moessner, J. Quintanilla, Correlated Quantum Tunneling of Monopoles in Spin Ice. *Phys. Rev. Lett.* **123**, 067204 (2019).
50. I. A. Ryzhkin, M. I. Ryzhkin, Screening of the magnetic field by magnetic monopoles in spin ice. *JETP Lett.* **93**, 384-387 (2011).
51. M. I. Ryzhkin, I. A. Ryzhkin, S. T. Bramwell, Dynamic susceptibility and dynamic correlations in spin ice. *Europhys. Lett.* **104**, 37005 (2013).
52. I. A. Ryzhkin, R. W. Whitworth, The configurational entropy in the Jaccard theory of the electrical properties of ice. *J. Phys. Condens. Matter* **9**, 395 (1997).
53. A. M. Samarakoon *et al.*, Machine-learning-assisted insight into spin ice Dy2Ti2O7. *Nat. Commun.* **11**, 892 (2020).
54. A. V. Klyuev, M. I. Ryzhkin, A. V. Yakimov, B. Spagnolo, Memory effect and generation-recombination noise of magnetic monopoles in spin ice. *J. Stat. Mech.* **2019**, 094005 (2019).
55. C. Nisoli, The color of magnetic monopole noise. *Europhys. Lett.* **135**, 57002 (2021).
56. C.-C. Hsu *et al.*, Dichotomous dynamics of magnetic monopole fluids. *Proc. Natl. Acad. Sci. U.S.A.* **121**, e2320384121 (2024).

57. J. B. Johnson, Thermal Agitation of Electricity in Conductors. *Phys. Rev.* **32**, 97-109 (1928).

58. H. Nyquist, Thermal Agitation of Electric Charge in Conductors. *Phys. Rev.* **32**, 110-113 (1928).

59. R. Kubo, The fluctuation-dissipation theorem. *Rep. Prog. Phys.* **29**, 255-284 (1966).

60. W. Reim, R. H. Koch, A. P. Malozemoff, M. B. Ketchen, H. Maletta, Magnetic Equilibrium Noise in Spin-Glasses: $Eu_{0.4}Sr_{0.6}S$. *Phys. Rev. Lett.* **57**, 905-908 (1986).

61. S. Vitale, A. Cavalleri, M. Cerdonio, A. Maraner, G. A. Prodi, Thermal equilibrium noise with $1/f$ spectrum in a ferromagnetic alloy: Anomalous temperature dependence. *J. Appl. Phys.* **76**, 6332-6334 (1994).

62. V. Raban, L. Berthier, P. C. W. Holdsworth, Violation of the fluctuation-dissipation theorem and effective temperatures in spin ice. *Phys. Rev. B* **105**, 134431 (2022).

63. K. Agarwal, E. Demler, I. Martin, $1/f^{\alpha}$ noise and generalized diffusion in random Heisenberg spin systems. *Phys. Rev. B* **92**, 184203 (2015).

64. J. Y. Khoo, F. Pientka, P. A. Lee, I. S. Villadiego, Probing the quantum noise of the spinon Fermi surface with NV centers. *Phys. Rev. B* **106**, 115108 (2022).

65. E. B. Aleksandrov, V. S. Zapasskii, Spin Noise Spectroscopy. *J. Phys. Conf. Ser* **324**, 012002 (2011).

66. N. A. Sinitsyn, Y. V. Pershin, The theory of spin noise spectroscopy: a review. *Rep. Prog. Phys.* **79**, 106501 (2016).

67. R. C. Jaklevic, J. Lambe, A. H. Silver, J. E. Mercereau, Quantum Interference Effects in Josephson Tunneling. *Phys. Rev. Lett.* **12**, 159-160 (1964).

68. D. Drung, M. Mück, in *The SQUID Handbook*. (2004), pp. 127-170.

69. T. Sleator, E. L. Hahn, C. Hilbert, J. Clarke, Nuclear-spin noise. *Phys. Rev. Lett.* **55**, 1742-1745 (1985).

70. J. Magnusson, P. Nordblad, P. Svedlindh, Flux noise in $Bi_2Sr_2CaCu_2O8$ displaying the paramagnetic Meissner effect: Evidence of spontaneous magnetic moments. *Phys. Rev. B* **57**, 10929-10935 (1998).

71. P. Svedlindh *et al.*, Equilibrium magnetic fluctuations of a short-range Ising spin glass. *Phys. Rev. B* **40**, 7162-7166 (1989).
72. M. B. Weissman, What is a spin glass? A glimpse via mesoscopic noise. *Rev. Mod. Phys.* **65**, 829-839 (1993).
73. P. K. Yadav, R. Upadhyay, R. Kumar, P. Nukala, C. Upadhyay, Emergence of field-induced memory effect in spin ices. *J. Phys. Condens. Matter* **35**, 495601 (2023).
74. V. G. Artemov, A unified mechanism for ice and water electrical conductivity from direct current to terahertz. *Phys. Chem. Chem. Phys.* **21**, 8067-8072 (2019).
75. H. M. Revell *et al.*, Evidence of impurity and boundary effects on magnetic monopole dynamics in spin ice. *Nat. Phys.* **9**, 34-37 (2013).
76. C. Paulsen *et al.*, Experimental signature of the attractive Coulomb force between positive and negative magnetic monopoles in spin ice. *Nat. Phys.* **12**, 661-666 (2016).
77. M. J. Jackson *et al.*, Dynamic behavior of magnetic avalanches in the spin-ice compound $Dy_2Ti_2O_7$. *Phys. Rev. B* **90**, 064427 (2014).
78. J. Dasini, Discovery of Dynamical Heterogeneity in a Supercooled Magnetic Monopole Fluid. arXiv:2408.00460 (2024).
79. L. Berthier, G. Biroli, Theoretical perspective on the glass transition and amorphous materials. *Rev. Mod. Phys.* **83**, 587-645 (2011).
80. J.-P. Bouchaud, G. Biroli, On the Adam-Gibbs-Kirkpatrick-Thirumalai-Wolynes scenario for the viscosity increase in glasses. *J. Chem. Phys* **121**, 7347-7354 (2004).
81. D. Chandler, J. P. Garrahan, Dynamics on the Way to Forming Glass: Bubbles in Space-Time. *Annu. Rev. Phys. Chem.* **61**, 191-217 (2010).
82. A. Lemaître, Structural Relaxation is a Scale-Free Process. *Phys. Rev. Lett.* **113**, 245702 (2014).
83. G. Tarjus, S. A. Kivelson, Z. Nussinov, P. Viot, The frustration-based approach of supercooled liquids and the glass transition: a review and critical assessment. *J. Phys. Condens. Matter* **17**, R1143 (2005).
84. H. Tanaka, T. Kawasaki, H. Shintani, K. Watanabe, Critical-like behaviour of glass-forming liquids. *Nat. Mater.* **9**, 324-331 (2010).

85. L. Berthier, Dynamic Heterogeneity in Amorphous Materials. *Physics* **4**, 42 (2011).

86. M. D. Ediger, Spatially Heterogeneous Dynamics in Supercooled Liquids. *Annu. Rev. Phys. Chem.* **51**, 99-128 (2000).

87. M. M. Hurley, P. Harrowell, Non-Gaussian behavior and the dynamical complexity of particle motion in a dense two-dimensional liquid. *J. Chem. Phys* **105**, 10521-10526 (1996).

88. A. M. Samarakoon *et al.*, Structural magnetic glassiness in the spin ice $Dy_2Ti_2O_7$. *Phys. Rev. Res.* **4**, 033159 (2022).

89. J. G. Rau, M. J. P. Gingras, Spin slush in an extended spin ice model. *Nat. Commun.* **7**, 12234 (2016).

90. T. S. Grigera, N. E. Israeloff, Observation of Fluctuation-Dissipation-Theorem Violations in a Structural Glass. *Phys. Rev. Lett.* **83**, 5038-5041 (1999).

91. H. Oukris, N. E. Israeloff, Nanoscale non-equilibrium dynamics and the fluctuation–dissipation relation in an ageing polymer glass. *Nat. Phys.* **6**, 135-138 (2010).

92. J. Snyder, J. S. Slusky, R. J. Cava, P. Schiffer, How 'spin ice' freezes. *Nature* **413**, 48-51 (2001).

93. A. Sen, R. Moessner, Topological Spin Glass in Diluted Spin Ice. *Phys. Rev. Lett.* **114**, 247207 (2015).

94. R. de-Picciotto *et al.*, Direct observation of a fractional charge. *Nature* **389**, 162-164 (1997).

95. S. T. Bramwell, Dimensional analysis, spin freezing and magnetization in spin ice. *J. Phys. Condens. Matter* **23**, 112201 (2011).

96. L. D. C. Jaubert *et al.*, Topological-Sector Fluctuations and Curie-Law Crossover in Spin Ice. *Phys. Rev. X* **3**, 011014 (2013).

97. L. Bovo *et al.*, Restoration of the third law in spin ice thin films. *Nat. Commun.* **5**, 3439 (2014).

98. R. Cantor, D. Koelle, in *The SQUID Handbook*. (2004), pp. 171-217.

99. C. P. Foley, M. N. Keene, H. J. M. ter Brake, J. Vrba, in *The SQUID Handbook*. (2004), pp. 251-355.

100. A. Smith *et al.*, The demagnetizing field of a nonuniform rectangular prism. *J. Appl. Phys.* **107**, 103910 (2010).
101. J. M. Farmer *et al.*, Structural and crystal chemical properties of rare-earth titanate pyrochlores. *J. Alloys Compd.* **605**, 63-70 (2014).